NUMERICAL STUDY OF HEAT TRANSFER AND FLUID FLOW CHARACTERISTICS IN MICROCHANNEL HEAT SINK

K. NARREIN A/L KRISHNASAMY

FACULTY OF ENGINEERING
UNIVERSITY OF MALAYA
KUALA LUMPUR

2016

NUMERICAL STUDY OF HEAT TRANSFER AND FLUID FLOW CHARACTERISTICS IN MICROCHANNEL HEAT SINK

K. NARREIN A/L KRISHNASAMY

THESIS SUBMITTED IN FULFILMENT OF THE REQUIREMENTS FOR THE DEGREE OF DOCTOR OF PHILOSOPHY

DEPARTMENT OF MECHANICAL ENGINEERING
FACULTY OF ENGINEERING
UNIVERSITY OF MALAYA
KUALA LUMPUR

2016

ABSTRACT

Numerical investigation is performed to study the heat transfer and fluid flow characteristics in a Microchannel Heat Sink (MCHS) with the combination of various active and passive enhancement methods. Convective heat transfer analyses are performed on the MCHS and the governing equations are solved using the finite volume method. The performances of the MCHS are tested by varying the geometrical parameters, magnitude of external forces, boundary conditions, flow type and different fluids.

For the study on effects of geometry, the thermal field results show that Helical MCHS (HMCHS) can contribute to better heat transfer enhancement as compared to a straight microchannel of similar length and hydraulic diameter due to the presence of secondary flow. Geometrical parameters such as helix radius, pitch and channel aspect ratio have significant effect on the performance of the MCHS due to the variation in flow characteristics. It is also noted that the modified two-phase mixture model method produce more accurate results as compared to single phase nanofluid model, hence, this new model can be used in future research for better results. In addition, pulsating inlet flow condition is able to increase the convective heat transfer substantially with marginal reduction in pressure drop compared to steady condition. Pronounced enhancement in Nusselt number is also achieved in the HMCHS with porous medium compared to the non-porous straight and helical microchannel.

The study on the effects of external forces showed that presence of magnetic field lead to thermal enhancement with additional pressure drop. The external force prevents the flow from reaching a fully develop state, hence the larger fluid velocity at the bottom wall result in better convective heat transfer.

ABSTRAK

Siasatan berangka dilakukan untuk mengkaji pemindahan haba dan ciri-ciri aliran bendalir dalam Pembenam Haba Saluran Mikro (PHSM) dengan kombinasi pelbagai kaedah peningkatan prestasi aktif dan pasif. Analisis pemindahan haba perolakan dilakukan ke atas PHSM dengan menyelesaikan pelbagai persamaan. Prestasi PHSM diuji dengan mengubah geometri, magnitud daya luar, jenis aliran dan sebagainya.

Untuk kajian pada kesan geometri, keputusan menunjukkan bahawa PHSM heliks (PHSMH) boleh menyumbang kepada peningkatan pemindahan haba berbanding dengan PHSM biasa yang mempunyai diameter hidraulik yang sama disebabkan kehadiran aliran sekunder. Parameter geometri seperti jejari heliks, jarak antata pusingan heliks dan nisbah aspek saluran mempunyai kesan yang besar ke atas prestasi PHSM disebabkan oleh perubahan dalam ciri-ciri aliran. Juga diperhatikan bahawa model campuran dua fasa yang diubahsuai menghasilkan keputusan yang lebih tepat berbanding model satu fasa bagi kes aliran cecair nano dalam PHSM. Oleh yang demikian, model baru ini boleh digunakan dalam usaha penyelidikan masa depan untuk keputusan yang lebih baik. Selain itu, ia juga diperhatikan bahawa keadaan aliran masuk sinusoidal dapat meningkatkan pemindahan haba perolakan dengan ketara dan juga mengurangkan magnitud penurunun tekanan berbanding keadaan stabil. Peningkatan ketara dalam kadar pemindahan haba dicapai dalam PHSM dengan medium berliang berbanding PHSM biasa tanpa medium berliang.

Kajian tentang kesan daya luar menunjukkan bahawa kehadiran daya magnet menjurus kepada peningkatan kadar pemindahan haba dan diiringi dengan penurunun tekanan yang lebih. Daya luaran menghalang aliran dari mencapai perkembangan yang sepenuhnya, oleh itu perbezaan suhu yang lebih besar antara dinding bahagian bawah dan cecair menjurus kepada kadar pemindahan haba yang lebih baik.

ACKNOWLEDGEMENTS

The author expresses his sincere appreciation to all who contributed to the success of this research. Special thanks to the research supervisor Dr. S. Sivasankaran, Institute of Mathematical Sciences University Malaya who had offered great assistance throughout this project. Without his knowledge and assistance this study would not have been successful.

Finally, sincere gratitude and acknowledgement is dedicated towards the contribution of author's parents, wife and friends who had been helpful and supportive throughout this research.

TABLE OF CONTENTS

LIST OF FIGURES

LIST OF TABLES

LIST OF SYMBOLS AND ABBREVIATIONS

B_o	Magnetic field strength
C_p	Heat Capacity, (J/kg. k)
D	Channel depth, (m)
D_h	Hydraulic diameter, ($2W_{ch}D/W_{ch} + D$), (m)
De	Dean number
h	Heat transfer coefficient, (W/m^2. K)
Ha	Hartmann number, ($B_oD_h (\sigma/\mu)^{1/2}$)
HR	Helix radius
K_p	Permeability, (m^2)
λ	Thermal conductivity, (W/m. K)
L	Channel length
Nu	Nusselt number, ($Nu = hD_h/k$)
P	Pressure, (Pa)
q	Heat transfer rate, W
Re	Reynolds number, ($Re = \rho VD_h/\mu$)
T	Temperature, (K)
V	Velocity, (m/s)
W	Total Channel width
W_{ch}	Channel; width

Greek Symbols

α	Channel aspect ratio, (D/W_{ch})
σ	Electrical conductivity (S/m)
ρ	Density, (kg/m^3)
μ	Viscosity, (kg.m/s)
Ø	Volume fraction of nanoparticle

f	frequency, (rad/s)

Subscript

bf	Base fluid
bottom	Bottom
ch	Channel
eff	Effective
f	Fluid
m	Mixture
nf	Nanofluid
np	Nanoparticle
top	Top

CAD	:	Computer aided design
CFD	:	Computational fluid dynamics
CFOM	:	Coolant figures of metric
CPU	:	Central processing unit(s)
FVM	:	Finite volume method
GIT	:	Grid independence test
HMCHS	:	Helical microchannel heat sink
MCHS	:	Microchannel heat sink
TMCHS	:	Trapezoidal microchannel heat sink
SIMPLE	:	Semi-implicit method for pressure linked equations

CHAPTER 1: INTRODUCTION

The continued increase in power density and compactness of electronic chips has invoked the need for novel methods in lieu of more efficient and effective cooling solutions. Improper thermal management of electronic equipment may lead to six fundamental problems as outlined below (Berger, 2007):

- Reduced lifespan – Increase in product operating temperature reduces its lifetime
- Increased operating cost – Excessive cooling lead to increase in overall operating cost, i.e. bigger fans or compressor require more electricity.
- User comfort – Using larger fans lead to higher noise levels
- Reduced reliability – Products are more susceptible to failure at higher temperatures.
- Reduced performance – Central processing unit(s) (CPU) tend to lag at higher temperatures
- Higher manufacturing cost – Oversizing of cooling equipment require higher cost.

The stringent operational temperature requirements call for new heat dissipation techniques to address thermal issues. Microchannel heat sinks (MCHS) have been used as an effective heat dissipation device in the past and has proven to be a very efficient method to remove high heat loads. The novel idea of dispelling heat through the use of MCHS was first presented by Tuckerman and Pease (1981). The MCHS was fabricated using silicon to attain a higher heat transfer rate which is a direct implication of a lower thermal resistance. Deionized water was used as the working fluid in that study and a power density of 790 W/cm^2 was achieved which eventually resulted in the substrate temperature rise of 71^oC above the inlet water temperature. Reducing the overall channel

hydraulic diameter results in a larger heat transfer coefficient. The channel hydraulic diameter is inversely proportional to the heat transfer coefficient within a narrowed channel of laminar flow. Hence, a higher heat transfer coefficient can be achieved in a smaller channel. In addition, more channels of smaller size can be fabricated onto a heat sink block therefore leading to better overall heat transfer performance.

1.1 Applications and Heat Transfer Characteristics of MCHS

Numerous publications in the past have reported the superior heat transfer rate of MCHS compared to other conventional heat sinks and heat exchangers of much larger scale. The overall better thermal performance and smaller size make MCHS a preferred choice for electronic thermal management. The successful removal of high heat loads from the electronic devices is possible to the small channels which provide high surface area to volume ratio that allows for higher heat transfer rates.

Various techniques can be used to enhance the heat transfer rate which are divided into two major categories; active and passive methods. Active techniques include surface vibration, electric field, acoustic forces, injection and suction. Passive techniques include modification to the geometry and also use of inserts, surface treatments, and additives. This research will focus on the effects of both active and passive techniques on thermal performance of MCHS.

1.2 Problem Statement

The application of MCHS with the combination of various active and passive enhancement techniques seems to have a promising future technology for industrial use. The research interest related to MCHS increased significantly in the last decade, however, the number of technical publication reached a saturated level after year 2009 (Kandlikar, 2012). Many aspects of MCHS still remains vague till date and further research is

required before the combination of these technologies are put into valuable use to cater for the ever increasing heat loads of processors. Although the promised advantages of using MCHS in conjunction with other active and passive enhancement methods, the disadvantages should not be discounted, such as pressure drop, economic viability and environmental impact. A worldwide common understanding needs to be established through further research in order to improve the viability of this technology.

1.3 Scope of Study

A thorough literature review is done in the preliminary stages of the research where the core focus was the techniques used in the past to improve the overall thermal performance of MCHS. MCHS review encompasses the various numerical, experimental and analytical studies on the heat transfer and fluid flow characteristics by using different methods, geometries, fluids and external forces. Once the understanding in the previous mentioned topics is established, it is evident that not much research has been conducted in the field of magnetohydrodynamics (MHD), helical microchannel heat sink (HMCHS), two-phase nanofluid analysis, porous medium and transient velocity flow; so it can be fairly said that the knowledge in this area is still new. This study will be focused on analyzing the thermal and fluid flow characteristics of MCHS with the combination of other active and passive enhancement techniques.

1.4 Research Objectives

This study has carried out heat transfer and fluid flow analysis on various types of MCHS using CFD. The detailed objectives are:

1. To investigate heat transfer characteristics and fluid flow of water (working fluid) in different types of HMCHS in which the helix radius, pitch, number of turns and aspect ratios are varied.

2. To investigate the heat transfer effect of HMCHS and Al_2O_3-water nanofluid using the two-phase mixture model. The transient inlet velocity boundary conditions are also investigated.
3. To investigate heat transfer characteristics of water flow (working fluid) in a HMCHS filled with fluid saturated Porous medium.
4. To study the effect of external force, i.e., transverse magnetic field, on heat transfer characteristics of water flow in straight rectangular and trapezoidal MCHS.

1.5 Thesis Outline

This thesis contains 9 chapters. The organizations of the chapters are described in brief below.

Chapter 1 portrays an overview of the research which includes introduction of the research, problem statement, scope of the study and the research objectives.

Chapter 2 presents the literature review which was carried out on this research topic and it is mainly categorized into three core sections which are experimental, numerical and analytical studies on MCHS.

Chapter 3 to chapter 8 discusses 6 different problems on MCHS. The governing equations, boundary conditions and results obtained from this research which includes the effects of transverse magnetic field, helical geometry, porous medium, nanofluids, and varying inlet velocity conditions are given in detail.

Finally, chapter 9 contains the conclusions this research and the recommendations for future work.

CHAPTER 2: LITERATURE REVIEW

The demand for smaller electronic chips with higher power consumption has paved the way for various research activities to provide more efficient cooling. Cooling is required to maintain the chips at optimum temperature and to prevent it from burning. Heat transfer enhancement in micro-scale is a challenging problem and is an active area of research due to many applications. Literature review was carried out to eliminate the knowledge gap in this field of study. A critical analysis of previous experimental, numerical and analytical works has been outlined in the following sections.

2.1 Experimental Analysis

Tuckerman and Pease (1982) further discussed the challenges associated to microchannel cooling such as headering and coolant selection. Coolant figures of merit (CFOM) were proposed to optimize the heat transfer coefficient for either a given coolant pressure or constant pumping power.

Wu and Little (1983) and Wu and Little (1984) conducted a study to determine the friction factor of gas in both rectangle and trapezoidal MCHS. The channel depth and width were varied from 28 to 65μm and 133 to 200 μm correspondingly. It was found that the friction factor was higher in the laminar regime as compared to the predicted value. Also, transition takes place between Re = 350 and 900 depending on surface roughness. However, the friction factor for turbulent regime was found to be indecisive. It was also concluded that the Nusselt number varied rapidly with Reynolds number in the fully developed laminar region. As for the turbulent flow, the Nusselt number was higher than the predicted one.

Pfahler et al. (1989) and Pfahler et al. (1990) experimentally investigated the laminar fluid flow through a trapezoidal MCHS using various types of fluid. The Poiseuille number, (*fRe*) increases in increasing the Reynolds number; however it was generally lower than the predicted value. Rahman and Gui (1993a) and Rahman and Gui (1993b) experimentally investigated forced convection of water thorough a trapezoidal MCHS. It was found that the Nusselt number in laminar flow was much higher as compared to that of turbulent flow and no extreme change was observed in the transition region. The critical Reynolds number was in good agreement with theory but it stretched out for turbulent flow in the experiment performed by Gui and Scaringe (1995).

Peng and Peterson (1996) conducted an experimental study to investigate the single-phase forced convective heat transfer and flow characteristic in a rectangular MCHS using water. Based on the result obtained, it was concluded that the geometry was a key factor to determine the heat transfer and fluid flow characteristics. Empirical correlations were proposed for the Nusselt number and friction factor for laminar, transition and turbulent flows.

Harms et al. (1999) conducted a study on developing convective heat transfer in deep rectangular microchannel. Deionized water was used as the working fluid with Reynolds number ranging from 173 to 12900. The Nusselt number results were found to be similar with the classical channel flow theory. Apart from that, the results indicate that microchannel systems designed for developing laminar flow performed then the channel systems designed for turbulent flow.

Weilin et al. (2000) experimentally analyzed the flow characteristics of water through trapezoidal silicon microchannels with hydraulic diameters ranging from 51 to 169 μm. Significant differences in the experimental results were observed when compared with

conventional laminar flow theoretical predictions. The authors suggested that the difference may be due to the effect of surface roughness.

Qu and Mudawar (2002b) conducted both numerical and experimental study to determine the pressure drop and heat transfer characteristic in a single-phase water-cooled MCHS of height and depth of 231μm and 713 μm respectively. Early transition of laminar to turbulent was not observed in the range of Reynolds number which was from 132 to 1672. It was noted that Reynolds number affects the pressure drop and temperature dependence viscosity of water. Temperature distribution of experimental data was in decent agreement with numerical predictions.

Lee et al. (2005) conducted an experimental investigation to validate classical correlations used for conventional sized channels in order to predict thermal characteristics of a single-phase flow through rectangular copper microchannels. The range of the microchannel width considered was from 194 to 534 μm where the channel depth was set to be five times of the width for each respective case. Deionized water was allowed to flow in a parallel configuration through ten rows of channel. They concluded that the previous numerical predictions are fairly close with experimental results. Cho et al. (2010) found that straight microchannels are less sensitive in terms of temperature distribution as compared to diverging microchannels. However, the pressure drop in straight channels are higher compared to the latter. For the case of trapezoidal channels, the inverse was observed.

Mathew and Hegab (2012) conducted an experimental study to investigate the accuracy of their previously proposed thermal model (Mathew and Hegab, 2010). They concluded that the experimental results perfectly match the theoretical model irrespective of the parameters investigated. Zhang et al. (2013) conclude that the pressure drop and

heat transfer performance of fractal-like microchannel network are affected by other parameters such as branching level and aspect ratio. Ho and Chen (2013) experimentally studied the thermal performance of Al_2O_3- water based nanofluid in a minichannel heat sink. They found that nanofluid cooled heat sinks outperformed water cooled heat sinks.

Ho et al. (2014a) experimentally investigated the heat transfer characteristics of Al_2O_3-water based nanofluid in a rectangular natural circulation loop with a mini-channel heat sink. They found that nanofluid enhances the heat transfer performance of the natural circulation loop considered. In another separate study, Ho et al. (2014b) experimentally studied the thermal performance of water-based Al_2O_3 nanoparticles and microencapsulated phase change material (MEPCM) particles in a minichannel heat sink. Enhancement was observed due to the simultaneous increase in the effective thermal conductivity and specific heat. Other experimental studies (Ho et al., 2014c) also show significant heat transfer improvement with the presence of nanofluid.

Wang et al. (2015) performed and experimental and numerical study on a MCHS with micro-scale ribs and grooves. The Nusselt number of rib-grooved channel were 1.11-1.55 times higher than smooth channels. Azizi et al. (2015) conducted an experimental study on a cylindrical MCHS using Cu-water based nanofluid. They observed thermal enhancement on increasing the nanoparticle concentration.

2.2 Numerical Analysis

Chen et al. (1998) conducted a numerical study on gas flow through microchannels. Nitrogen and helium was considered as the working fluid in their study with a Knudsen number of 0.055 and 0.165 at the channel outlet. It was found that a large pressure gradient was required to drive the flow due to the extreme small size of the channel. Though the pressure gradient was large, the magnitude of the velocity remains small as a

result of high wall shear stress.

Fedorov and Viskanta (2000) numerically investigated the three-dimensional incompressible laminar conjugate heat transfer in a microchannel heat sink that is used in electronic packaging applications. The model was validated with the existing thermal resistance and friction factor data. They found that the Poiseuille flow assumption is not always accurate and careful assessment is needed to evaluate its validity to ensure minimal errors in predicting friction coefficients.

Ambatipudi and Rahman (2000) numerically examined the heat transfer through a silicon microchannel. They concluded that the higher Nusselt number was obtained for the design with greater number of channel and higher Reynolds number. The maximum Nusselt number was achieved for a channel depth of 300 μm at Re = 673. Qu and Mudawar (2002a) performed a numerical analysis to examine three-dimensional heat transfer in MCHS. The temperature rise was approximately linear with the flow direction in both solid and fluid region which result in significantly higher Nusselt number and heat flux at the channel inlet. Whereas at the edge of the channel, the Nusselt number and heat flux varied and reached zero at the corner. The authors also outlined that the solution of fin approach has a big variation from the real case even though it offers simplified solution for the heat transfer in MCHS thus may affect the accuracy of the result.

Zhao and Lu (2002) carried out a two-dimensional analytical and numerical study to analyze the heat transfer characteristic in a rectangular MCHS with forced convection. The porous and fin approach was used in the analytical method for laminar flow ($Re < 2000$) and turbulent flow ($Re \geq 2000$). It was found that both approach led to an increase of overall Nusselt number due to reduction in effective thermal conductivity ratio. Hence, fluid with higher thermal conductivity would have a higher overall Nusselt number.

Gamrat et al. (2005) numerically investigated the effect of conductance and entrance effect on heat transfer in a rectangular MCHS with high aspect ratio. The working fluid considered was water under laminar flow condition where the Reynolds number was varied from 200 to 3000. No significant scale effects on the heat transfer were seen in the numerical results up to the smallest scale considered. The contradicting experimental results were not discussed.

A numerical study was carried out by Sun et al. (2006) to investigate the pressure distribution and flow cross-over through the gas diffusion layer of a trapezoidal cross-section shaped microchannel. The authors concluded that the flow cross-over through the gas diffusion layer increases with the increase in size ratio and the size ratio had significant effect on the pressure variation for both cross-over and non cross-over cases.

Niazmand et al. (2008) studied the simultaneously developing velocity and temperature fields in the slip-flow region of a trapezoidal microchannel under constant wall temperature boundary condition. Large reductions in friction and heat transfer coefficients were observed in the entrance region and this was associated to the large amounts of velocity-slip and temperature jump. They also observed that the friction coefficient decreased on increasing the Knudsen number and aspect ratio in the fully developed region. In addition, heat transfer coefficient also decreased on increasing the aspect ratio and rarefaction.

Hong et al. (2008) numerically analyzed the subsonic gas flows through straight rectangular cross sectioned microchannel with patterned microstructures numerically. Analyses were carried for both three and two dimensional cases. It was noted that significant difference in results exist between the said cases for aspect ratios below 3. Similarity tends to take place at higher aspect ratios. Also, the cooling and heating effects

of the microstructure temperature on flow properties were enhanced on decreasing the Knudsen number. Raise et al. (2011) numerically investigated the forced convection of laminar nanofluid in a microchannel with both slip and no-slip condition. They reported that the solid volume fraction and slip velocity coefficient affects the heat transfer rate at high Reynolds number.

Hung and Yan (2012) numerically investigated the effects of tapered-channel on thermal performance of microchannel heat sink. They concluded that thermal resistance and width-tapered ratio was not monotonic at constant pumping power. A similar result was observed for the height-tapered ratio case as well. Cito et al. (2012) investigated the mass transfer rate in capillary-driven flow through microchannels. Wall mass transfer rate enhancement was observed due to recirculation.

Keshavarz Moraveji et al. (2013) numerically investigated the cooling performance and pressure drop in a mini-channel heat sink using nanofluids. Two different nanoparticles with various volume concentration and velocities were investigated. It was found that the heat transfer coefficient increased on increasing nanoparticle concentration and Reynolds number. Fani et al. (2013) presented the effect of nanoparticle size on thermal performance of nanofluid in a trapezoidal microchannel heat sink. CuO-Water nanofluid with 100-200nm and 1-4% concentration were considered. A significant increase in pressure drop was observed as the concentration was increased. Heat transfer was decreased with the increase of particle size. Emran and Islam (2014) conducted a numerical study on the flow dynamics and heat transfer characteristics in a microchannel heat sink. They observed that the highest temperature was at the bottom of the heat sink immediately below the channel outlet and the lowest at the channel inlet.

Konh and Shams (2014) conducted a numerical investigation on channel roughness using the second-order slip boundary condition. They observed that the second-order model is more reliable in predicting the channel roughness. Jessela and Sobhan (2015) numerically investigated the characteristics of two phase flow with liquid to vapor phase change in rectangular microchannels. They found that the two phase heat transfer coefficient increased on increasing the vapor quality. It was also noticed that the wall temperature decreased along the length of the channel. Arie et al. (2015) presented numerical results for optimized manifold-microchannel plate heat exchanger. The optimized heat exchanger showed superior heat transfer performance over chevron plate heat exchanger designs.

Zhang et al. (2015) numerically analyzed the fluid flow and heat transfer in U-Shaped microchannels. They concluded that the model with periodic boundary conditions is the optimal model to simulate heat transfer performance. Analysis on heat transfer, fluid flow and nanofluids have been studied extensively in the past (Ochende et al., 2010, Sivanandam et al., 2011, Nadeem et al., 2012, Xie at al., 2013, Yang et al., 2014), to name a few.

2.2.1 Effects of magnetic field

Aminossadati et al. (2011) numerically investigated the laminar forced convection through a horizontal microchannel under the influence of a transverse magnetic field. Al_2O_3-water based nanofluid was used as the working fluid and the microchannel was partially heated in the mid-section. Effects of Reynolds number, nanoparticle volume fraction and Hartmann number were investigated. The heat transfer increased on increasing Reynolds and Hartmann number.

Weng and Chen (2013) showed that the combined effects of non-zero electric field and negative magnetic fields can produce electromagnetic driving force which results in an additional velocity slip and flow drag. In another separate study,

Ganji and Malvandi (2014) presented the results for nanoparticle migration in a vertical enclosure with the presence of magnetic field. The Nusselt number decreased in the presence of magnetic field for the case of alumina/water and increased for titania/water. Malvandi and Ganji (2014a) further presented the results of alumina/water convective heat transfer inside a circular microchannel in the presence of magnetic field. Heat transfer enhancement was observed as a result of near wall velocity gradients increase. Further enhancement was observed as the magnitude of the magnetic field is increased for the case of nanofluid flow inside a vertical microtube (Malvandi and Ganji, 2014b).

2.2.2 Effects of curvature

Yang et al. (2005) investigated the flow characteristics of curved microchannels. They introduced a roughness-viscosity model to the classical Navier-Stokes equation to eliminate the discrepancy between the numerical and experimental data. Wang and Liu (2007) studied the effects of curvature in microchannels. Secondary flow was always present regardless of the curvature's magnitude which directly increased the mean friction factor and Nusselt number. Chu et al. (2010) studied the flow characteristics in a curved rectangular microchannel with different aspect ratio and curvature ratio. The pressure drop increases on decreasing the channel width and the effect increased at higher flow rates. The secondary flow due to curvature leads to higher pressure drop. Xi et al. (2010) conducted an experimental investigation to understand the flow and heat transfer characteristics in swirl microchannels of different rectangular cross sections. The friction

factor and average Nusselt number values obtained from the experiment did not agree well with previous correlations reported in the literature. Swirl microchannels lead to 50% thermal enhancement compared to straight microchannels.

A numerical investigation was carried out by Alam and Kim (2012) to study the mixing in curved microchannels with grooves on side-walls. The degree of mixing and effects of width and depth of the rectangular grooves were analyzed. They concluded that grooved microchannels lead to better mixing performance compared to smooth microchannels. Sheu et al. (2012) investigated the mixing of a split and recombine micro-mixer with tapered curved microchannels. The split structures of the tapered channels lead to the uneven split of the main stream and the reduction of the diffusion distance of two fluids. The mixing was intensified due to the impingement of one stream on the other. The staggered curved-channel mixer with a tapered channel achieved 20% higher mixing index compared to other channels with 50% higher pressure drop.

Chu et al. (2012) studied the characteristics of water through curved rectangular microchannels for different curvature and aspect ratio. They observed that classical Navier-Stokes equations were still valid for the incompressible laminar flow for curved microchannels. Alam et al. (2013) numerically investigated the mixing and fluid flow in a curved microchannel with several cylindrical obstructions. Mixing of water and ethanol were analyzed using Navier-Stokes and diffusion equations. The proposed micromixer portrayed better mixing performance compared to a T-micromixer with similar obstructions. Liu et al. (2013) presented a high-efficiency three-dimensional helical micromixer in fused silica for mixing applications in the chemical engineering field. Such devices were not considered for electronic cooling in the past due to challenges in

fabrication. With new technologies in place, such devices can be given consideration because of its proven high thermal performance on larger scaled applications.

2.2.3 Two-phase analysis

Lotfi et al. (2010) studied the forced convective heat transfer of nanofluid flow through horizontal circular tube. The numerical initiative was done to investigate the accurateness of the single-phase model, two-phase mixture model and two-phase Eulerian model against previous experimental work. It was concluded that the mixture model provided better results as compared to all the other models. Kalteh et al. (2012) numerically and experimentally studied the laminar convective heat transfer of Al_2O_3-H_2O nanofluid flow through a wide rectangular MCHS. The two-phase Eulerian–Eulerian model was adopted for the numerical study. It was proven that the two-phase numerical results were in good agreement with experimental results as compared to single-phase results with maximum error of 7.42% and 12.61%, respectively. Also, the velocity and temperature difference between the phases in the two-phase analysis was negligible. The average Nusselt number was increased on increasing the Reynolds number and volume concentration but was decreased with increase in nanoparticle size.

Abbasi et al. (2015) showed that the increase in heat transfer due to nanofluid concentration is lesser in turbulent flow compared to laminar flow by using the two-phase mixture model. Bahnermiri et al. (2015) presented the results of two-phase nanofluid flow in a sinusoidal wavy channel. The Nusselt number increased on increasing nanoparticles and Reynolds number.

Garoosi et al. (2015) presented the results for mixed convection of nanofluids in a square cavity using the two-phase mixture model approach. They observed that heat transfer can be enhance by using several configuration of heaters coolers. Saghir et al.

(2016) recently concluded that the single-phase model which was presented by Ho et al. (2010) is able to predict the heat transfer accurately in a square cavity.

2.2.4 Transient velocity condition

The effect of porous baffles and flow pulsation on a double pipe heat exchanger was numerically studied by Targui and Kahalerras (2013). They observed heat transfer enhancement due to the addition of an oscillating component to the mean flow structure. The peak performance was obtained for the case of pulsating hot fluid. Nandi and Chattopadhyay (2014) numerically investigated the simultaneously developing unsteady laminar fluid flow and heat transfer characteristics of water through a two dimensional wavy microchannel. The pulsating inlet fluid condition led to improved heat transfer performance with pressure drop within the acceptable limits. The aforementioned research was further continued by Akdag et al. (2014) using nanofluid via the single phase approach. The authors observed that increase in heat transfer performance on increasing nanoparticle volume fraction and amplitude of pulsation.

2.2.5 Effects of Porous Medium

Analysis of heat and fluid flow using porous medium has been studied extensively in the past (Ingham and Pop, 1998, Nield and Bejan, 1999, Ali, 2006, Vafai, 2011, Dalponte et al., 2012, Wang, 2013, McQuillen et al., 2012), to name a few. Zhao and Lu (2002) carried out a two-dimensional analytical and numerical study to analyze the forced convective heat transfer characteristic in a rectangular MCHS. The porous and fin approach was used for the analytical method for laminar flow ($Re < 2000$) and turbulent flow ($Re \geq 2000$). It was found that both approach led to an increase of overall Nusselt number due to reduction in effective thermal conductivity ratio. Hence, fluid with higher thermal conductivity would have a higher overall Nusselt number.

Jiang et al. (2004), presented experimental results of forced convection heat transfer in sintered porous plate channels filled with water and air. They observed that convective heat transfer was more intense for the sintered case as compared to the non-sintered. The local heat transfer coefficients were 15 times higher for water and 30 times for air due to reduced thermal contact resistance and higher effective thermal conductivity as a result of better thermal contact. Hooman (2008) analytically studied the fully developed forced convective flow in a rectangular channel with and without (Brinkman) porous medium. The Nusselt number increases on increasing porous medium shape parameter, aspect ratio and Prandtl number. The slip coefficient approached its maximum value for s>100. Singh et al. (2009) examined sintered porous heat sink used for cooling high-powered compact microprocessors. They found that the system was able to dissipate 2.9 MW/m^2 of heat flux with pressure drop of 34 kPa.

Chen and Ding (2011) analyzed the MCHS with non-Darcy porous medium saturated with Al_2O_3-H_2O nanofluid with different volume fractions. It was reported that the temperature distribution in the channel is insensitive to inertial forces. One the other hand, temperature distribution and thermal resistance of the fluid were significantly affected by inertial forces. Hung et al. (2013) studied the heat transfer analysis on three dimensional porous microchannel heat sinks with various configurations such as rectangular, outlet enlargement, trapezoidal, thin rectangular, block and sandwich. They concluded that the sandwich and trapezoidal distribution design lead to the best heat transfer efficiency, cooling and convective performance compared to all the other designs considered in the study. The presence of porous medium lead to additional pressure drop.

Liu et al. (2015) presented a lotus-type porous copper heat sink design for heat transfer enhancement. The MCHS structure with long cylindrical pores increase the

overall heat transfer coefficient leading to better heat transfer enhancement. Chuan et al. (2015) proposed a new a new MCHS with porous fins as a replacement for solid fins. The new design had a lower pressure drop compared to the latter due to "slip" of coolant on the channel wall.

Pourmehran el al. (2015) found that Cu-water nanofluid has better thermal performance compared to Al2O3-water nanofluid in a MCHS filled with porous medium. They also concluded that intertial force and volume flow rate has a direct relationship with Nusselt number enhancement. Dehghan et al. (2016) showed that heat transfer performance of MCHS can be enhanced by using rarefied porous inserts.

2.3 Analytical Analysis

Knight et al. (1991) performed an analytical study on MCHS performance using empirical correlation. They concluded that the thermal resistance can be reduced up to 35% that work of Tuckerman and Pease (1998) by using fin approach.

Tsai and Chein (2007) performed an analytical study on the performance of nanofluid-cooled microchannel heat sinks filled with porous medium. Copper-water and carbon nanotube-water nanofluids were used as the working fluid. They found that nanofluid was able to reduce the temperature difference between the MCHS bottom wall and bulk nanofluid, thus reducing the conductive thermal resistance. Significant increment in the thermal resistance was observed due to the higher viscosity of nanofluids as compared to other coolants.

Biswal et al. (2009) carried out an analytical investigation pertaining to various designing parameters of a rectangular MCHS. Single-phase laminar flow was considered

in their study for both fully developed and developing conditions to identify the Nusselt number and friction factor.

Kim and Mudawar (2010) developed detailed analytical heat diffusion models for a number of channel geometries of microchannel heat sink such as rectangular, inverse-trapezoidal, trapezoidal, triangular and diamond shaped cross-sections. The analytical results agreed fairly with two-dimensional numerical results for a range of Biot numbers. Wang et al. (2011) analytically optimized the geometry of a MCHS using the inverse problem method. The bottom section was heated up with constant heat flux of 100 W/cm^2 and fluid pumping power of 0.05W. A reduction in efficiency at high pumping power was observed in the optimized design. The optimized design had more channels, a bigger aspect ratio and a smaller channel width to pitch ratio.

2.4 Research Gap

Table 1 shows the summary of past literatures covered in this research. Since the pioneering efforts of Tuckerman and Pease (1981), research efforts in the field of MCHS gained strong attention aimed to further reduce the size and enhance the overall thermal performance. The research area related to single phase flow in MCHS have made significant advances in the past three decades with much work done to understand the fundamental mechanism of fluid flow through such devices (Kandlikar, 2012). Researches now are more focused on enhancing the thermal characteristics of MCHS.

Numerical predictions have proven to be a cost effective method in developing new designs and past literatures suggest better accuracy with two-phase models. Helical geometries on a micro scale level are investigated extensively in the chemical engineering field to facilitate liquid mixing. Prior studies did not tackle this effect which can be used to enhance heat transfer. This need is the starting point of this study, which looks at

different combination of other enhancement method such as porous media, nanofluids and pulsating flow with the secondary flow induced by the curved structure. In addition, very little effort has been found in the field of Magnetohydrodyamics (MHD) for the purpose of heat transfer enhancement.

Table 2.1: Summary of past MCHS studies

Author	Nature of work and observation
Experimental Work	
Tuckerman and Pease (1981)	• Pioneers of rectangular MCHS for high convective heat transfer applications.
Tuckerman and Pease (1982)	• Presented coolant figures of merit (CFOM) or given coolant pressure and pumping power. • Discussed headering, microstructure selection, fabrication, coolant selection and bonding.
Wu and Little (1983) & Wu and Little (1984)	• Studied the friction factor and Nusselt number in rectangular and trapezoidal MCHS. • Proposed a Nusselt number correlation; • $Nu = 0.00222\ \ \mathrm{Pr}^{0.4}\ \mathrm{Re}^{1.09}$
Pfahler et al. (1989) & Pfahler et al. (1990)	• Investigation on trapezoidal MCHS showed that Poiseuille number increased with increasing Reynolds number.
Rahman and Gui (1993a) & Rahman and Gui (1993b)	• Concluded that Nusselt number in laminar regime was higher than turbulent.

Table 2.1: continued

Peng and Peterson (1996)	• Proposed empirical correlations for water flow in <u>rectangular</u> MCHS. $Nu = 0.1165 \left(\frac{D_h}{W_c}\right)^{0.81} \left(\frac{H}{W}\right)^{-0.79} \mathrm{Re}_l^{0.8} \mathrm{Pr}_l^{1/3}$ - Laminar $Nu = 0.0072 \left(\frac{D_h}{W_c}\right)^{1.15} \left[1 - 2.42 \cdot (2 - 0.5)^2\right] \mathrm{Re}_l^{0.8} \mathrm{Pr}_l^{1/3}$ - Turbulent $f = \frac{C_{f,l}}{\mathrm{Re}^{1.98}}$ - Laminar $f = \frac{C_{f,t}}{\mathrm{Re}^{1.72}}$ - Turbulent
Harms et al. (1999)	• Analysis on <u>rectangular</u> MCHS. • Nusselt number obtained was similar to classical channel flow theory. • MCHS with laminar design perform better than turbulent flow design. • Correlations for Nusselt number and friction factor for respective dimensional length:

Table 2.1: continued

	$Nu_{N=1} = 5.39;\ x^* \geq 0.1$ $Nu_{N=1} = 5.16 + 0.02(x^*)^{-1.035};\ 0.01 \leq x^* < 0.1$ $Nu_{N=1} = 1.17(x^*)^{-0.401}\mathrm{Pr}^{-.0.044};\ 0.001 \leq x^* < 0.01$ $f_{app}\mathrm{Re} = (\mu_w/\mu_m)^{0.58}16/G + K_\infty/4x^+;\ 0.001 \leq x^* < 0.01$ $f_{app}\mathrm{Re} = 11.3(x^+)^{-0.202}\alpha^{-0.094};\ 0.02 \leq x^+ < 0.1$ $f_{app}\mathrm{Re} = 5.26(x^+)^{-0.434}\alpha^{-0..010};\ 0.001 < x^+ < 0.02$
Qu and Mudawar (2002b)	• Experimental and numerical study on rectangular MCHS. • Larger Reynolds number reduced the water temperature but with penalty in pressure drop. • Reynolds number affects pressure drop and temperature dependence of water viscosity.
Lee et al. (2005)	• Concluded that classical correlation can be used to calculate heat transfer characteristics in MCHS.

Table 2.1: continued

Numerical Work	
Fedorov and Viskanta (2000)	• Presented the temperature heat/heat flux distribution for 3D laminar conjugate heat transfer. • Deduced the Poiseuille flow assumption are not always accurate.
Ambatipudi and Rahman (2000)	• Nusselt number was higher for design with greater number of channels and higher Reynolds number.
Qu and Mudawar (2002a)	• Increasing the substrate thermal conductivity reduces heated surface temperature at the bottom. • Nusselt number and heat flux are higher at channel inlet. • The developing region increases with increasing Reynolds number.
Gamrat et al. (2005)	• Analysis of conductance and entrance effect on heat transfer in rectangular MCHS. • Entrance effect are dependent on Reynolds number and channel spacing separately.
Sun et al. (2006)	• The flow cross-over through the gas diffusion layer increases with the increase in size ratio • The size ratio had significant effect on the pressure variation for both cross-over and non cross-over cases. • Significant effect on pressure variation was observed due to flow cross-over. • Increase in Reynolds number leads to a minute increase in the flow cross-over.
Wang and Liu (2007)	• Secondary flow increases Nusselt number and friction factor.

Table 2.1: continued

Lotfi et al. (2010)	• Investigation on the accurateness of the single-phase model, two-phase mixture model and two-phase Eulerian. • Two-phase mixture model was the most accurate.
Aminossadati et al. (2011)	• 2D investigation of transverse magnetic field on MCHS heat transfer characteristics. • Heat transfer increases with Hartmann number.
Kalteh et al. (2012)	• Eulerian-Eulerian two-phase nanofluid analysis. • Results indicate better accuracy compared to single-phase approach.
Hung and Yan (2012)	• Thermal performance of MCHS with tapered channels.
Alam et al. (2013)	• Curved microchannel with cylindrical obstruction lead to better mixing compared to T-micromixer.
Keshavarz Moraveji et al. (2013)	• Single-phase nanofluid analysis on cooling performance and pressure drop. • Heat transfer coefficient increases on increasing nanoparticle concentration and Reynolds number.
Liu et al. (2013)	• Presented a high efficiency helical micromixer.
Fani et al. (2013)	• Eulerian-Eulerian two-phase nanofluid investigation. • Heat transfer decreased on increasing particle size.
Hung et al. (2013)	• Presence of porous medium lead to better thermal performance with increased pressure drop.
Nandi and Chattopadhyay (2014) & Akdag et al. (2014)	• Inlet pulsation effect improved heat transfer with significant reduction in pressure drop.

CHAPTER 3: METHODOLOGY

This chapter discusses the step-by-step methodology used to investigate the heat transfer and fluid flow characteristics of the MCHS. CFD software was used to solve all the differential equations numerically. The use of commercial CFD package to complete this research was due to the fact that the current CFD technology could solve laminar heat transfer related problems with high accuracy. CFD is known to effectively simulate flow in engineering related problems and as a results to this, major savings in cost can be attained. However, modification to the equations in the commercial CFD package is required to improve the accuracy of the results. The detailed equations which were modified is explained in the respective chapters.

3.1 CFD Modelling

The modeling process of heat transfer analysis of the MCHS is described in the following section briefly. Generally, the steps consist of geometry creation, meshing and setting up of boundary conditions which are solved numerically. The process is described below and also shown schematically in Figure 3.1.

3.1.1 Pre-processing

The first phase of the process which is known as *pre-processing* involves the creation of the geometry using a three dimensional CAD software which is the imported to GAMBIT (FLUENT grid generation package). Meshing is done in order to create tiny control volumes where discretized versions of the equations are solved. Hence, a fine mesh generation is required for accurate results. A mixture of hex/wedge structured and unstructured mesh was used for this research. The quality of the mesh is checked using the grid check option which is readily available in GAMBIT. A grid independence test (GIT) is performed in order to validate that the results is independent of the mesh size.

The temperature field across the MCHS are observed for each mesh size until the reduction in mesh size (increase in mesh quality), which did not affect the results. Finally, all the boundary conditions are defined and the model is exported to FLUENT for the next step.

3.1.2 Processing

The next step involved in the research is known as *processing* and it is carried out using Fluent 6.3, commercial CFD software. The mesh of the MCHS is read into the package and values are given for all the boundary conditions (mass flow inlet, wall, wall coupled for heat transfer and pressure outlet). Numerical parameters and solution algorithms are then defined accordingly. All necessary initial conditions for the analysis are defined for initiating the iteration process. Next, Fluent solves the conservation, transport and energy equations numerically. The discretized forms of the equations are solved iteratively by making use of the initial guesses values. Convergence criteria will be achieved once the *residual* is zero for every cell in the domain.

3.1.3 Post-processing

Finally, *post-processing* was done using Fluent's built in capability which enables users to obtain the thermal field and flow field with the aid of Tecplot 8.0.

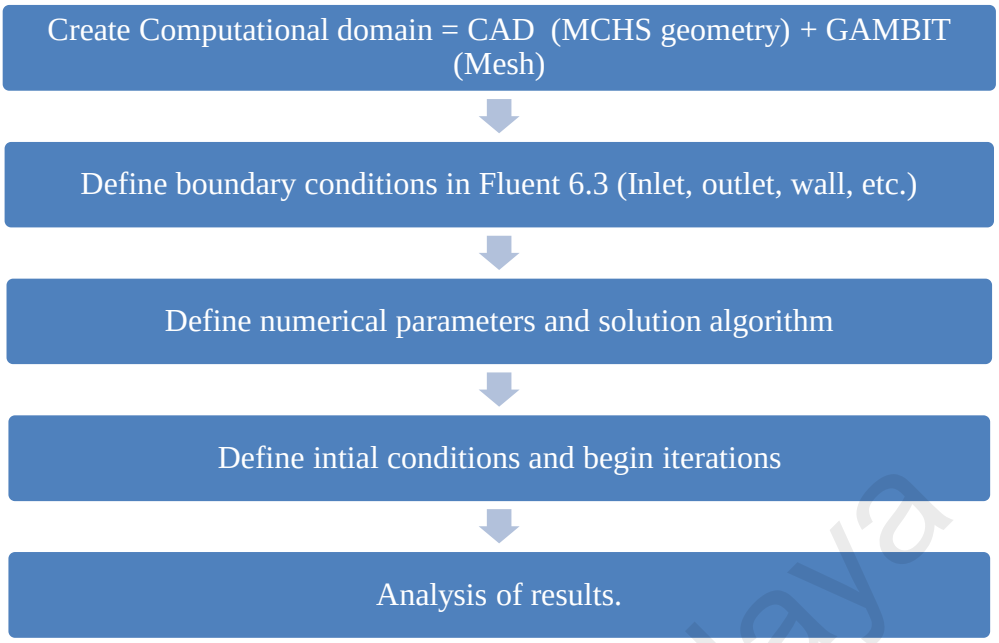

Figure 3.1: CFD modeling flow chart

3.2 Finite Volume Method (FVM)

Solving integral equation for the conservation of mass, momentum and energy analytically is very much complicated and tedious for a three dimensional problem, thus CFD is the alternative method to solve these equations more accurately and to save cost. The commercial CFD package uses control-volume approach to solve the equations and it consists of:

- The computational domain is divided into finite number of discrete control volumes using a computational grid as shown in.
- Integration of the governing equations over the individual control volume to construct algebraic equations for the discrete dependent variables (unknowns) such as velocities, pressure, temperature, and conserved scalars.
- Linearization of the discretized equations and solution of the resultant linear equation system to yield updated values of the dependent variables.

- The grid defines the boundaries of the control volumes while the computational node lies at the center of the control volume.
- The net flux through the control volume boundary is the sum of integrals over the four control volume faces (six in 3D).

3.3 Fluid flow using SIMPLE Algorithm

Problems associated with pressure-velocity coupling can be solved accurately by adopting an iterative solution strategy using the Semi-Implicit Method for Pressure Linked Equations algorithm method developed by Patankar and Spalding (1972). The sequence of operations of the SIMPLE algorithm is as follows (Versteeg and Malalasekara, 1995):

1. Set the boundary conditions.
2. Compute the gradients of velocity and pressure.
3. Solve the discretized momentum equation to compute the intermediate velocity field.
4. Compute the uncorrected mass fluxes at faces.
5. Solve the pressure correction equation to produce cell values of the pressure correction.
6. Update the pressure field:

$$p^{k+1} = p^k + urf.p' \tag{3.1}$$

where urf is the under-relaxation factor for pressure.

7. Update the boundary pressure corrections p'_b .
8. Correct the face mass fluxes:

$$\dot{m}_f{}^{k+1} = \dot{m}_f^* + \dot{m}_f' \tag{3.2}$$

9. Correct the cell velocities:

$$v^{\rightarrow k+1} = v^{\rightarrow *} - \frac{Vol\,\nabla p'}{a_P^{\rightarrow v}} \tag{3.3}$$

where $\nabla p'$ is the gradient of the pressure corrections, $a_P^{\rightarrow v}$ is the vector of central coefficients for the discretized linear system representing the velocity equation and *Vol* is the cell volume.

10. Update density due to pressure changes.

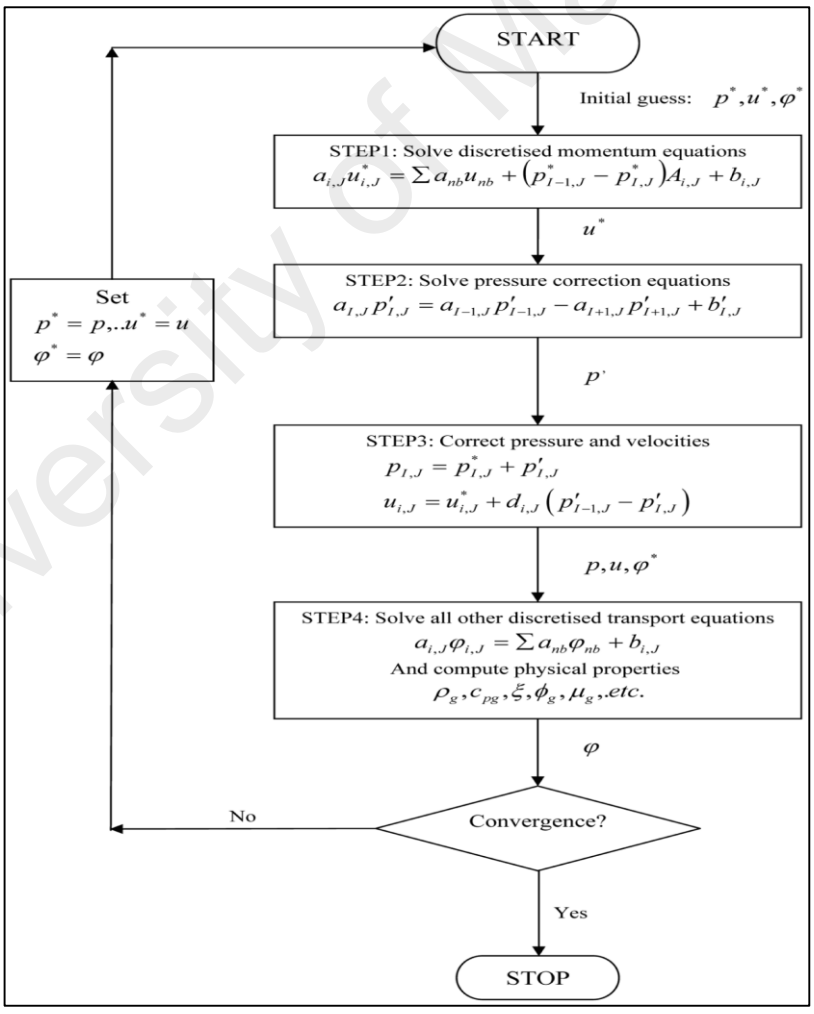

Figure 3.2: SIMPLE algorithm flow chart (Versteeg & Malalasekara, 1995)

CHAPTER 4: THERMAL AND HYDRAULIC CHARACTERISTICS OF HELICAL MICROCHANNEL HEAT SINK (HMCHS)

This chapter discusses the effects of using different geometrical parameters on heat transfer and fluid flow in a helically coiled microchannel heat sink (HMCHS). The performance of the HMCHS is compared to that of a straight channel of similar length, shape and hydraulic diameter. The effects of helix radius, pitch, number of turns and aspect ratio heat transfer and fluid flow characteristics are comprehensively investigated.

4.1 Mathematical Modeling

4.1.1 Governing equations

The helically coiled microchannel heat sink considered in this study is shown schematically in Figure 4.1. Heat is transferred from the outer wall of the HMCHS to the inner working fluid. Several assumptions are made on the operating conditions of the HMCHS: (i) the HMCHS operates under steady-state conditions; (ii) the fluid is incompressible and remains in single phase along the channel; (iii) the properties of the fluid and HMCHS material are temperature independent; (iv) the external heat transfer effects are ignored.

The governing equations for flow and heat transfer in the HMCHS are:

Continuity equation:

$$\nabla \circ \vec{v} = 0 \tag{4.1}$$

Momentum equation:

$$(\vec{v} \circ \nabla)\vec{v} = \frac{1}{\rho}\nabla p + \nu \Delta \vec{v} \tag{4.2}$$

Energy equation:

$$(\vec{v} \circ \nabla)T = \alpha \Delta T \tag{4.3}$$

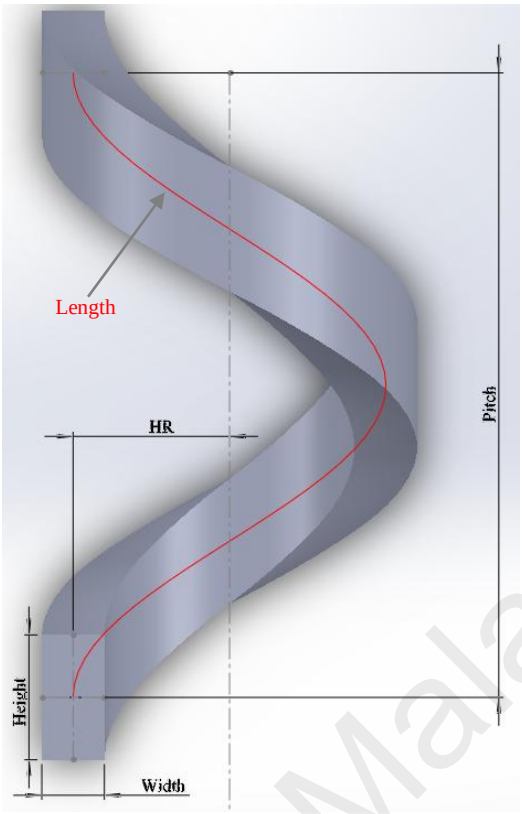

Figure 4.1: Schematic diagram of HMCHS (computational domain)

The length of the helical MCHS can be obtained using the following equation:

$$Length = \pi \times (2 \text{ x } HR) \times \text{Number of Turns} \quad (4.4)$$

4.1.2 Boundary conditions

The iso-flux boundary condition is applied on all four walls of the physical system. No-slip boundary conditions for velocity (*u, v, and z*) are applied on the solid walls. The inlet region is specified as mass flow rate boundary condition while the pressure outlet boundary condition is applied to the HMCHS outlet region. The governing equations along with the given boundary conditions are solved to obtain the fluid temperature distribution and pressure drop along the HMCHS. These data are then used to examine the thermal and flow fields along the HMCHS. . Individual parameters are investigated by making all others constant as shown in Table 4.1.

Table 4.1: Details of case setup.

Case	Values	Fixed Parameter
Helix Radius	0.15 0.20 0.25 0.30	Pitch, 1mm Turns, 7 Aspect Ratio, 2
Pitch	0.5 1.0 1.5 2.0	Helix Radius, 0.25mm Turns, 7 Aspect Ratio, 2
Turns	7 8 9 10	Helix Radius, 0.25mm Pitch, 1mm Aspect Ratio, 2
Aspect Ratio	1.5 2.0 2.5 3.0	Helix Radius, 0.25mm Pitch, 1mm Turns, 7

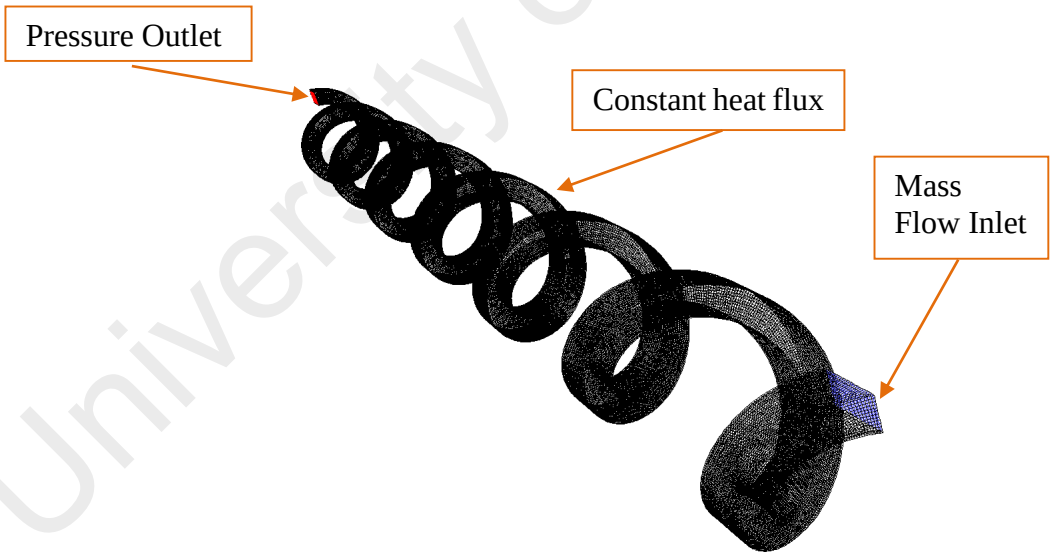

Figure 4.2: Boundary conditions

4.1.3 Numerical Method

Water was set to flow through the microchannel inlet. Four different values of inlet mass flow rates are used for the investigations, 0.00008, 0.00012, 0.00016 and 0.00020 kg/s. The range of mass flow rate is chosen based on some preliminary analysis. The

intensification of the secondary flow is not evident at very low mass flow rates. At higher mass flow rates, it is not suitable for the laminar flow assumption of this study. The outlet is set as "pressure outlet" boundary condition. Laminar flow was considered and the inlet temperature of the water is set to 300K. The outer wall of the HMCHS is set to a constant heat flux of 1×10^6 W/m^2. The convergence criterion required that the maximum relative residual for mass, momentum and energy to be smaller than 1×10^{-6}. Second order discretization scheme is used for pressure, momentum and energy equations. The under-relaxation factor parameters for pressure and momentum is set to 0.3 and 0.7 respectively.

4.1.4 Grid Independence Test (GIT)

The geometry modelling and grid generation are done using a commercial software, Gambit 2.3. A grid sensitivity analysis is performed to evaluate the effects of grid sizes on the results. Hexagonal mesh of 7 262, 0.29 million, 0.68 million and 1.77 million nodes are considered. The inlet temperature of the channel is set to 300 K with a velocity of 4 m/s. A constant heat flux of 1×10^6 W/m^2 is applied to the outer wall. The error for each mesh size is calculated respective to the 1.77 million nodes model. As shown in Table 4.2, the 1.77 million and 0.68 million nodes grid produce almost identical results along the MCHS with an error of 0.09%. Therefore, a domain with approximately 0.5 to 0.6 million nodes is chosen for all other cases to reduce computing time.

Table 4.2: Grid independence test results.

Nodes	Outlet Temperature (K)	Error (%)
7 262	319.779	2.18
292 317	313.897	0.30
684 632	313.222	0.09
1 773 648	312.943	-

4.1.5 Curved (i.e. semicircle MCHS Model Validation

The model validation for the curved structure is done based on the geometry which was presented by Chu et al. (2012). The channel's height and width is 200 µm respectively with 5000 µm radius of curvature and a curvature ratio of 0.04. The inlet temperature is set to 300 K for a range of Reynolds number. The flow field results (Figure 4.3) are accurate at lower Reynolds number but tend to slightly deviate at larger Reynolds number with a maximum error less than 10% which is deemed acceptable due to uncertainties in numerical and laboratory measurements (Hao et al., 2008). The discrepancy is likely due to the dominant inlet, exit and surface roughness effect at higher Reynolds number (Tsuzuki et al., 2014).

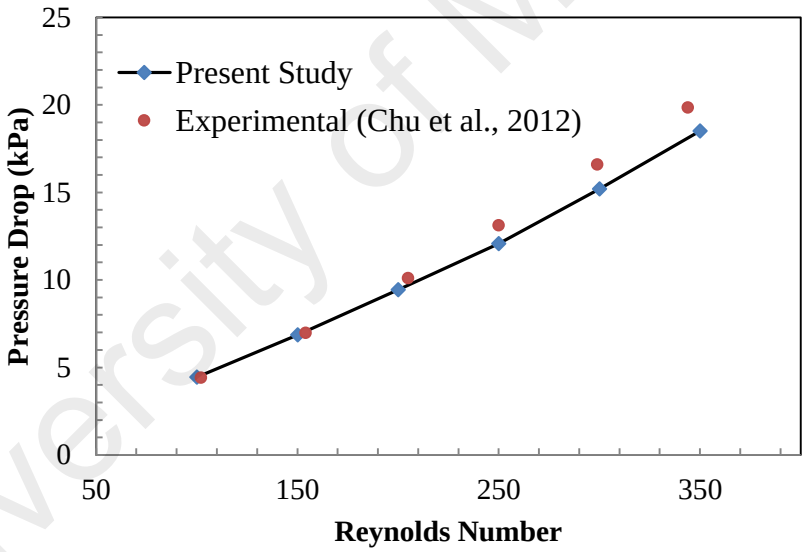

Figure 4.3: Model validation results for curved (i.e. semicircle) MCHS

4.2 Results and Discussion

4.2.1 The effects geometry on thermal field

The effects of different geometrical parameters on the thermal fields are presented by means of the Nusselt number as depicted in Figure 4.5. The local convective heat transfer coefficient and Nusselt number is calculated using the following equation:

$$h(x) = \frac{q}{(T_{Wall}(x) - T_{Fluid}(x))} \tag{4.5}$$

$$Nu(x) = \frac{h(x)D_h}{\lambda} \tag{4.6}$$

where q represents heat flux, h is the heat transfer coefficient, D_h is the hydraulic diameter and λ is the thermal conductivity of the working fluid. The average Nusselt number can be obtained by:

$$Nu = \frac{1}{L}\int_0^L Nu\,(x).dx \tag{4.7}$$

where L represents the channel length.

It can be deduced from the figure that the Nusselt number for the HMCHS is much higher compared to the straight microchannel. Since the hydraulic diameter, length and the heat flux for both the HMCHS and straight microchannel is similar, it is evident that a slight helix curvature (i.e. HR = 0.30 mm) can lead to heat transfer enhancement. A secondary flow is generated perpendicular to the curved central axis of the curved geometry. A pressure gradient is created across the pipe to balance the centrifugal force which is exerted on the fluid due to the curved trajectory of the geometry (Cuming, 1955). The pressure will be higher at the outer wall compared to the inner wall as shown in Figure 4.4.

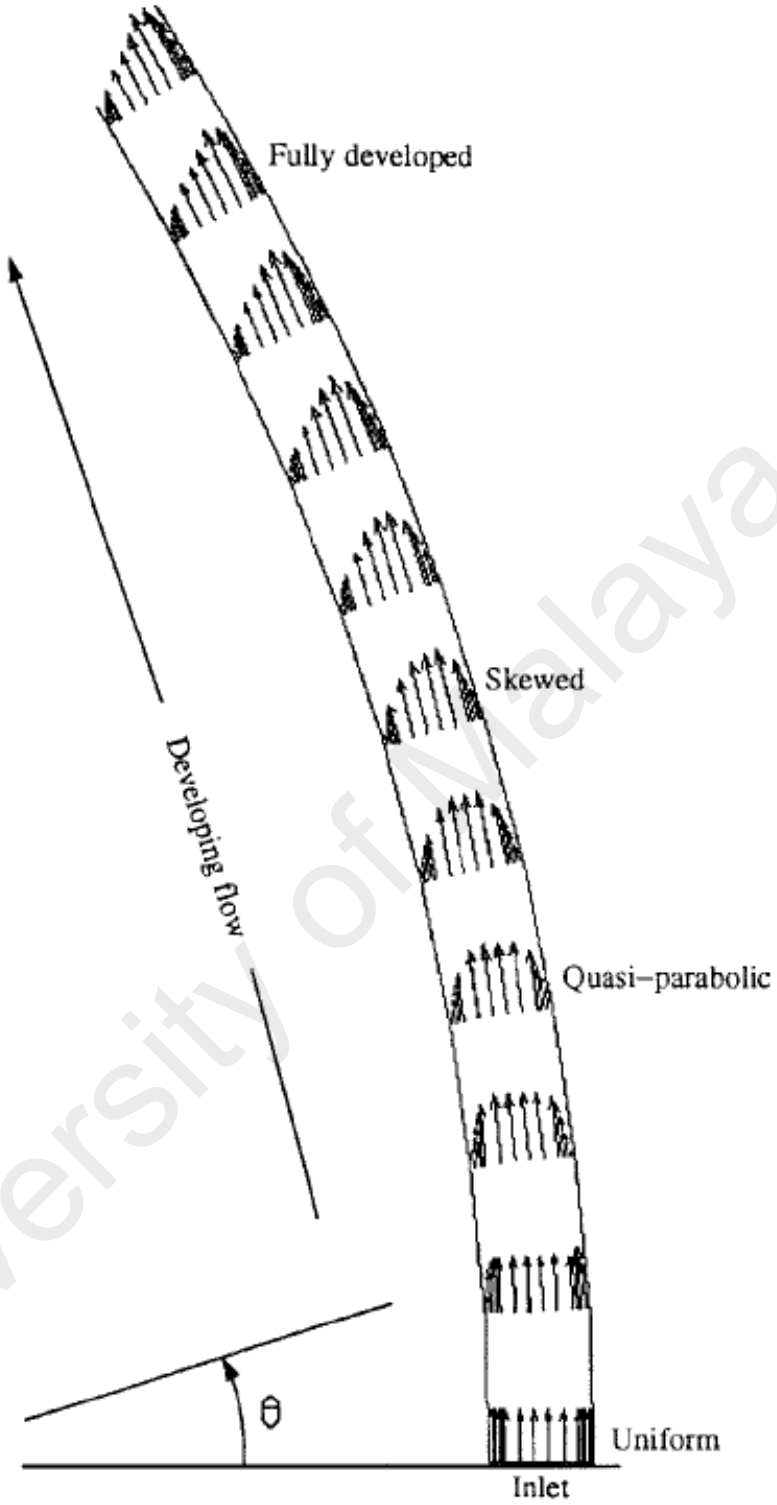

Figure 4.4: Axial velocity patterns for curved geometries (Guan & Martonen, 1997).

The fluid at the walls will be moving slower than the core region due to viscosity effects. The difference in pressure gradient will lead to the secondary flow being generated, whereby the fluid near the walls of the channel moves inwards towards the center of curvature of the central axis and the fluid near the core region move outwards. The difference in pressure gradient is further intensified as the helix radius is reduced. Such effects does not exist in straight channels because a pressure gradient is not created.

For the case of the HR = 0.30, 189% increment in Nusselt number is achieved compared to the straight microchannel (simulated case) at 0.00008 kg/s mass flow rate. The Nusselt number also increases on increasing the mass flow rate for all cases.

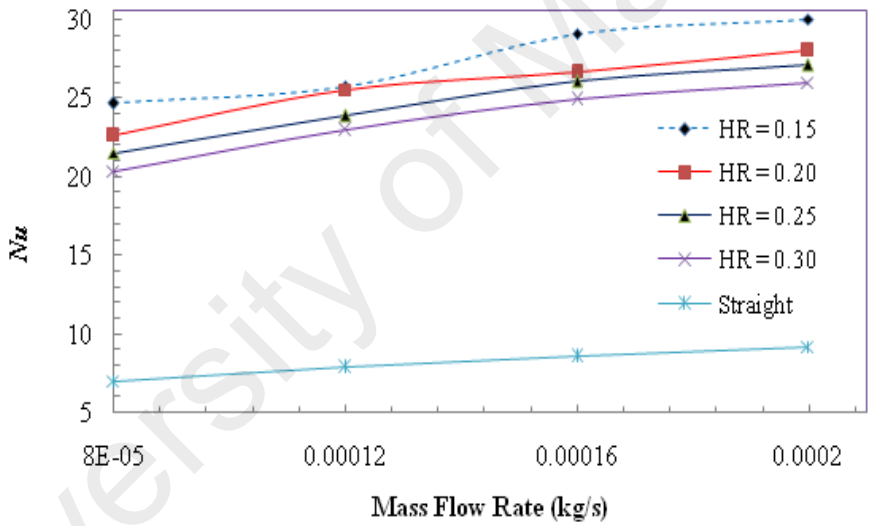

Figure 4.5: Variation of average Nusselt number vs. mass flow rate for straight microchannel and helical microchannel with various helix radius (Constants; Pitch = 1mm, Turns = 7, $\alpha = 2$).

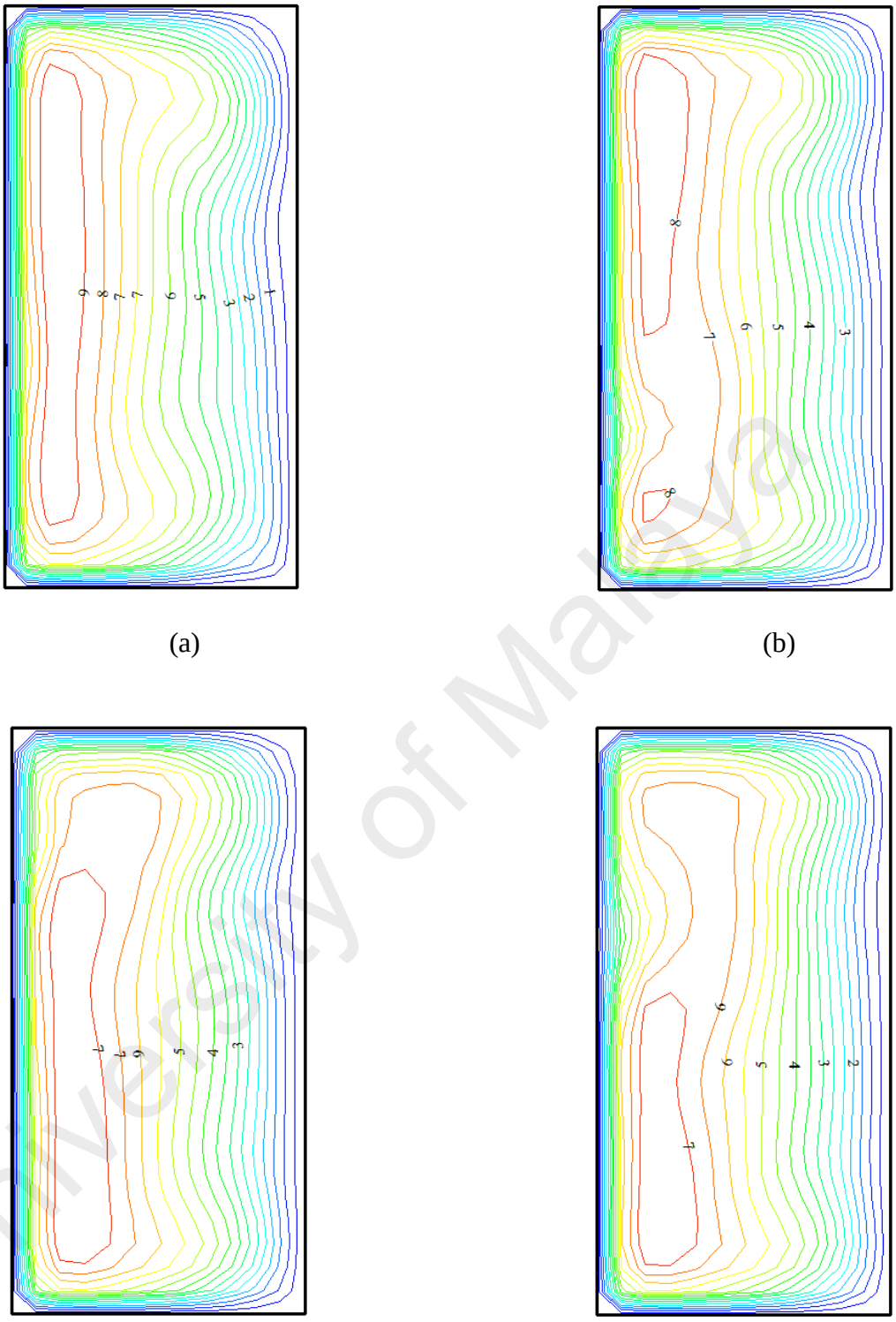

(a) (b)

c) (d)

Figure 4.6: Velocity (m/s) contour (at mid-section) for (a) HR = 0.15 mm, (b) HR = 0.20 mm, (c) HR = 0.25 mm. (d) HR = 0.30 mm at $\dot{m} = 0.00008\ kg/s$ (Constants; Pitch = 1mm, Turns = 7, α = 2)

Further enhancement in convective heat transfer is observed as the helix radius is further reduced. As the helix radius is decreased, the secondary flow is intensified based on the Dean number ($De = Re\sqrt{\frac{r}{HR}}$). Hence, the secondary flow plays a major role in passive enhancement. The secondary flow intensification can be further validated via the velocity contour as shown in Figure 4.6. It can be seen from the figure that magnitude of the secondary flow is much larger for the channel with smaller helix radius. Similar trends are also observed by Mohammed and Narrein (2012) for macro-scaled tubes.

The pitch of a helical coil is the distance of one complete helix turn measured along the helix axis. The effect of pitch variation on heat transfer rate is shown in Figure 4.7. The pitch of the coil will lead to an additional torsion force which enhances heat transfer. Previous studies suggest that torsion effect only exist for large turbulent flows for macro-scale devices (Yang & Ebadian, 1996). However, it can be inferred from this study that torsion effect does exist for laminar flow in micro-scale devices. Increase in pitch leads to an increase in Nusselt number, but the increase is limited to a certain optimum value which differs with various flow rates (Yang & Ebadian, 1996). When increasing the values of pitch parameter in a helical geometry, the flow obstruction becomes lesser due to ease of flow. Therefore, the flow speed is increased due to low curvature and heat transfer is increased.

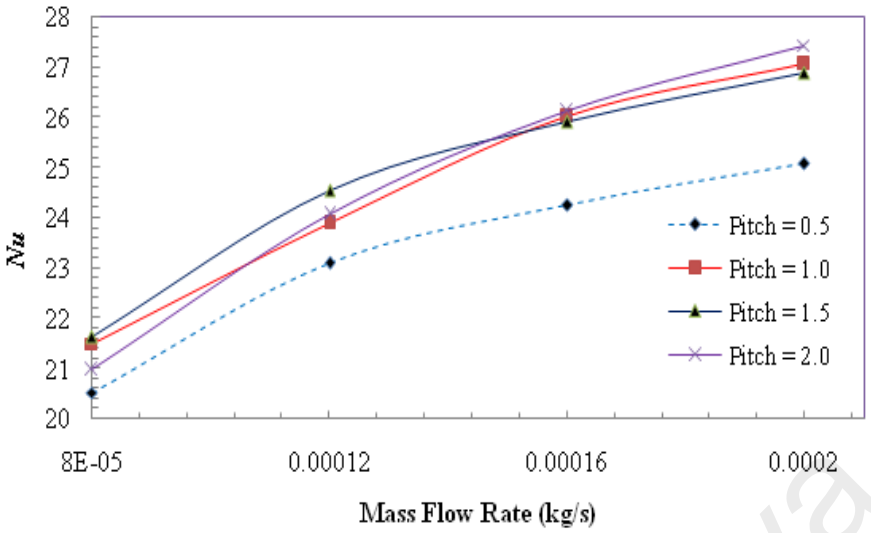

Figure 4.7: Variation of average Nusselt number vs. mass flow rate various pitch (Constants; HR = 0.25mm, Turns = 7, $\alpha = 2$).

The next parameter investigated is the number of turns and the result are portrayed in Figure 4.8. Very small changes in Nusselt number is observed as the number of turns are increased. However, the convective heat transfer tends to decrease slightly as the number of turns is increased. Similar effects are observed by Ali (2006) whereby the plenum rises from the first turn to the following turns successively, thereby reducing the effectiveness of the subsequent turns.

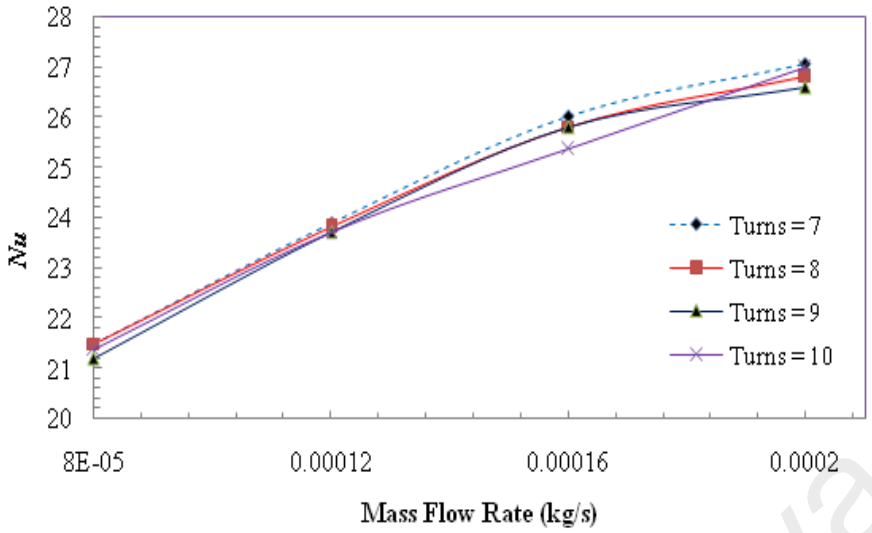

Figure 4.8: Variation of average Nusselt number vs. mass flow rate for various number of turns (Constants; HR = 0.25mm, Pitch = 1mm, α = 2).

Figure 4.9 shows that smaller aspect ratio provides better convective heat transfer enhancement for optimum flow rates. However, the Nusselt number for the channel with aspect ratio of 1.5 tends to drop at higher mass flow rates. This can be attributed to the residence time of the fluid whereby a minimum residence time is required for the fluid to effectively absorb heat (Narrein & Mohammed, 2013). Hence, the optimum residence time criterion is breached in this case. For other aspect ratios, the effect of velocity plays a more dominant role whereby the overall bulk velocity of the fluid is decreased on increasing the hydraulic diameter. Hence, the overall convective heat transfer is reduced with the drop in velocity.

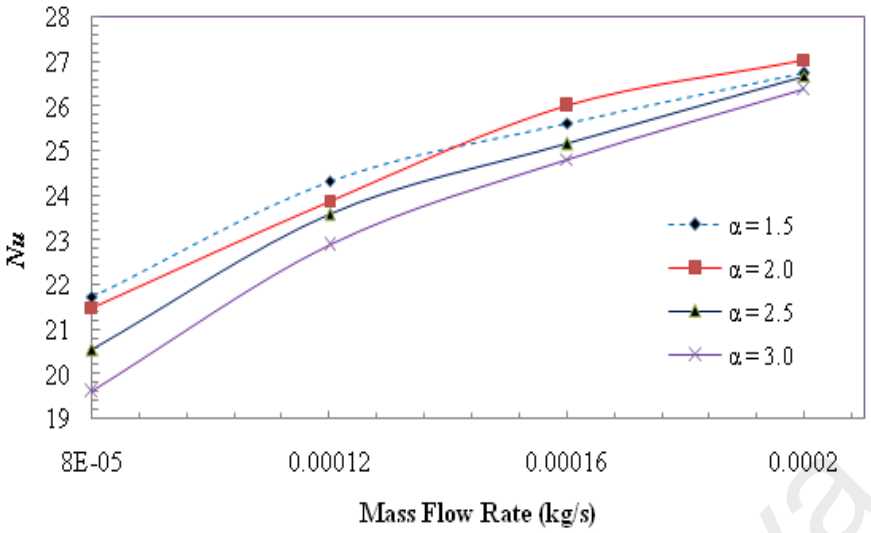

Figure 4.9: Variation of average Nusselt number vs. mass flow rate for various number aspect ratios (Constants; Pitch = 1mm, Turns = 7, HR = 0.25mm).

4.2.2 The effects of geometrical parameters on flow field

The net pressure drop across the HMCHS is used as an assessment metric to analyze the flow field performance. The pressure drop is obtained based on the area-weighted average value pressure of the inlet and outlet. Figures 4.10 through 4.13 show the pressure drop analysis for different geometrical parameters considered in this study. It can be inferred that pressure drop increases on increasing the mass flow rate for all cases. The pressure drop for different values of helix radius is portrayed in Figure 4.10. Generally, the pressure drop for all the HMCHS are significantly higher compared to the straight microchannel. The secondary flow induced may contribute to additional wall shear stress which leads to additional pressure drop.

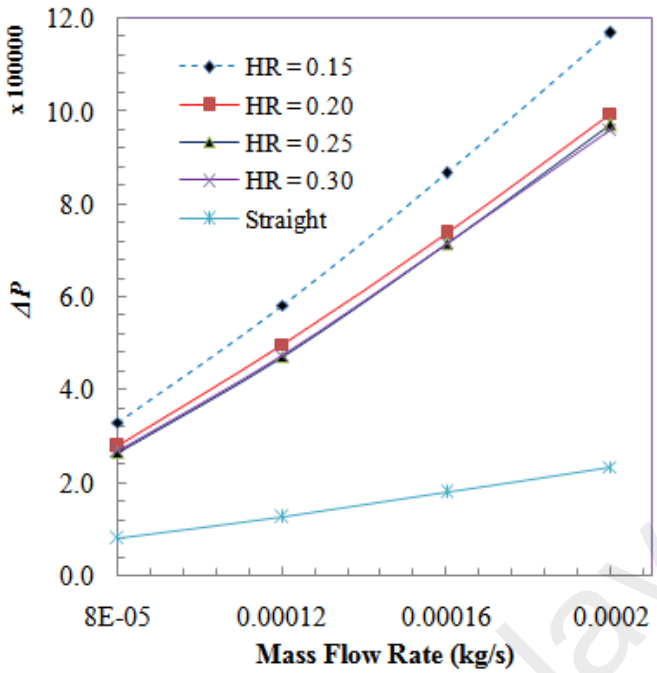

Figure 4.10: Pressure drop of different helix radius for various mass flow rates (Constants; Pitch = 1mm, Turns = 7, α = 2).

Similar effects are noticed for variation in pitch as shown in Figure 4.11. As the pitch is increased, the flow speed increases due the reduced curvature. At higher velocities, the shear stress is increased which leads to a higher pressure drop.

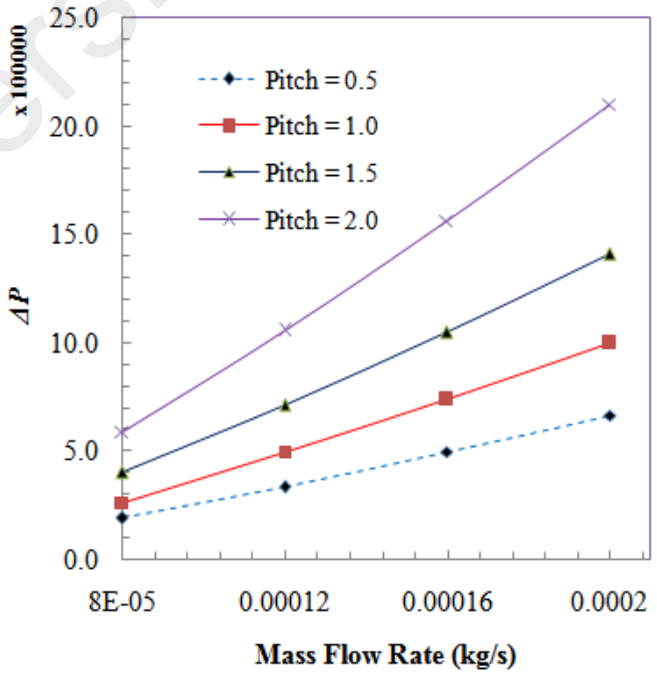

Figure 4.11: Pressure drop of different pitch length for various mass flow rates (Constants; HR = 0.25mm, Turns = 7, α = 2).

Increasing the number of turns also lead to additional pressure drop and this is due to the increase in overall length of the HMCHS as shown in Figure 4.12.

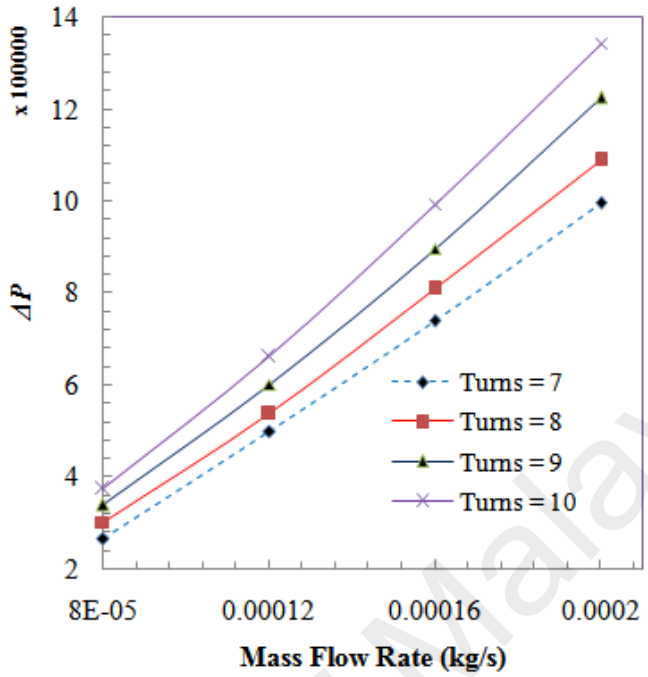

Figure 4.12: Pressure drop of different number of turns for various mass flow rates (Constants; HR = 0.25mm, Pitch = 1mm, α = 2).

It can be also observed that pressure drop increases on decreasing the aspect ratio as depicted in Figure 4.13. As the aspect ratio becomes smaller, the overall bulk velocity becomes higher which directly results in additional wall shear stress which in turn leads to higher pressure drop.

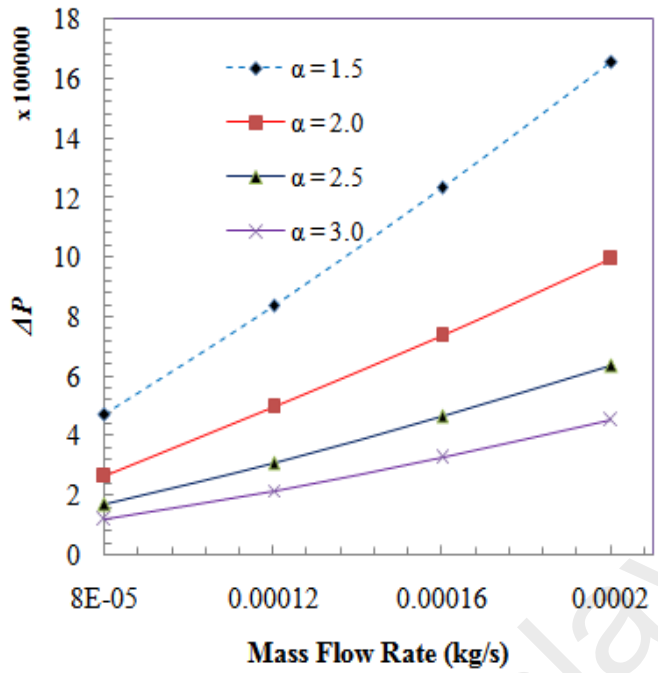

Figure 4.13: Pressure drop of aspect ratio for various mass flow rates (Constants; HR = 0.25mm, Turns = 7, Pitch = 1mm).

4.2.3 HMCHS performance

The performance index of the HMCHS is calculated using the following equation (Dang et al., 2011):

$$\eta = \frac{Q}{\Delta P} \tag{4.8}$$

where Q id the heat transfer and ΔP is the pressure drop. It is in an indication of the overall performance of the system based on pressure drop. It can be inferred from Table 4.3 that the overall performance index is significantly lower for all the HMCHS compared to the straight microchannel except for the channel with high aspect ratio (α = 3.0).

Table 4.3: Performance index based on various geometrical parameters.

Parameters	Effects		Performance Index (W/Pa) × 10^{-5}
Fixed	Straight		7.52
Pitch = 1.0,	Helix Radius	0.15	1.38
Turn = 7,		0.20	2.06
Aspect Ratio = 2		0.25	2.64
		0.30	3.10
HR = 0.2,	Pitch	0.5	3.50
Turn = 7,		1.0	2.64
Aspect Ratio = 2		1.5	1.85
		2.0	1.35
Pitch = 1.0,	Turns	7	2.64
HR = 0.2,		8	2.65
Aspect Ratio = 2		9	2.67
		10	2.68
HR = 0.2	Aspect Ratio	1.5	1.25
		2.0	2.64
		2.5	4.74
		3.0	7.66

The performance index tends to improve as the helix radius is increased. A larger helix radius will encounter a smaller magnitude of secondary flow which leads to smaller pressure drop. Performance index decreases on increasing the pitch. As the pitch is increased, the flow velocity becomes faster and this leads to additional pressure drop. Increasing the number of turns will lead to better overall heat transfer hence giving a better performance index value. The overall heat transfer rate, *Q* increases as a result of larger surface area. The pressure drop will increase as well. However, the percentage increase in *Q* is much higher compared to the percentage increases in pressure drop. It can be also seen that performance index increases on increasing the aspect ratio.

4.3 Conclusions

Numerical study on the performance of HMCHS based on various geometrical parameters are analyzed. The thermal field results show that HMCHS can contribute to better heat transfer enhancement as compared to a straight microchannel of similar length and hydraulic diameter. The results also showed that convective heat transfer tends to improve as the helix radius is reduced and when the pitch is increased. Increasing the overall length of the HMCHS leads to a higher pressure drop and lower convective heat transfer. Reducing the aspect ratio leads to an increase in the overall bulk fluid velocity which results to better convective heat transfer but with a penalty in pressure drop. The channel with the largest aspect ratio has the best performance index as compared to all other cases.

CHAPTER 5: TWO-PHASE ANALYSIS OF HELICAL MICROCHANNEL HEAT SINK USING NANOFLUIDS

This chapter discusses the heat transfer characteristic of Al_2O_3-water based nanofluid flow through helical microchannel heat sink (HMCHS). The two-phase mixture model with modified effective thermal conductivity and viscosity equations is employed for solving the problem numerically. The model developed is validated by comparing the results of Nusselt number with available experimental and numerical data for a wide range of Reynolds number. The detailed results for thermal field are reported for the effects of helix radius, pitch, number of turns and aspect ratio. The analysis presents a unique fundamental insight into the complex secondary flow pattern established in the channel due to curvature effects.

5.1 Mathematical Modeling

5.1.1 Governing equations

The helical microchannel heat sink considered in this study is shown schematically in Figure 5.1. Heat is transferred from the outer wall of the HMCHS to the nanofluid which flows through the channel. Several assumptions are made on the operating conditions of the HMCHS as follows: (i) the MCHS operates under steady-state conditions; (ii) the properties of the HMCHS material are temperature independent; (iii) the external heat transfer effects are ignored.

The simplified version of the Euler-Euler model is the mixture model. The transport equations in the mixture-model are based on mixture properties of density, velocity, viscosity etc. The phases are allowed to move with different velocities by introducing the slip velocity concept.

The governing equations for mass, momentum and energy two-phase mixture model are:

Continuity equation:

$$\nabla.(\rho_m \vec{v}_m) = 0 \tag{5.1}$$

where

$$\rho_m = \sum_{k=1}^{n} \emptyset_k \rho_k \tag{5.2}$$

Momentum equation:

$$\nabla.(\rho_m \vec{v}_m \vec{v}_m) = \nabla\rho_m + \nabla.[\mu_m(\nabla\vec{v}_m + \vec{v}_m^T)] + \rho_m\vec{g} + \nabla.(\sum_{k=1}^{n} \emptyset_k \rho_k \vec{v}_{dr,k}\vec{v}_{dr,k}) \tag{5.3}$$

where n is the number of phases, $\emptyset$ is the volume fraction and μ_m is the viscosity of the mixture:

$$\mu_m = \sum_{k=1}^{n} \emptyset_k \mu_k \tag{5.4}$$

and $\vec{v}_{dr,k}$ is the drift velocity for secondary phase *k* defined as:

$$\vec{v}_{dr,k} = \vec{v}_k - \vec{v}_m \tag{5.5}$$

Energy equation:

$$\nabla.(\sum_{k=1}^{n} \emptyset_k \vec{v}_k(\rho_k h_k + p)) = \nabla.(\lambda_{eff}\nabla T) \tag{5.6}$$

The representative viscosity for the nanoparticle is estimated as:

$$\mu_{np} = \frac{\frac{\mu_m}{\emptyset_{bf}\mu_{bf}}}{\emptyset_{np}} \tag{5.7}$$

where μ_m is given by (Corcione, 2012):

$$\frac{\mu_m}{\mu_{bf}} = \frac{1}{1-34.87\left(\frac{d_{np}}{d_{bf}}\right)^{-0.3}\emptyset^{1.03}} \tag{5.8}$$

Equivalent diameter of base fluid molecule (Corcione, 2012):

$$d_{bf} = \left[\frac{6M}{N\pi\rho_{bf}}\right] \tag{5.9}$$

The effective thermal conductivities for liquid and particle phases are estimated as (Kuipers et. al, 1992):

$$\lambda_{eff,bf} = \frac{\lambda_{bf}}{\emptyset_{bf}} \tag{5.10}$$

$$\lambda_{eff,np} = \frac{\lambda_{np}}{\emptyset_{np}} \tag{5.11}$$

where

$$\lambda_{bf} = (1 - \sqrt{(1 - \emptyset_{bf}}) \lambda_{bf} \, , \tag{5.12}$$

$$\lambda_{np} = 1 - \sqrt{(1 - \emptyset_{bf}}) (\omega A + [1 - \omega] \Gamma) \lambda_{bf} \, , \tag{5.13}$$

and

$$\Gamma = \frac{2}{1 - \frac{B}{A}} \left\{ \frac{B(A-1)}{A\left(1 - \frac{B}{A}\right)^2} \ln\left(\frac{A}{B}\right) - \frac{(B-1)}{(1 - \frac{B}{A})} - \frac{B+1}{2} \right\} \tag{5.14}$$

with

$$B = 1.25 \left(\frac{[1 - \emptyset_{bf}]}{\emptyset_{bf}} \right)^{10/9} \tag{5.15}$$

For spherical particles

$$A = \frac{\lambda_{np}}{\lambda_{bf}} \text{ and } \omega = 7.26 \, x \, 10^{-3} \tag{5.16}$$

5.1.2 Boundary conditions

The inlet section is specified as velocity inlet and the pressure outlet boundary condition is applied to the outlet region. No-slip boundary conditions are applied on the internal solid walls for velocity (*u, v* and *z*). Iso-flux boundary condition is applied on the external walls. These governing equations along with the specified boundary conditions are solved to obtain the fluid temperature distribution and pressure drop along the HMCHS. These data was then used to examine the thermal field along the HMCHS.

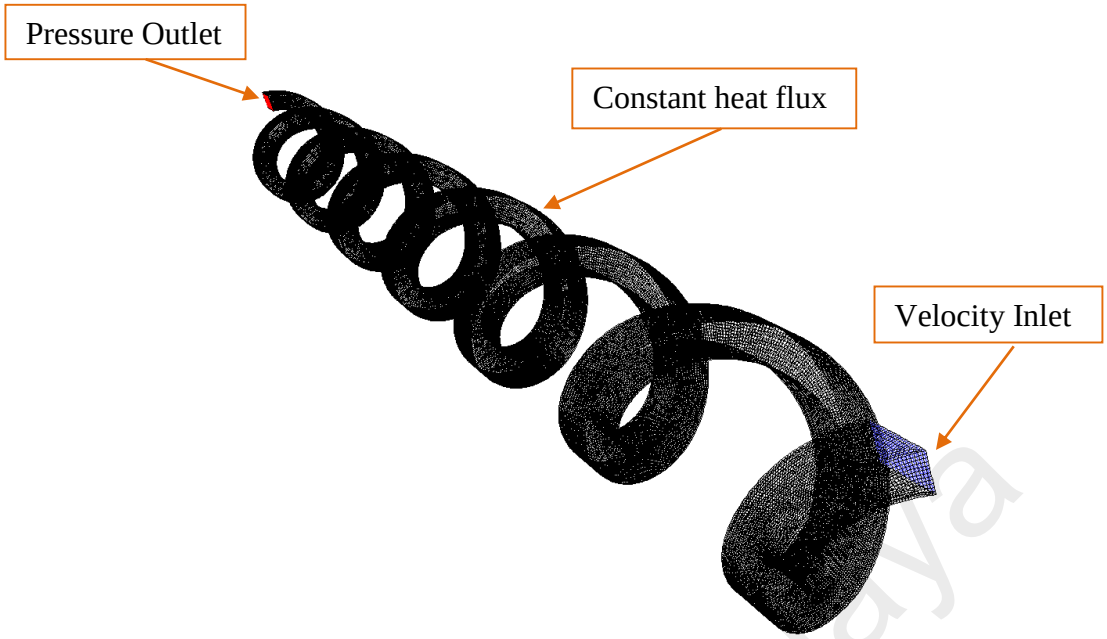

Figure 5.1: Schematic diagram of the computational domain of HMCHS

The inlet Reynolds number is varied from 5 to 25 and is kept to a minimum value since the accuracy of results might be affected at high Reynolds number due to entrance, exit and surface roughness effects. The Al_2O_3-water based nanofluid of 1% volume concentration and 42nm average diameter is used as the working fluid. The inlet temperature of the water is taken as 300K and constant heat flux of 5×10^4 W/m^2 is applied on the external walls. The properties of the nanoparticles are given in Table 5.1. Individual parameters are investigated by making all others constant as shown in Table 5.2.

Table 5.1: Properties of nanoparticle (Al_2O_3)

Physical property	Value
Volume concentrations, %	1%
Diameter, d_{np}	42nm
Density, ρ	3970
Specific heat capacity, C_p	535.6
Thermal conductivity, λ	11.47

Table 5.2: Details of case setup.

Case	Values	Fixed Parameter
Helix Radius	0.15 0.20 0.25 0.30	Pitch, 1mm Turns, 7 Aspect Ratio, 2
Pitch	0.5 1.0 1.5 2.0	Helix Radius, 0.25mm Turns, 7 Aspect Ratio, 2
Turns	7 8 9 10	Helix Radius, 0.25mm Pitch, 1mm Aspect Ratio, 2
Aspect Ratio	1.5 2.0 2.5 3.0	Helix Radius, 0.25mm Pitch, 1mm Turns, 7

5.1.3 Numerical Method

The numerical computations are carried out by solving the governing equations along with boundary conditions using the finite volume method. The SIMPLE algorithm is adopted to couple the velocity and pressure field. The second-order upwind differencing scheme is used for the convective terms. The original equation for two-phase mixture model over predicts the thermal conductivity and a viscosity value is also required for the solid phase as per Eq. 5.4. Hence, Eq. 5.7-5.16 is used to redefine the effective thermal conductivity and effective viscosity. Numerical simulation is carried out for different combinations of pertinent parameters such as helix radius, pitch, number of turns and aspect ratio to investigate the effects on the HMCHS. The convergence criterion required that the maximum relative residual for mass, momentum and energy to be smaller than 1×10^{-6}. Second order discretization scheme is used for volume fraction, pressure, momentum and energy equations. The under-relaxation factor parameters for pressure, momentum, slip velocity and volume fraction is set to 0.3, 0.7, 0.1 and 0.2 respectively.

5.1.4 Two-phase Nanofluid Analysis Model Validation

The two-phase mixture model method results were compared to the experimental work presented by Wen and Ding (2004). The tube considered has a diameter of 45 mm and a length of 970 mm with a constant inlet fluid temperature of 295 K.

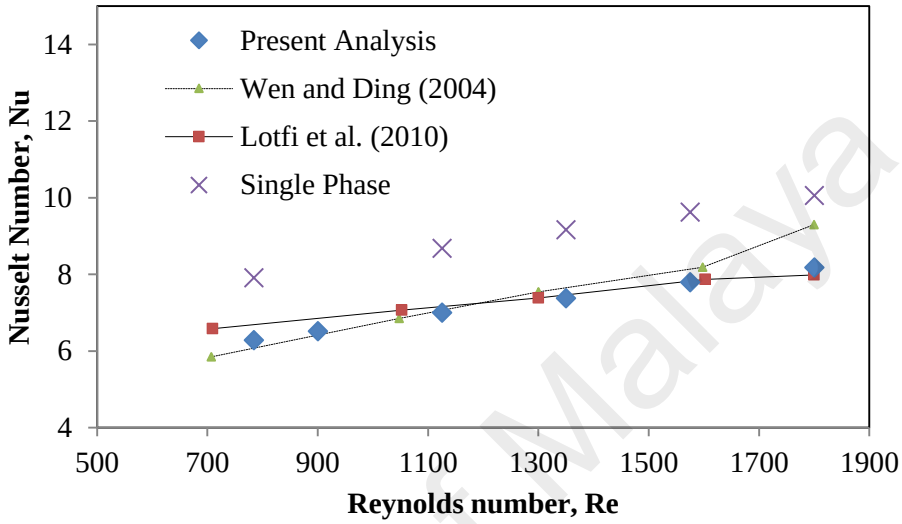

Figure 5.2: Two-phase model validation

The results for the two-phase mixture model (Figure 5.2) are in excellent agreement with the experimental (Wen and Ding, 2004) and numerical (Lotfi et al., 2010) results of past literatures. It is also evident that the single phase method over predicts the Nusselt number. The equation used to define the single phase nanofluid flow is given below:

Density (Ghasemi and Aminossadati, 2010):

$$\rho_{nf} = (1 - \emptyset)\rho_{bf} + \emptyset\rho_{np} \tag{5.17}$$

Heat Capacity (Ghasemi and Aminossadati, 2010)

$$(\rho c_p)_{nf} = (1 - \emptyset)(\rho c_p)_{bf} + \emptyset(\rho c_p)_{np} \tag{5.18}$$

Effective Thermal Conductivity (Ghasemi and Aminossadati, 2010):

$$k_{eff} = k_{Static} + k_{Brownian} \tag{5.19}$$

Static Thermal Conductivity:

$$k_{Static} = k_{bf}\left[\frac{k_{np}+2k_{bf}-2(k_{bf}-k_{np})\emptyset}{k_{np}+2k_{bf}+(k_{bf}-k_{np})\emptyset}\right] \tag{5.20}$$

Brownian Thermal Conductivity:

$$k_{Brownian} = 5x10^4\beta\emptyset\rho_{bf}c_{p,bf}\sqrt{\frac{\kappa T}{2\rho_{np}R_{np}}}.f(T,\emptyset) \tag{5.21}$$

where Boltzmann constant is:

$$\kappa = 1.3807x10^{-23}\ J/K$$

Modeling function (Al_2O_3), β (Vajha et al., 2010):

$$\beta = 8.4407(100\emptyset)^{-1.07304}\ for\ 1\% \le \emptyset \le 10\% \tag{5.22}$$

Modeling function, $f(T, \emptyset)$ (Vajha et al., 2010):

$$f(T,\emptyset) = (2.8217x10^{-2}\emptyset) + 3.917x10^{-3})\left(\frac{T}{T_0}\right) + (-3.0699x10^{-2}\emptyset - 3.91123x10^{-3}) \tag{5.23}$$

5.2 Results and Discussion

The heat transfer characteristics are presented by means of Nusselt number. The local convective heat transfer coefficient and Nusselt number is calculated using the following equation:

$$h(x) = \frac{q}{(T_{Wall}(x)-T_{Fluid}(x))} \tag{5.24}$$

$$Nu(x) = \frac{h(x)D_h}{\lambda} \tag{5.25}$$

where q represents heat flux, h is the heat transfer coefficient, D_h is the hydraulic diameter and λ is the thermal conductivity of the working fluid. The average Nusselt number can be obtained by:

$$Nu = \frac{1}{L}\int_0^L Nu\,(x).dx \tag{5.26}$$

where L represents the length of the channel.

Figure 5.3 shows the comparison between a straight microchannel and HMCHS of similar hydraulic diameter, length and heat flux. This shows that curvature effect can indeed lead to heat transfer enhancement.

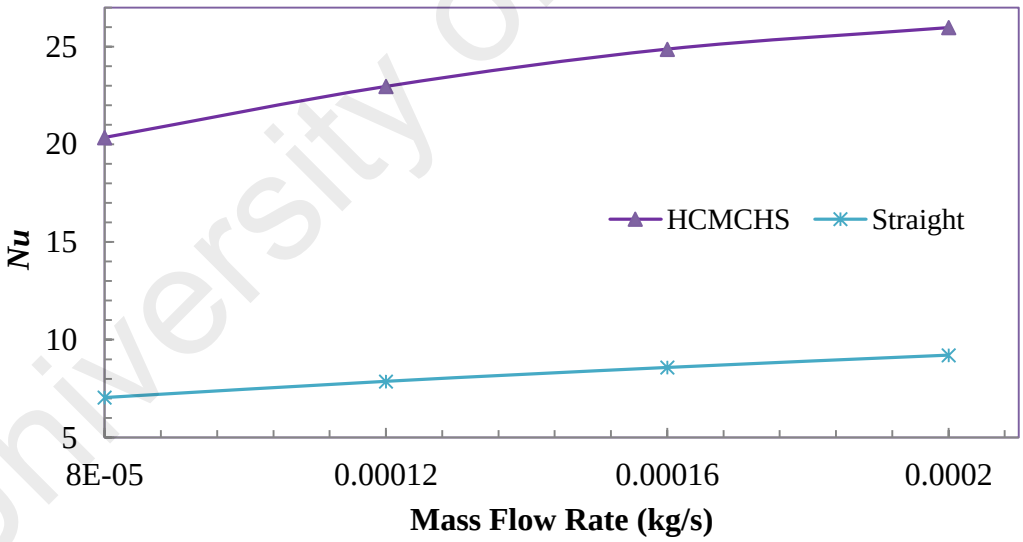

Figure 5.3: Comparison of Nu between straight MCHS and HMCHS with α = 2.0, HR = 0.30m, Pitch = 1.0 and Turns = 7

The effect of helix radius variation on the thermal field is shown in Figure 5.4. It is seen that the Nusselt number increases on increasing the Reynolds number and decreasing the helix radius.

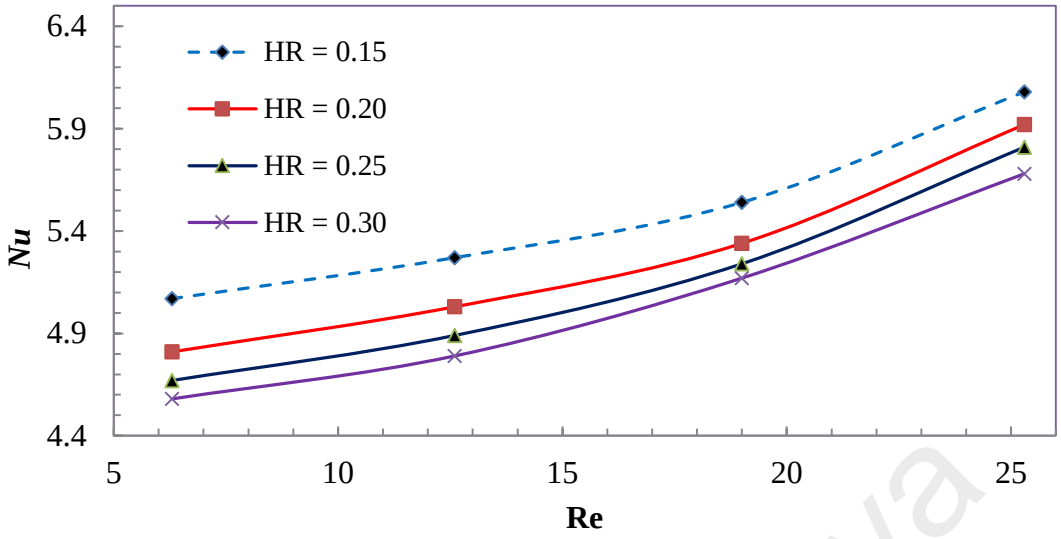

Figure 5.4: Variation of Nusselt number vs. Reynolds number for different helix radius (Constants; Pitch = 1mm, Turns = 7, α = 2).

Recall that the secondary flow is intensified based on the Dean number as shown in Figure 5.5. It can be seen from the figure that magnitude of the secondary flow is much larger for the channel with smaller helix radius. From the figure, it can be clearly seen that the magnitude of the core flow decreases as the helix radius increases (Figure 5.5a-d). Similar patterns are also observed by Mohammed and Narrein (2012) for other related heat transfer applications.

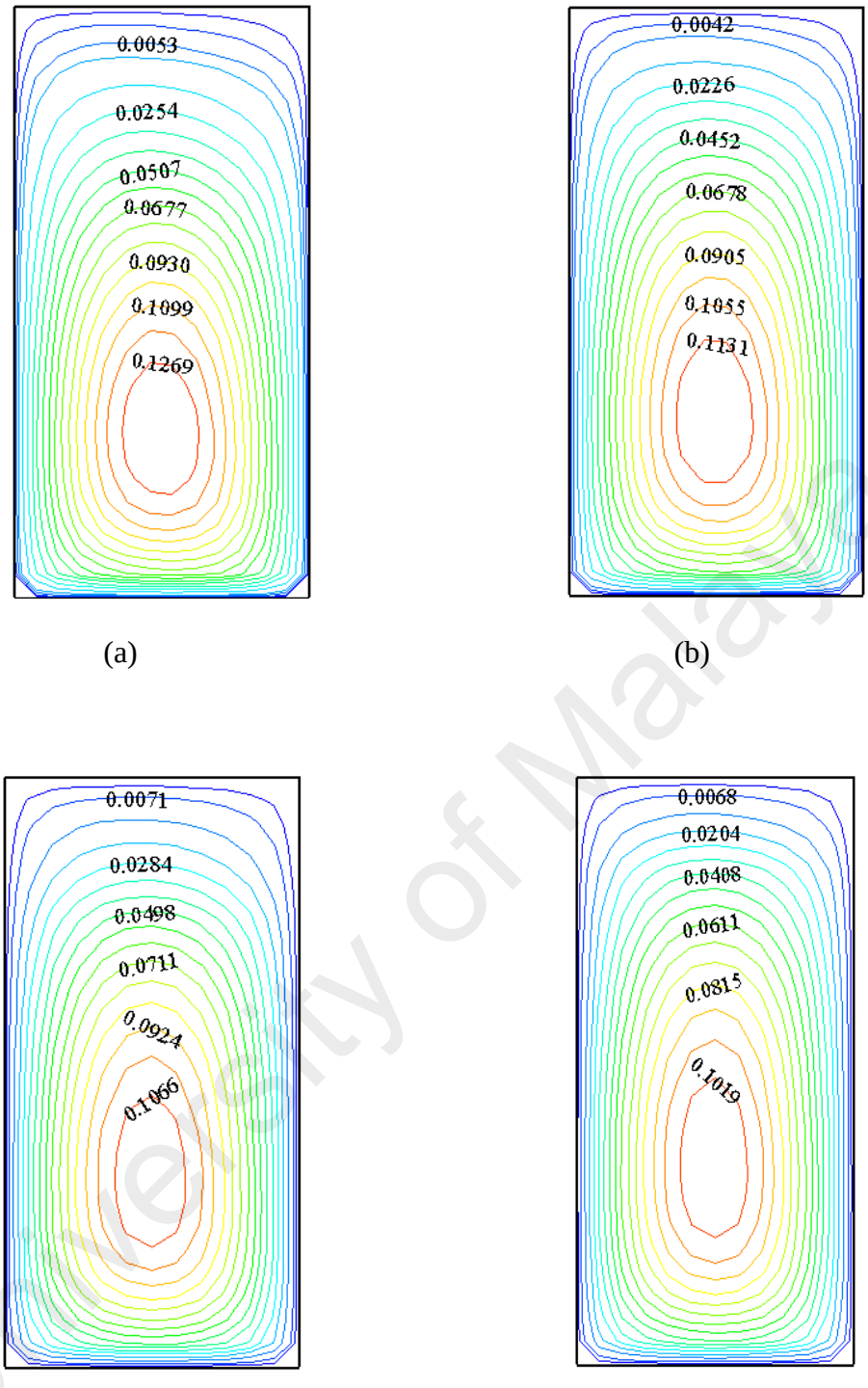

Figure 5.5: Velocity (m/s) contour (at mid-section) for HR = 0.15 mm, (b) HR = 0.20 mm, (c) HR = 0.25 mm. (d) HR = 0.30 mm at *Re* = 6 (Constants; Pitch = 1mm, Turns = 7, α = 2)

The pitch of a helical coil is the distance of one complete helix turn measured along the helix axis. Figure 5.6 shows that better heat transfer enhancement can be achieved at lower *Re* as the pitch value is increased. The pitch of the coil will lead to an additional torsion force which enhances heat transfer. The effect of pitch becomes less dominant at higher *Re*. At lower Reynolds number, the heat transfer is intensified as the secondary flow is skewed towards the outer wall of the HMCHS on increasing the pitch. However, this effect is reduced at higher Reynolds number as shown in Figure 5.7.

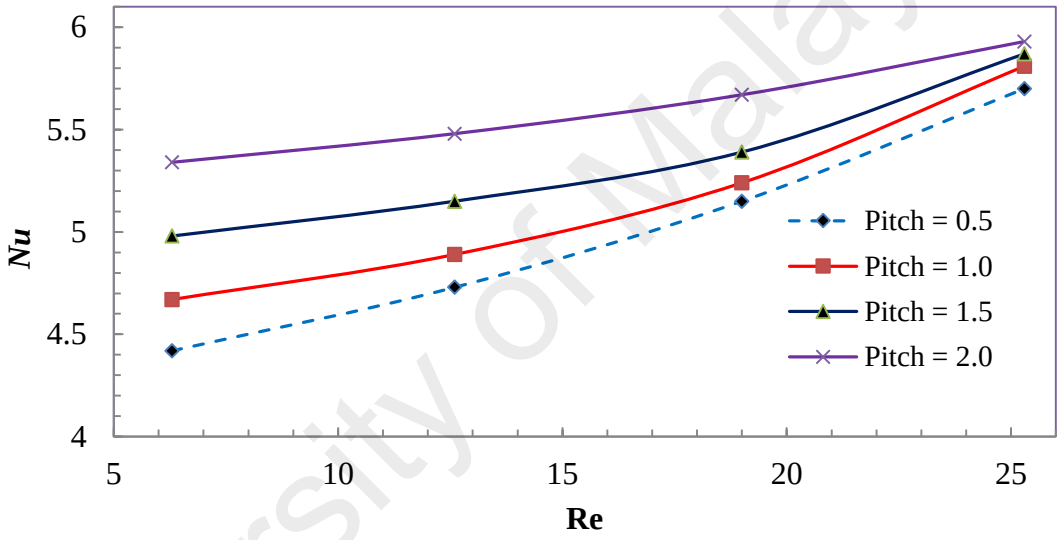

Figure 5.6: Variation of Nusselt number vs. Reynolds number rate for different pitch (Constants; HR = 0.25mm, Turns = 7, α = 2).

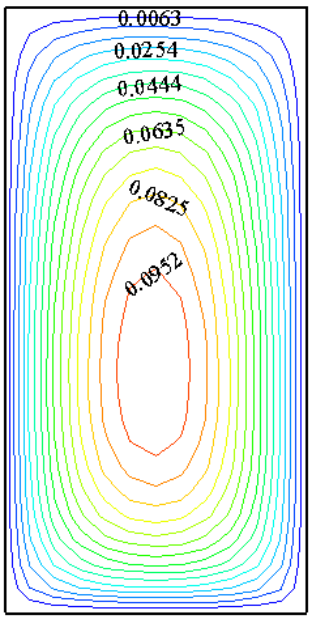

Pitch = 0.5

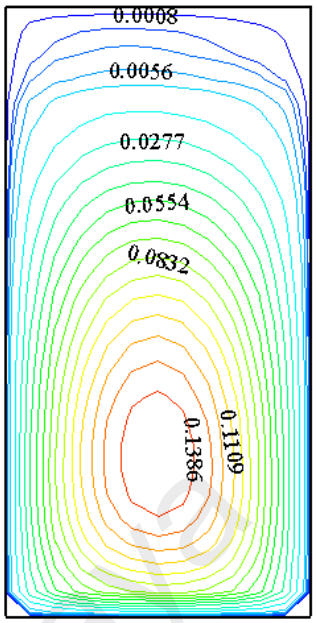

Pitch = 2.0

(a)

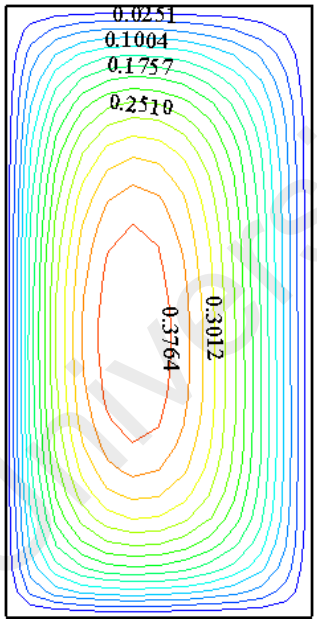

Pitch = 0.5

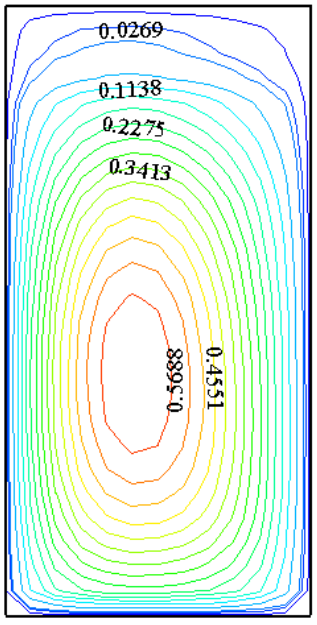

Pitch = 2.0

(b)

Figure 5.7: Velocity contour (at mid-section) for (a) *Re* = 6 and (b) *Re* = 25

The effect of the HMCHS length on the thermal field is presented in Figure 5.8. Increasing the number of turns does not affect the overall heat transfer performance since the thermal boundary layer becomes fully developed after a certain optimum length. Hence the overall heat transfer rate reaches a maximum value. Such effect was also observed in a work by Poh and Ng (1998).

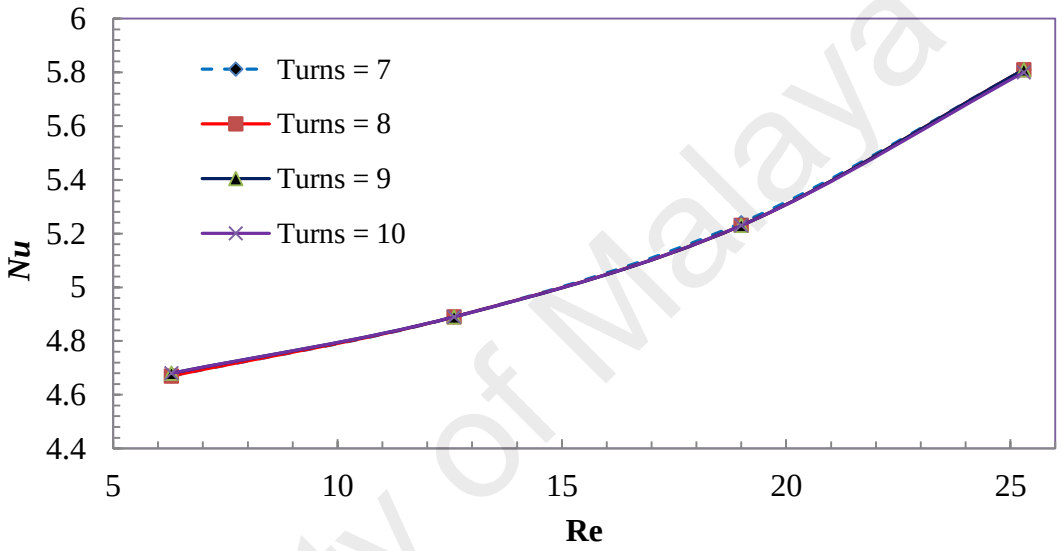

Figure 5.8: Variation of Nusselt number vs. Reynolds number for different number of turns (Constants; Pitch = 1mm, HR = 0.25mm, α = 2).

The aspect ratio is varied on increasing the channel height and keeping the channel width constant. The results for aspect ratio is presented in Figure 5.9. Previous literatures suggest that local heat transfer conductance vary around the edge of the channel and move towards zero at the square corners (Kays and Crawford, 1993). Svino and Siegel (1964) found that poor convection occurs due to lower velocities at the corners. The dominance of these effects on convective heat transfer fades off at higher aspect ratio which is also observed in this study where Nusselt number increases on increasing the aspect ratio. In addition, the overall heat transfer area increases on increasing the channel height and this leads to better thermal performance. The aspect ratio characteristics portrayed in Figure

5.8 and Figure 4.9 (previous chapter) is different because the x-axis value considered in both the cases are not similar.

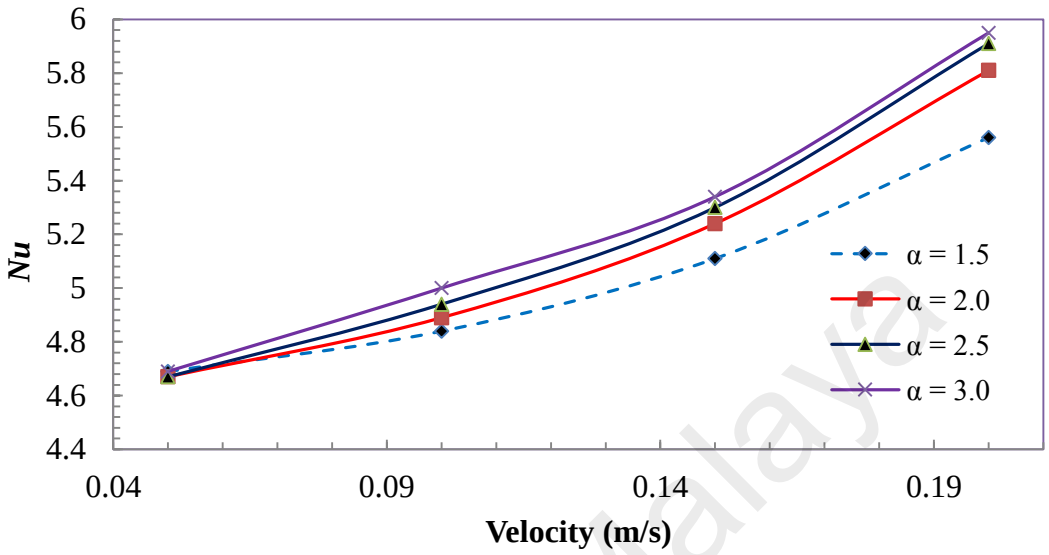

Figure 5.9: Variation of Nusselt number vs. velocity for different aspect ratios (Constants; Pitch = 1mm, Turns = 7, HR = 0.25mm).

5.2.1 The effects of geometrical parameters on flow field

The net pressure drop across the HMCHS is used as an assessment metric to analyze the flow field performance. The pressure drop is obtained based on the area-weighted average value pressure of the inlet and outlet. Figures 5.10 through 5.13 show the pressure drop analysis for different geometrical parameters considered in this study. It can be inferred that pressure drop increases on increasing the Reynolds number for all cases. The pressure drop for different values of helix radius is portrayed in Figure 5.10. The pressure drop generally increases with decreasing helix radius due to secondary flow intensification.

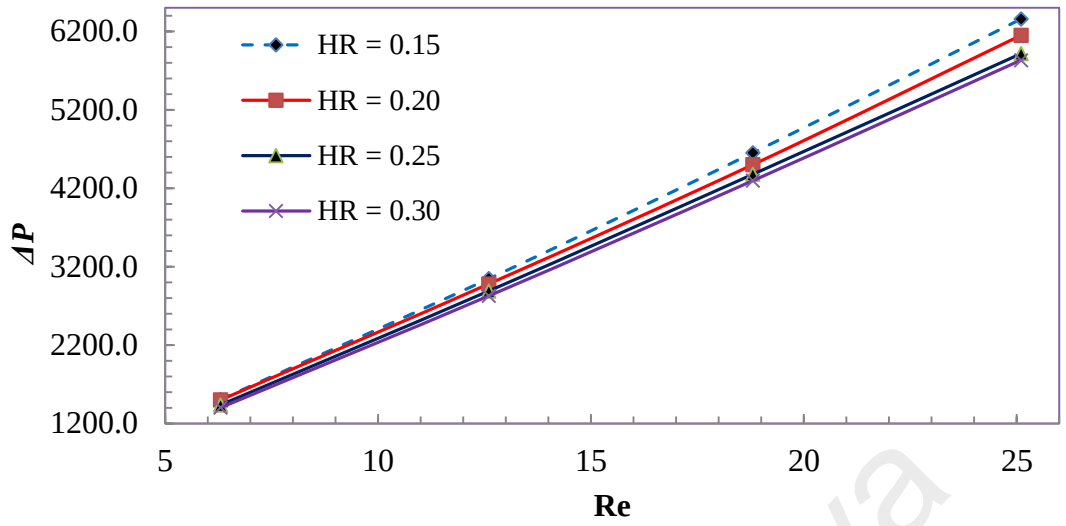

Figure 5.10: Pressure drop of different helix radius for various mass flow rates (Constants; Pitch = 1mm, Turns = 7, α = 2).

The pressure drop increases on increasing pitch as shown in Figure 5.11. As the pitch is increased, the flow speed increases due the reduced curvature. At higher velocities, the shear stress is increased which leads to a higher pressure drop.

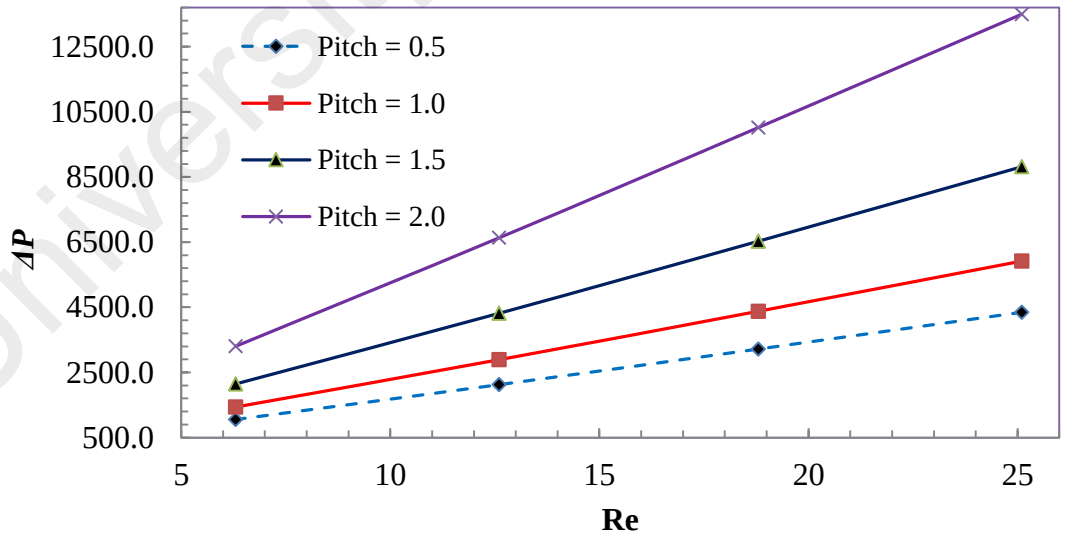

Figure 5.11: Pressure drop of different pitch length for various mass flow rates (Constants; HR = 0.25mm, Turns = 7, α = 2).

Increasing the number of turns also lead to additional pressure drop and this is due to the increase in overall length of the HMCHS as shown in Figure 5.12.

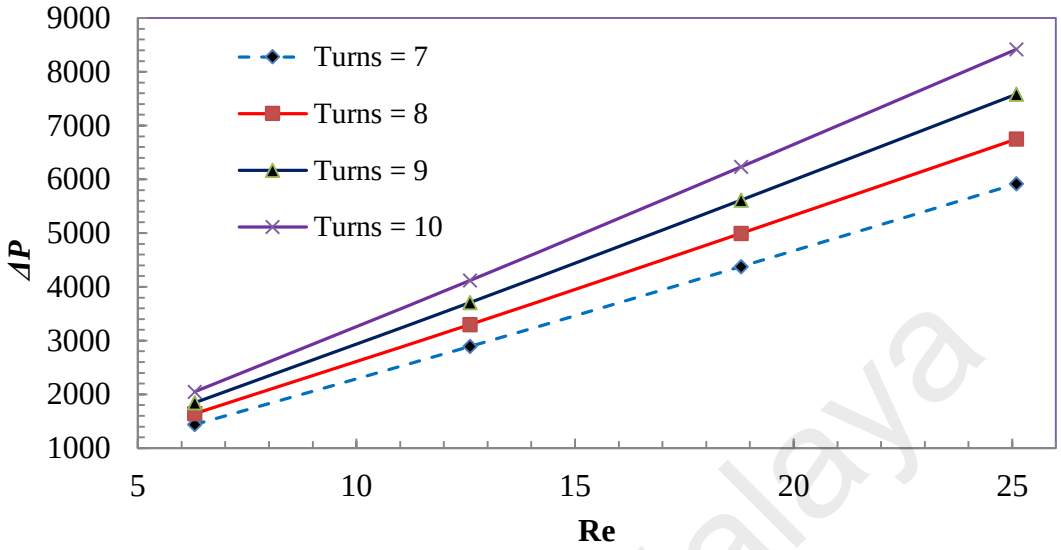

Figure 5.12: Pressure drop of different number of turns for various mass flow rates (Constants; Pitch = 1mm, HR = 0.25mm, α = 2).

It can be also observed that pressure drop increases on decreasing the aspect ratio as depicted in Figure 5.13. As the aspect ratio becomes smaller, a higher wall shear stress is induced which directly results in additional pressure drop.

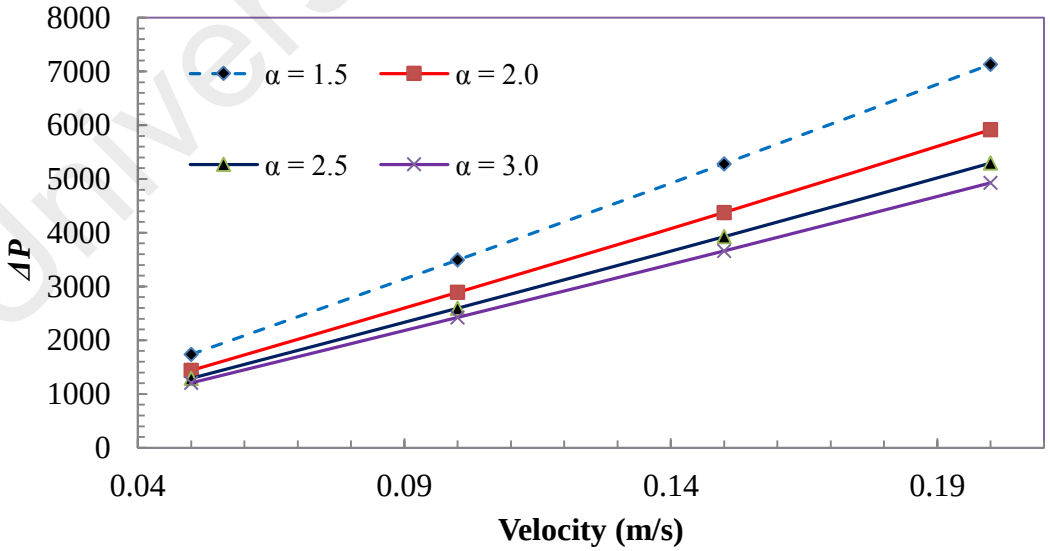

Figure 5.13: Pressure drop of aspect ratio for various mass flow rates (Constants; Pitch = 1mm, Turns = 7, HR = 0.25mm)

5.3 Conclusions

Convective heat transfer of nanofluid in a HMCHS is studied numerically using the two-phase mixture model approach with modified effective thermal conductivity and effective viscosity equation. The effects of helix radius, pitch, turns and aspect ratio on the temperature field is investigated.

- Helical shaped geometry is able to increase the convective heat transfer substantially and the thermal performance can be further increased by decreasing the helix radius.
- The Nusselt number increases on increasing the pitch due to additional torsion force but the effect is suppressed at higher Reynolds number.
- The number of turns (length of HMCHS) does not affect the thermal performance but more turns will lead to additional pressure drop.
- The thermal performance is better for channels with higher aspect ratio.

CHAPTER 6: TWO-PHASE LAMINAR PULSATING NANOFLUID FLOW IN HELICAL MICROCHANNEL

This chapter discusses the numerical investigations on the thermal and hydraulic characteristics of pulsating laminar flow in a three-dimensional helical microchannel heat sink (HMCHS) using Al_2O_3-water based nanofluid. The two-phase mixture model with modified effective thermal conductivity and viscosity equations is employed for solving the problem numerically. The detailed results for thermal and flow fields are reported for the effects of amplitude, frequency and nanoparticle concentration.

6.1 Mathematical Modeling

6.1.1 Governing equations

The helical microchannel heat sink considered in this study is shown schematically in Figure 6.1. The heat is transferred from the outer wall of the HMCHS to the nanofluid which flows through the channel. Several assumptions are made on the operating conditions of the HMCHS as follows: (i) the MCHS operates under steady-state conditions; (ii) the properties of the HMCHS material are temperature independent; (iii) the external heat transfer effects are ignored.

The governing equations for mass, momentum and energy for two-phase mixture model are:

Continuity equation:

$$\nabla.(\rho_m \vec{v}_m) = 0 \tag{6.1}$$

where

$$\rho_m = \sum_{k=1}^{n} \emptyset_k \rho_k \tag{6.2}$$

Momentum equation:

$$\nabla.(\rho_m \vec{v}_m \vec{v}_m) = \nabla\rho_m + \nabla.[\mu_m(\nabla\vec{v}_m + \vec{v}_m^T)] + \rho_m\vec{g} + \nabla.(\sum_{k=1}^{n} \emptyset_k \rho_k \vec{v}_{dr,k}\vec{v}_{dr,k}) \quad (6.3)$$

where n is the number of phases, $\emptyset$ is the volume fraction and μ_m is the viscosity of the mixture:

$$\mu_m = \sum_{k=1}^{n} \emptyset_k \mu_k \quad (6.4)$$

$\vec{v}_{dr,k}$ is the drift velocity for secondary phase *k* defined as:

$$\vec{v}_{dr,k} = \vec{v}_k - \vec{v}_m \quad (6.5)$$

Energy equation:

$$\nabla.(\sum_{k=1}^{n} \emptyset_k \vec{v}_k(\rho_k h_k + p)) = \nabla.(\lambda_{eff}\nabla T) \quad (6.6)$$

The representative viscosity for the nanoparticle is estimated as:

$$\mu_{np} = \frac{\frac{\mu_m}{\emptyset_{bf}\mu_{bf}}}{\emptyset_{np}} \quad (6.7)$$

where μ_m is given by (Corcione, 2012):

$$\frac{\mu_m}{\mu_{bf}} = \frac{1}{1-34.87\left(\frac{d_{np}}{d_{bf}}\right)^{-0.3}\emptyset^{1.03}} \quad (6.8)$$

Equivalent diameter of base fluid molecule (Corcione, 2012):

$$d_{bf} = \left[\frac{6M}{N\pi\rho_{bf}}\right] \quad (6.9)$$

The effective thermal conductivities for liquid and particle phases are estimated as (Kuipers et. al, 1992):

$$\lambda_{eff,bf} = \frac{\lambda_{bf}}{\emptyset_{bf}} \quad (6.10)$$

$$\lambda_{eff,np} = \frac{\lambda_{np}}{\emptyset_{np}} \quad (6.11)$$

where

$$\lambda_{bf} = (1 - \sqrt{(1 - \emptyset_{bf}}) \lambda_{bf} \, , \tag{6.12}$$

$$\lambda_{np} = 1 - \sqrt{(1 - \emptyset_{bf}}) (\omega A + [1 - \omega] \Gamma) \lambda_{bf} \, , \tag{6.13}$$

and

$$\Gamma = \frac{2}{1 - \frac{B}{A}} \left\{ \frac{B(A-1)}{A\left(1 - \frac{B}{A}\right)^2} \ln\left(\frac{A}{B}\right) - \frac{(B-1)}{(1 - \frac{B}{A})} - \frac{B+1}{2} \right\} \tag{6.14}$$

with

$$B = 1.25 \left(\frac{[1 - \emptyset_{bf}]}{\emptyset_{bf}} \right)^{10/9} \tag{6.15}$$

For spherical particles

$$A = \frac{\lambda_{np}}{\lambda_{bf}} \text{ and } \omega = 7.26 \, x \, 10^{-3} \tag{6.16}$$

The inlet velocity profile is given by:

$$V = V_o + a.sin(ft) \tag{6.17}$$

Figure 6.1: Schematic diagram of the computational domain of HMCHS

6.1.2 Boundary conditions

The inlet section is specified as transient velocity inlet and the pressure outlet boundary condition is applied to the outlet region. No-slip boundary conditions are applied on the internal solid walls for velocity (*u, v* and *z*). The iso-flux boundary condition is applied on the external walls. The governing equations along with the specified boundary conditions are solved to obtain the fluid temperature distribution and pressure drop along the HMCHS. These are then used to examine the thermal and flow field along the HMCHS.

The range of the inlet Reynolds number considered in this study is 6 to 25. The accuracy of results might be affected at high Reynolds number due to entrance, exit and surface roughness effects. The Al_2O_3-water based nanofluid of 42nm average diameter is used as a working fluid. The inlet temperature of the water is taken as 300K and constant heat flux of 5×10^4 W/m^2 is applied on the external walls. Individual parameters are investigated by making all other parameters constant as shown in Table 6.1.

Table 6.1: Details of case setup.

Case	Varying Parameter	Fixed Parameters	Geometrical Parameters
Amplitude (m/s)	1 2 3	Frequency, 10 rad/s Concentration, 1%	HR = 0.25mm Pitch = 1mm Turns = 7 Aspect Ratio = 2
Frequency (rad/s)	5 10 20	Amplitude, 3 m/s Concentration, 1%	
Concentration (%)	1 2 3	Amplitude, 1 m/s Frequency, 10 rad/s	

6.1.3 Numerical Method

The numerical computations are carried out by solving the governing equations along with boundary conditions using the finite volume method. The SIMPLE algorithm is adopted to couple the velocity and pressure field. The second-order upwind differencing scheme is used for the convective terms. The original two-phase mixture model equation over predicts the thermal conductivity and a viscosity value is required for the solid phase as per Eq. 6.4. Hence, Eq. 6.7-6.16 is used to redefine the effective thermal conductivity and viscosity. Numerical simulation is carried out for different combinations of amplitude, frequency and nanoparticle concentration. The velocity of the fluid V, fluctuates about an equilibrium value, V_O, based on the specified amplitude and frequency (Figure 6.2).

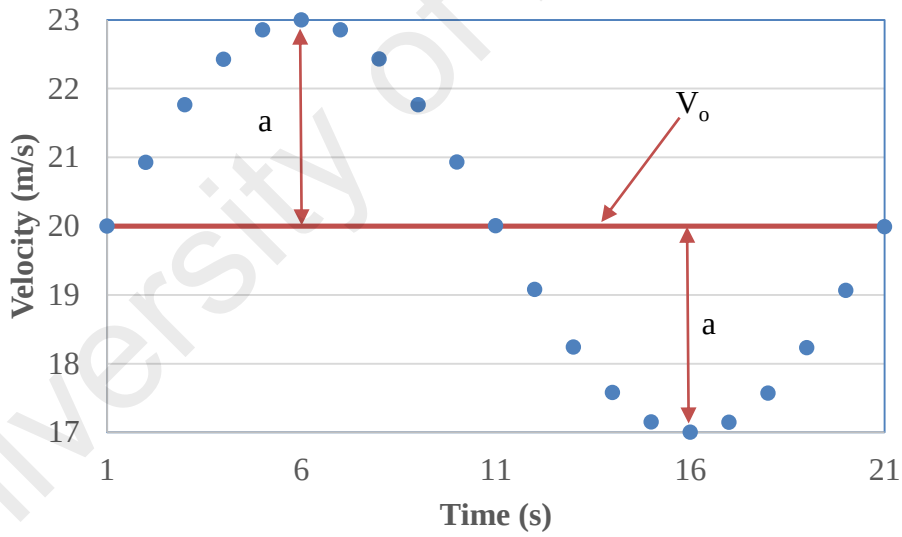

Figure 6.2: Sample velocity profile at inlet (a = 3 m/s)

The sample user defined function for the fluctuating velocity component is shown below:

```
/************************************************************************
unsteady.c
UDF for specifying a transient velocity profile boundary condition
************************************************************************/
#include "udf.h"
DEFINE_PROFILE(unsteady_velocity, thread, position)
{
face_t f;
real t = CURRENT_TIME;
begin_f_loop(f, thread)
{
F_PROFILE(f, thread, position) = 20. + 5.0*sin(10.*t);
}
end_f_loop(f, thread)
}
```

A full period of oscillation is considered in the inlet velocity and the maximum number of iterations per time step is set to 1500. This value is chosen based upon the fact that 800-1000 iterations are needed per time step for the flow and thermal field to reach steady state. . The convergence criterion required that the maximum relative residual for mass, momentum and energy to be smaller than 1×10^{-6}. Second order discretization scheme is used for volume fraction, pressure, momentum and energy equations. The under-relaxation factor parameters for pressure, momentum, slip velocity and volume fraction is set to 0.3, 0.7, 0.1 and 0.2 respectively.

6.2 Results and Discussion

Figure 6.3 illustrates the comparison of time averaged Nusselt number between steady and pulsating flow conditions. The local convective heat transfer coefficient and Nusselt number is calculated using the following equation:

$$h(x) = \frac{q}{(T_{Wall}(x) - T_{Fluid}(x))} \tag{6.18}$$

$$Nu(x) = \frac{h(x)D_h}{\lambda} \tag{6.19}$$

where q represents heat flux, h is the heat transfer coefficient, D_h is the hydraulic diameter and λ is the thermal conductivity of the working fluid. The average Nusselt number can be obtained by:

$$Nu = \frac{1}{L}\int_0^L Nu\,(x).dx \tag{6.20}$$

where L represents the channel length.

An average of 30% increase in Nusselt number is observed for the case of pulsating flow. The heat transfer enhancement is due to the additional mixing between the core and near-wall fluid region as a result of the unsteady inlet flow (Nandi and Chattopadhyay, 2014).

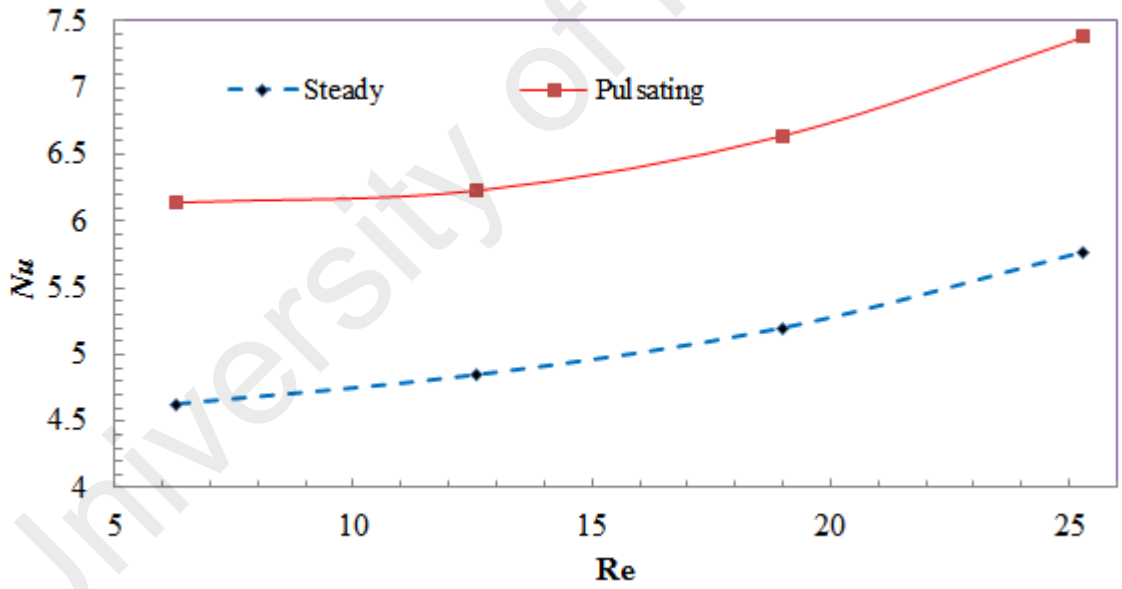

Figure 6.3: Comparison between steady and pulsating flow (a = 1, f = 10 rad/s, and Ø = 1%)

Increasing the amplitude lead to further enhancement as shown in Figure 6.4. However, the effects of different amplitude become less significant at higher Reynolds number due to the dominant effect of the secondary flow as a result of the helix curvature which suppresses the mixing effect caused by the inlet pulsating flow condition.

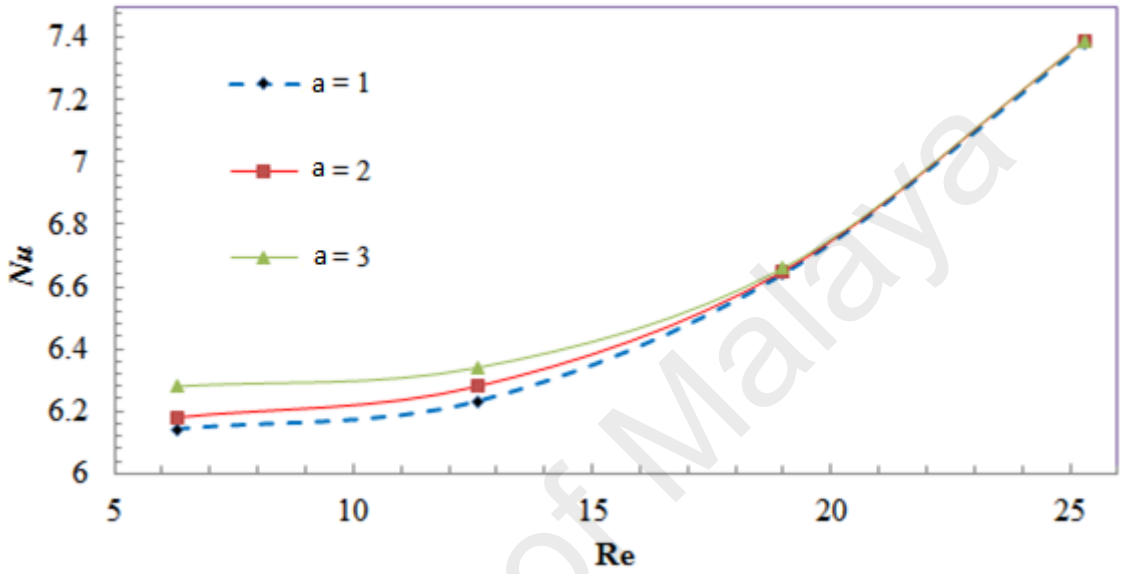

Figure 6.4: Variation of Nusselt number vs. Reynolds number for different amplitudes (Constants; HR = 0.25mm, Pitch = 1mm, Turns = 7, α = 2).

The effect of frequency on the heat transfer characteristics is shown in Figure 6.5. The Nusselt number increases on increasing the frequency and Reynolds number and the additional enhancement can be attributed to the supplementary mixing effect which is proportional to the magnitude of frequency.

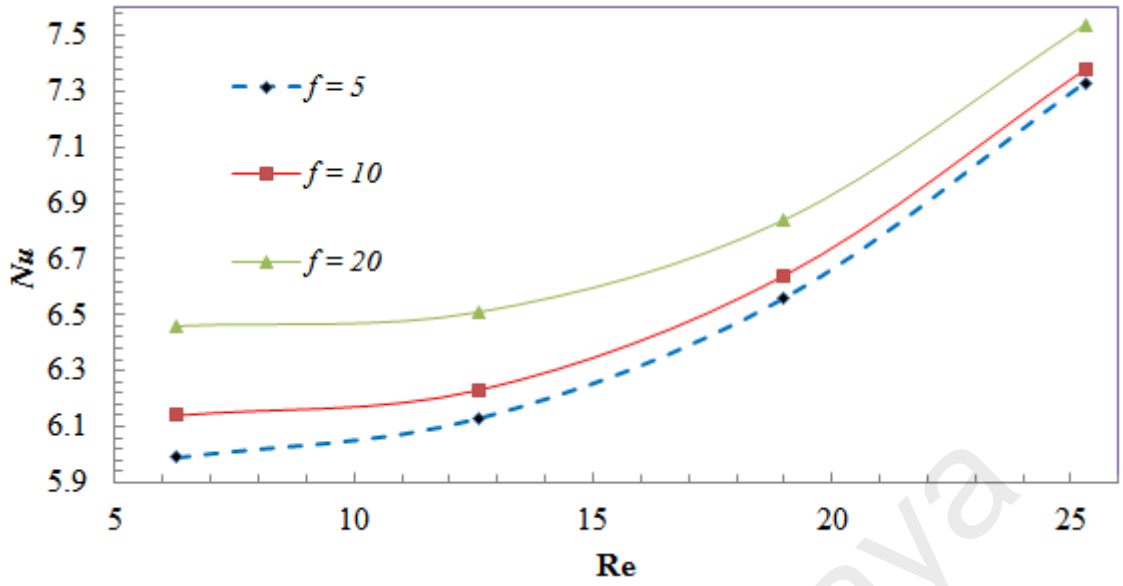

Figure 6.5: Variation of Nusselt number vs. Reynolds number for different frequencies (Constants; HR = 0.25mm, Pitch = 1mm, Turns = 7, α = 2).

The significance of nanoparticle volume fraction on the heat transfer coefficient is shown in Figure 6.6 Improvement in heat transfer coefficient is observed on increasing the nanoparticle volume fraction but the Nusselt number (not presented here) tends to decrease as a result of increasing thermal conductivity. Since the thermal conductivities of solid materials (metals) are higher than those of liquids, thermal conductivities of particle-fluid mixtures are expected to increase (Yu et al., 2008).

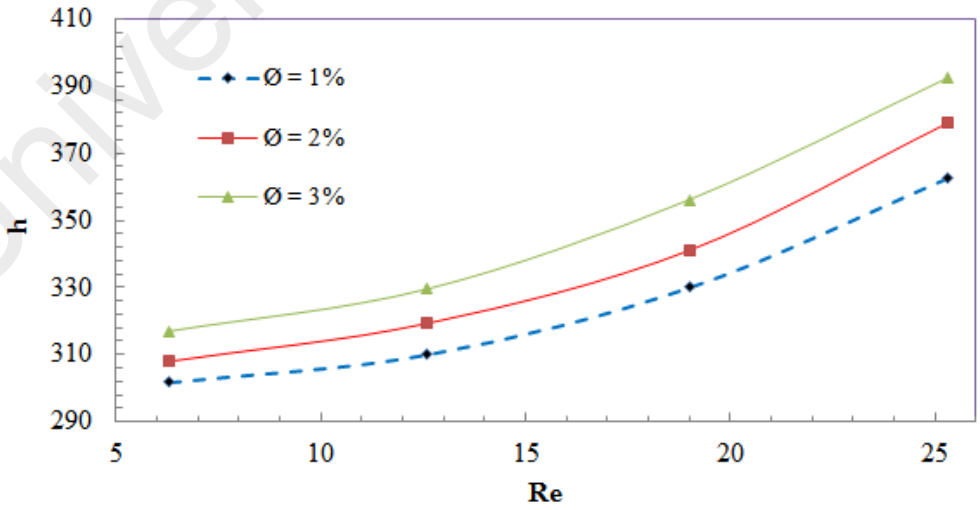

Figure 6.6: Variation of heat transfer coefficient vs. Reynolds number for different nanoparticle volume concentrations (Constants; HR = 0.25mm, Pitch = 1mm, Turns = 7, α = 2)..

The pressure drop for different amplitude and Reynolds number is presented in Figure 6.7. The pressure drop is marginally lower for the case of low amplitude compared to steady condition. This is because the pulsating flow creates more interaction between the near wall fluid and core fluid which makes the flow fully developed with shorter entrance region. Developed flow has a lower velocity at the near wall region which in turn has a small pressure drop. Hence, it can be observed that significant thermal enhancement can be achieved through pulsating flow with a reduction in pressure drop. The same result was observed by Luciu et al. (2009).

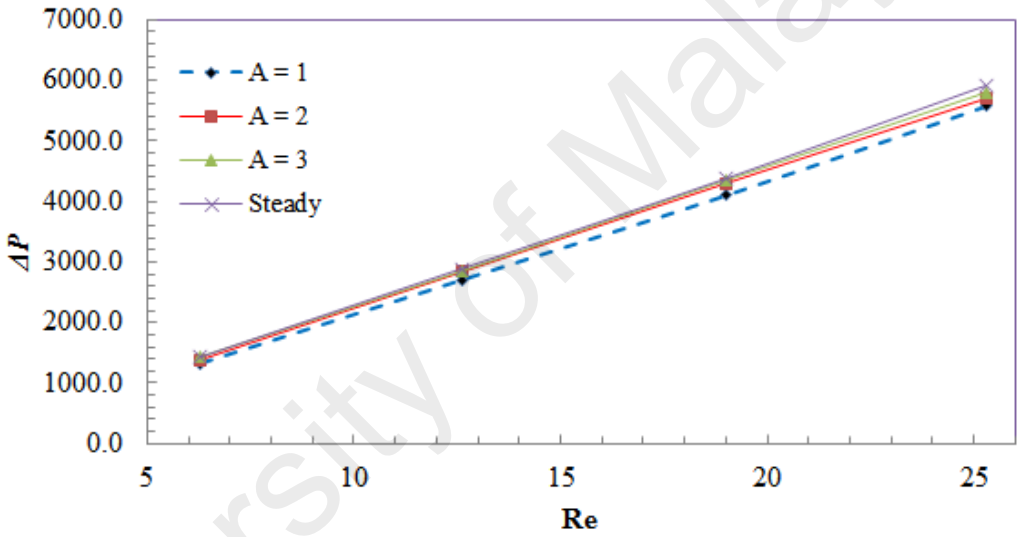

Figure 6.7: Variation of pressure drop vs. Reynolds number for different amplitudes (Constants; HR = 0.25mm, Pitch = 1mm, Turns = 7, $\alpha = 2$).

6.3 Conclusions

A numerical study of pulsating flow in a HMCHS is studied using the two-phase mixture model approach with modified thermal conductivity and viscosity equation. The effects of amplitude, frequency and nanoparticle volume concentration on the temperature and flow field are investigated.

- Pulsating inlet flow condition is able to increase the convective heat transfer substantially with marginal reduction in pressure drop compared to steady condition.
- The Nusselt number increases on increasing the amplitude due to additional mixing but the effect is suppressed at higher Reynolds number.
- The thermal performance increases on increasing the frequency.
- The heat transfer coefficient increases on increasing the nanoparticle volume concentration but the Nusselt number performance deteriorate as a result of increasing thermal conductivity.

CHAPTER 7: CONVECTIVE FLOW AND HEAT TRANSFER IN A HELICAL MICROCHANNEL FILLED WITH POROUS MEDIUM

This chapter discusses the numerical investigations on forced convection in a helical microchannel heat sink (HMCHS) filled with porous medium. The effects of helix radius, pitch, number of turns and aspect ratio on heat transfer and fluid flow characteristics are comprehensively investigated. The governing equations for flow and heat transfer are solved using the finite volume method.

7.1 Mathematical Modeling

7.1.1 Governing equations

The helical microchannel heat sink considered in this study is shown schematically in Figure 7.1. Heat is transferred from the outer wall of the HMCHS to the inner working fluid. Several assumptions were made on the operating conditions of the HMCHS: (i) the HMCHS operates under steady-state conditions; (ii) the fluid is laminar incompressible and remains in single phase along the channel; (iii) the properties of the fluid and HMCHS material are temperature independent; (iv) the external heat transfer effects are ignored; (v) the porous medium is assumed to be isotropic, homogenous and internally equilibrium with the fluid; (vi) the Darcy's Law is adapted for porous medium because of the suitability with laminar flow assumption.

The governing equations for flow and heat transfer in the HMCHS are:

Continuity

$$\nabla \circ \vec{v} = 0 \tag{7.1}$$

Momentum

$$(\vec{v} \circ \nabla)\vec{v} = \frac{1}{\rho}\nabla p + \nu\Delta\vec{v} + \frac{\nu}{K_p}\vec{v} \tag{7.2}$$

Energy

$$(\vec{v} \circ \nabla)T = \frac{k}{\rho c_p}\Delta T \tag{7.3}$$

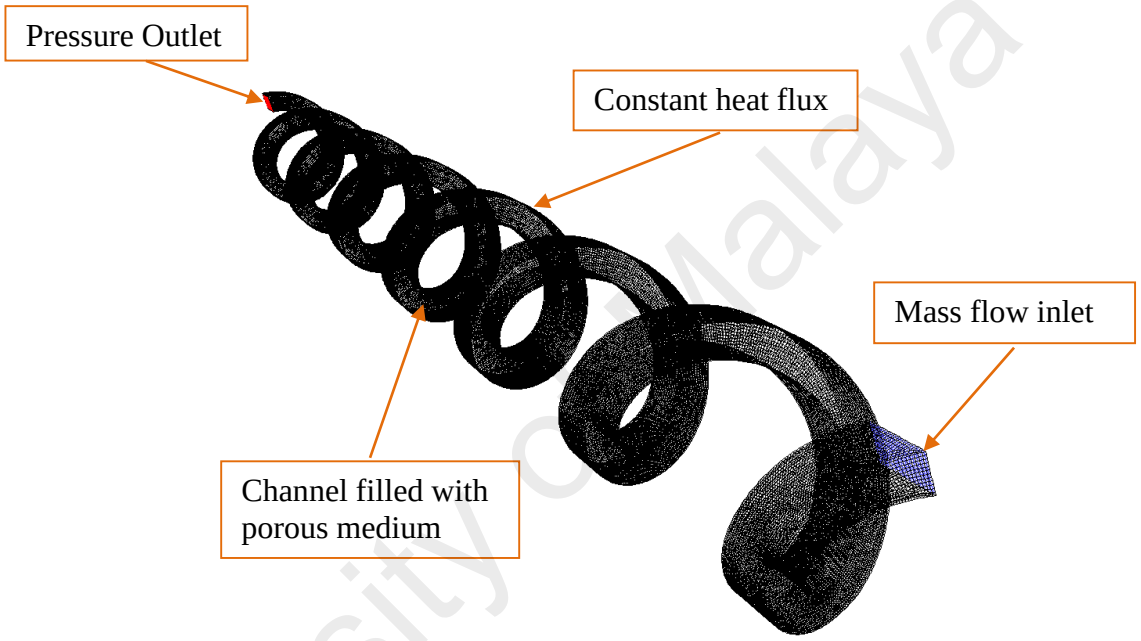

Figure 7.1: Schematic diagram of the computational domain of HMCHS filled with porous medium

7.1.2 Boundary conditions

The iso-flux boundary condition is applied on all four walls of the physical system. No-slip boundary conditions for velocity (*u*, *v* and *z*) are applied on the solid walls. The inlet region is specified as mass flow rate boundary condition while the pressure outlet boundary condition is applied to the MCHS outlet region. The governing equations along with the boundary conditions are solved to obtain the fluid temperature distribution and pressure drop in the HMCHS. These data are then used to examine the thermal and flow fields along the HMCHS.

With water as working fluid, four different values of inlet mass flow rates used in the investigations are 0.00008, 0.00012, 0.00016 and 0.00020 kg/s. The inlet temperature of the water is taken as 300K. Constant heat flux of 1×10^6 W/m^2 is applied to the outer walls. The porous medium is comprised of copper with 40% porosity, 1.44×10^{-11} m^2 of permeability, thermal conductivity of 387.6 W/m.K and 6.94×10^{10} 1/m^2 viscous resistance as listed in Table 7.1. The local fluid and porous medium are assumed to be in thermodynamic equilibrium. The porous medium is isotropic and homogenous. The details of the case setup is given in Table 7.2.

Table 7.1: Properties of porous medium (Copper)

Physical property	Value
Porosity, ε	40%
Permeability, K_p	1.44×10^{-11} m^2
Density, ρ	8978
Specific heat capacity, C_p	381
Thermal conductivity, k	387.6

Table 7.2: Details of case setup.

Case	Values	Fixed Parameter
Helix Radius	0.15 0.20 0.25 0.30	Pitch, 1mm Turns, 7 Aspect Ratio, 2
Pitch	0.5 1.0 1.5 2.0	Helix Radius, 0.25mm Turns, 7 Aspect Ratio, 2
Turns	7 8 9 10	Helix Radius, 0.25mm Pitch, 1mm Aspect Ratio, 2
Aspect Ratio	1.5 2.0 2.5 3.0	Helix Radius, 0.25mm Pitch, 1mm Turns, 7

7.1.3 Numerical Method

The numerical computations are carried out by solving the governing equations along with the boundary conditions using the finite volume method. The SIMPLE algorithm is adopted to investigate the flow field. The second-order upwind differencing scheme is used for the convective terms. The diffusion term in the momentum and energy equations are approximated by the second-order central difference scheme which gives a stable solution. At the end of each iteration, the residual sum for each of the conserved variables is computed and stored. The convergence criterion required that the maximum relative residual for mass, momentum and energy to be smaller than 1×10^{-6}. Second order discretization scheme is used for pressure, momentum and energy equations. The under-relaxation factor parameters for pressure and momentum is set to 0.3 and 0.7 respectively. Numerical simulation is carried out for different combinations of pertinent parameters such as (i) helix radius, (ii) pitch, (iii) turns and (iv) aspect ratio to investigate the effects on HMCHS.

7.1.4 Porous Medium Analysis Model Validation

The model validation results for porous medium problem are compared in terms of effective thermal conductivity based on the correlation suggested by Dunn and Reay (1994).

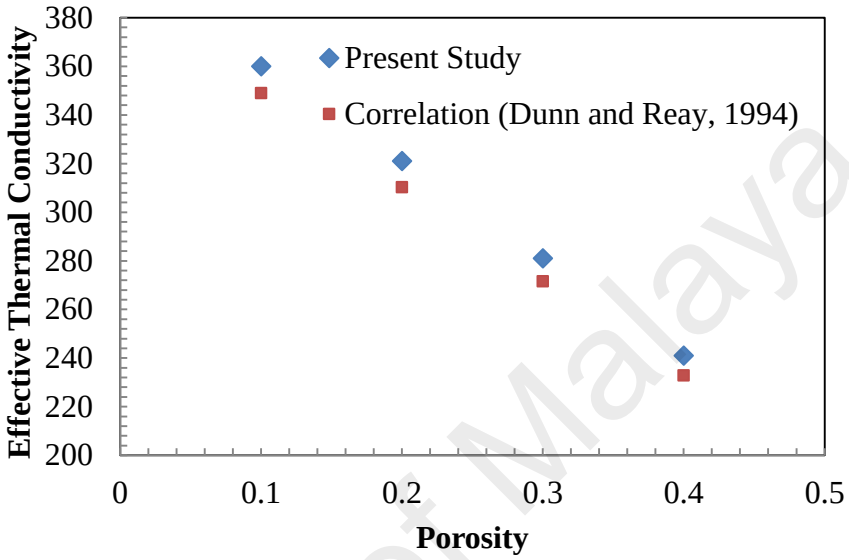

Figure 7.2: Model validation for porous medium

It can be seen from Figure 7.2 that the thermal field results are in good agreement with a maximum error of less than 3.5%. This error may be attributed to the CFD package code which uses superficial velocity formulation that does not consider porosity when calculating the convection and diffusion terms of the transport equations.

The model is further validated with the results presented by Hung et al. (2013). The rectangular microchannel's height and width is 0.009 m and 0.01 m respectively with a total number of 67 channels. The aspect ratio of the channel is 0.65. The inlet temperature is set to 295 K with a heat flux of 1×10^6 W/m^2 for a range of Reynolds number. Sintered coppered was considered as the porous substrate. It can be seen from Figure 7.3 that the Nusselt number results are in excellent agreement with previous literature.

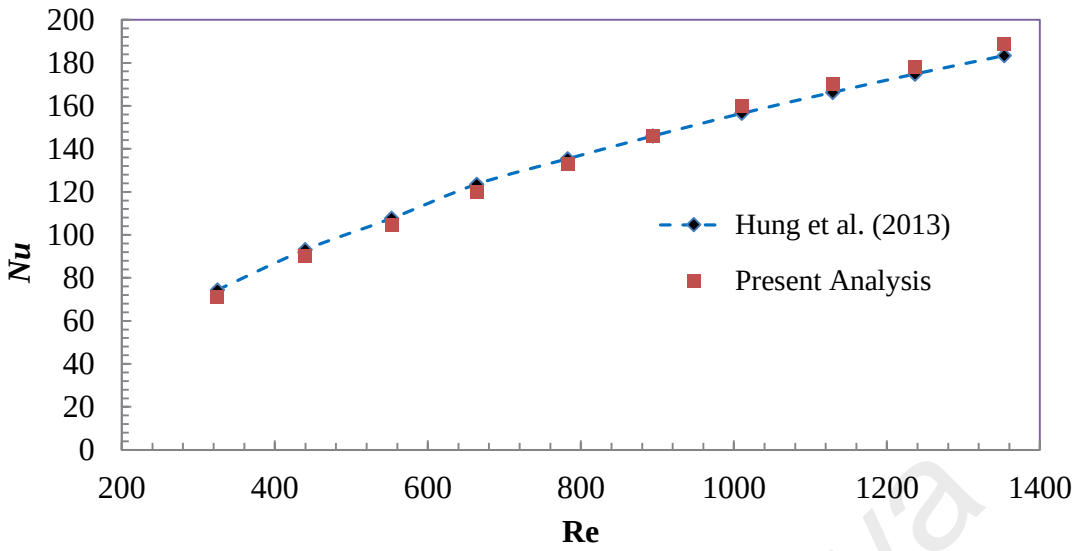

Figure 7.3: Nusselt number model validation for rectangular microchannel filled with porous medium.

7.2 Results and Discussion

7.2.1 The effects of geometry on the thermal field

The effects of different geometry on the thermal fields are presented by means of the Nusselt number as depicted in Figure 7.4. The local convective heat transfer coefficient and Nusselt number is calculated using the following equation:

$$h(x) = \frac{q}{(T_{Wall}(x) - T_{Fluid}(x))} \tag{7.4}$$

$$Nu(x) = \frac{h(x)D_h}{\lambda} \tag{7.5}$$

where q represents heat flux, h is the heat transfer coefficient, D_h is the hydraulic diameter and λ is the thermal conductivity of the working fluid. The average Nusselt number can be obtained by:

$$Nu = \frac{1}{L}\int_0^L Nu\,(x).dx \tag{7.6}$$

where L represents the channel length.

The Nusselt number increases on decreasing helix radius. As the helix radius is decreased, the secondary flow is intensified based on the Dean number.

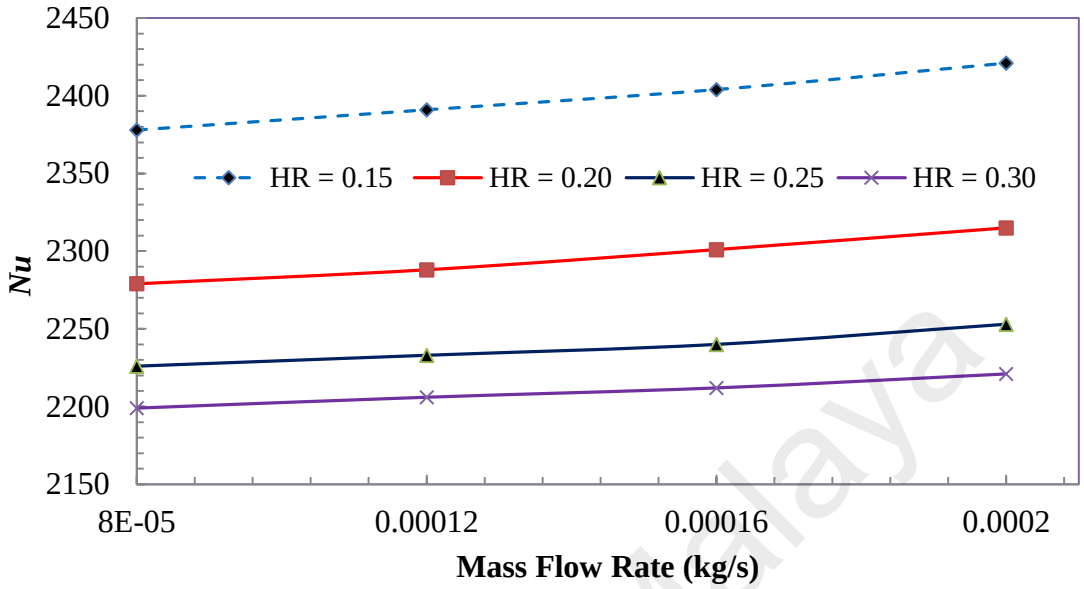

Figure 7.4: Variation of Nusselt number vs. mass flow rate for different helix radius (Constants; Pitch = 1mm, Turns = 7, α = 2).

Passive enhancement due to secondary flow intensification is validated via the velocity contour as shown in Figure 7.5. The figure implies that the magnitude of the secondary flow is much higher for the channel with smaller helix radius. The Nusselt number also increases on increasing the mass flow rate for all cases. Similar results are also observed by Mohammed and Narrein (2012) for macro-scaled tubes.

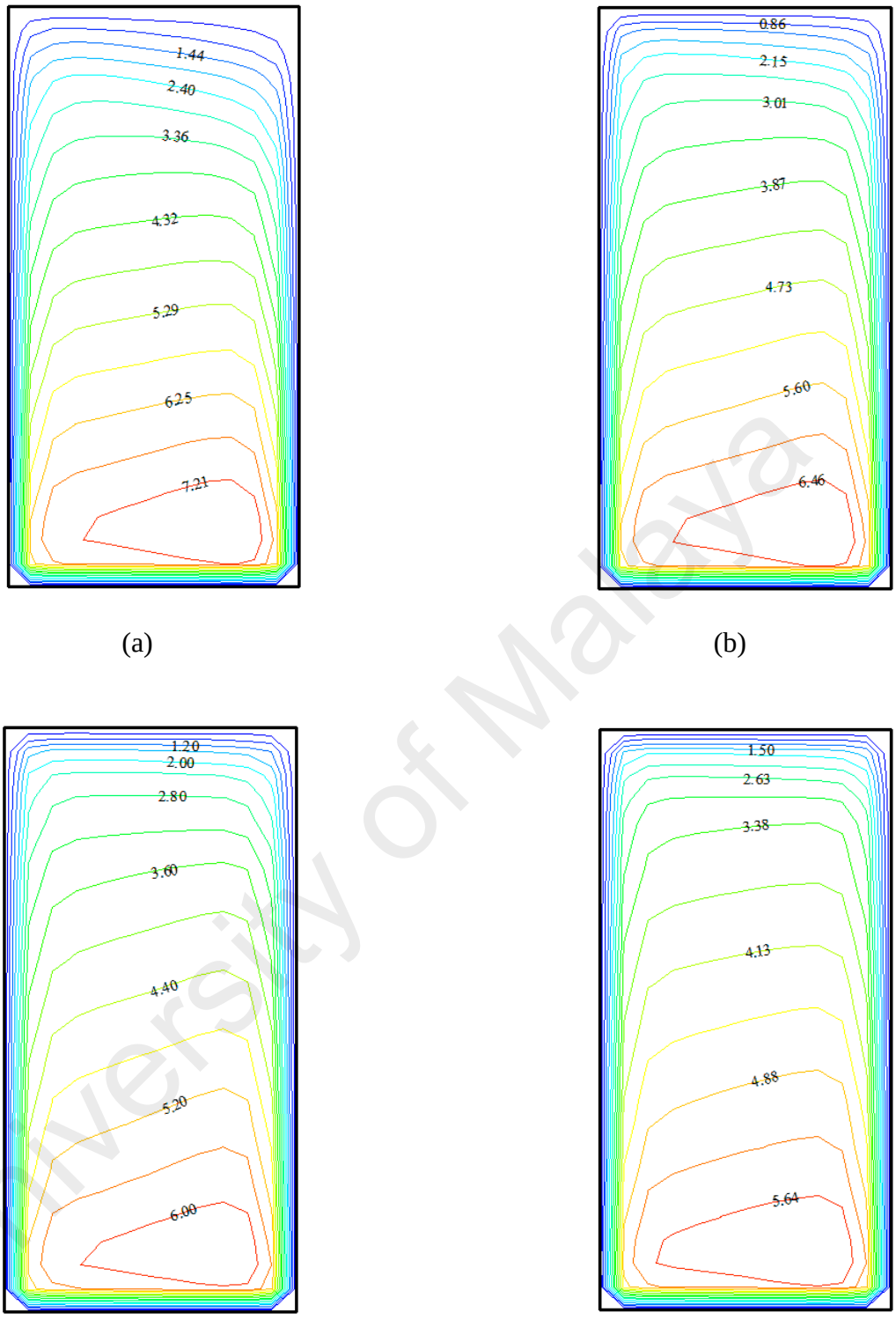

Figure 7.5: Velocity (m/s) contour (mid-section) for (a) HR = 0.15 mm, (b) HR = 0.20 mm, (c) HR = 0.25 mm. (d) HR = 0.30 mm at $\dot{m} = 0.00008\ kg/s$ (Constants; Pitch = 1mm, Turns = 7, α = 2).

Table 7.3 portrays the Nusselt number and pressure drop comparison between a straight microchannel and a HMCHS with and without porous medium of similar hydraulic diameter, length and the heat flux. Pronounced enhancement in Nusselt number is achieved in the HMCHS with porous medium compared to the non-porous straight and helical microchannel. The tremendous increase in pressure drop can be attributed to the additional flow resistance caused by the porous substrate.

Table 7.3: Comparison of Nusselt number and pressure drop

Geometry and Condition	Nusselt number	Pressure Drop (kPa)
Straight MCHS	7.04	79 730
HMCHS	22.06	280 084
HMCHS with porous medium	2279	4 361 834

The effect of pitch variation on the thermal field is shown in Figure 7.6. The pitch of the coil will lead to an additional torsion force which enhances heat transfer. Increase in pitch leads to an increase in Nusselt number. The results for number of turns are portrayed in Figure 7.7. No significant change in Nusselt number is observed as the number of turns is varied.

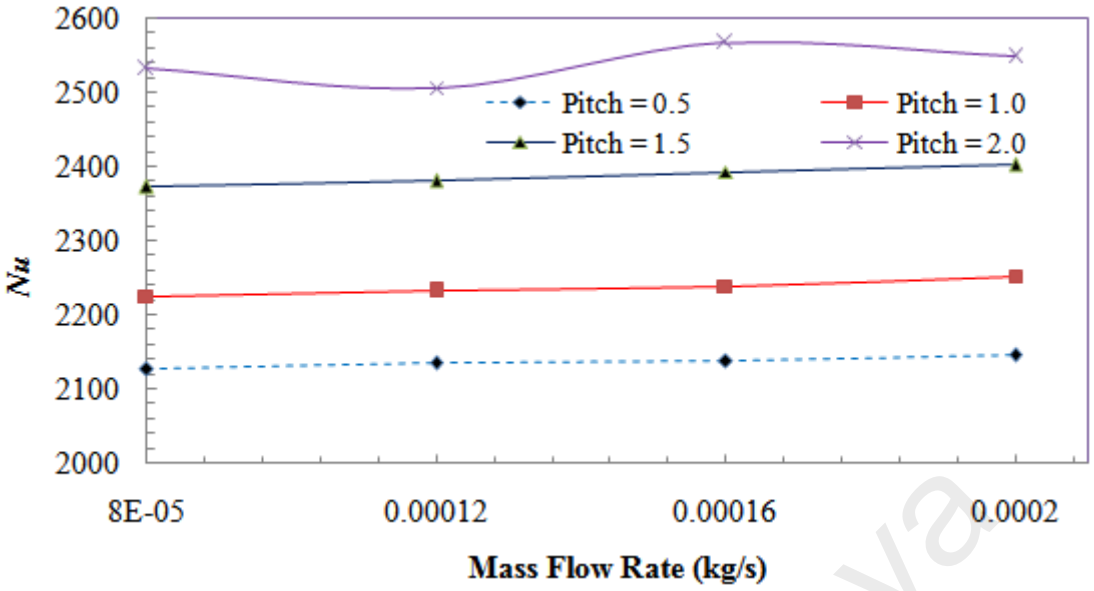

Figure 7.6: Variation of Nusselt number vs. mass flow rate for different pitch (Constants; HR = 0.25mm, Turns = 7, α = 2).

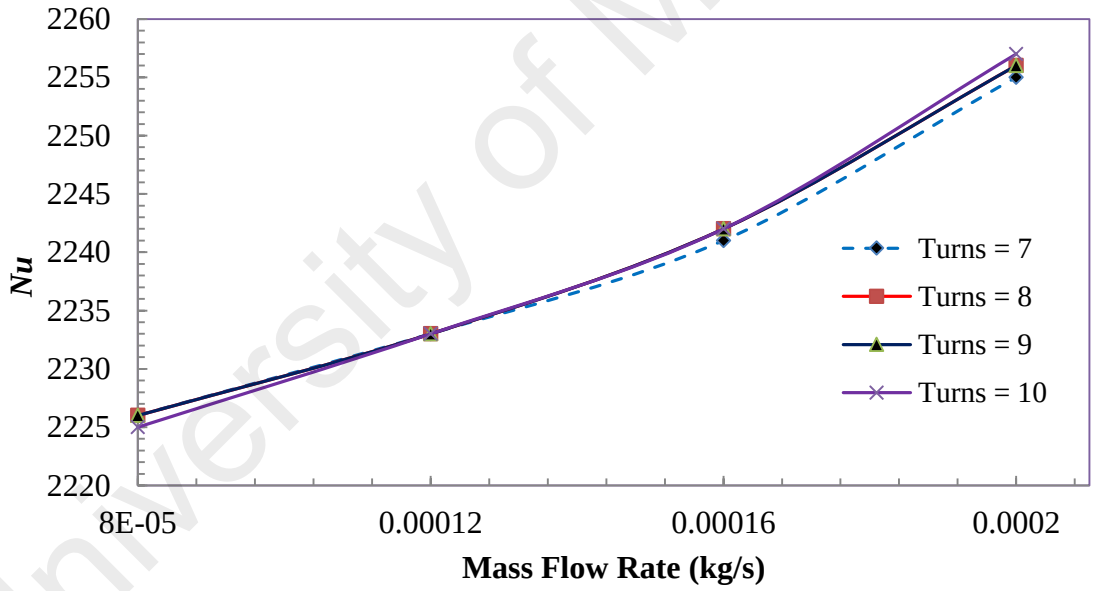

Figure 7.7: Variation of Nusselt number vs. mass flow rate for different number of turns (Constants; Pitch = 1mm, HR = 0.25mm, α = 2).

Figure 7.8 shows that the convective heat transfer increases on decreasing the aspect ratio. The difference in Nusselt number is more evident at smaller flow rates. This can be attributed to the residence time of the fluid whereby a minimum residence time is required

for the fluid to effectively absorb heat (Narrein and Mohammed, 2013). This effect tends to fade off at higher velocities.

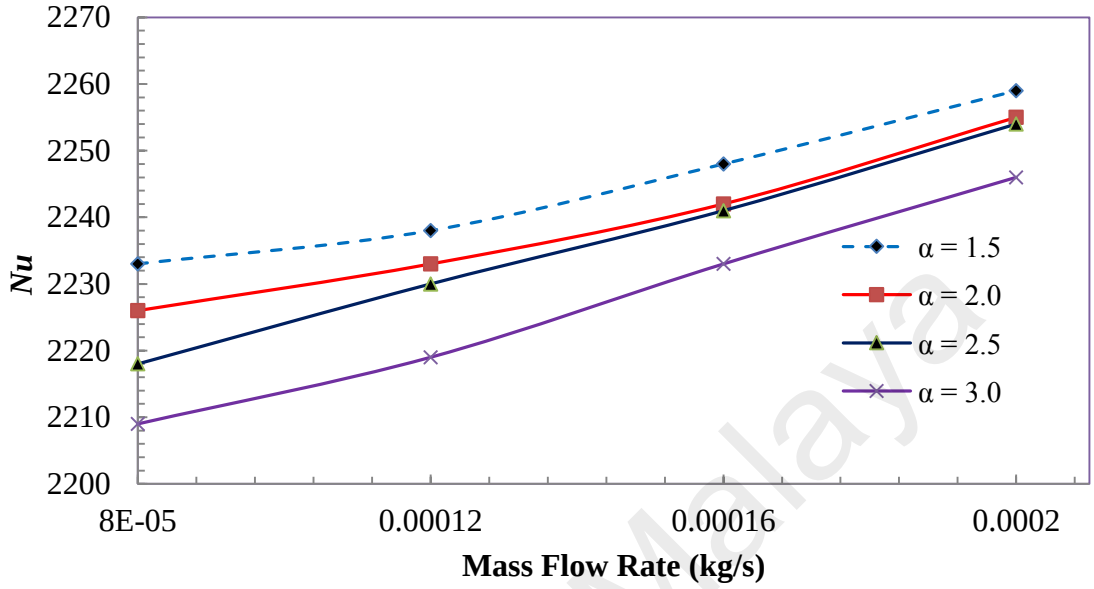

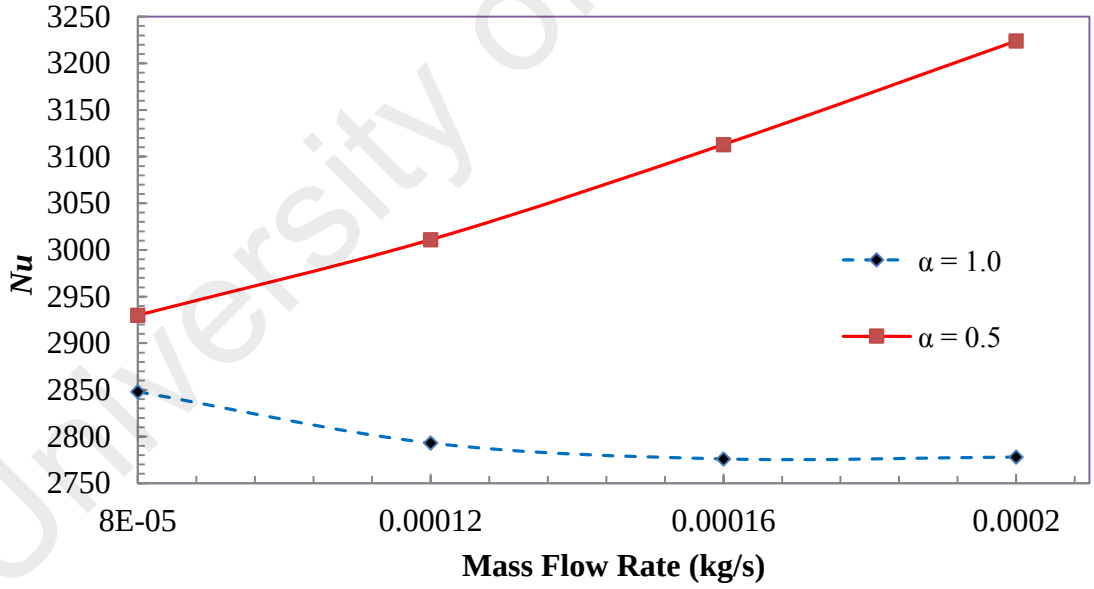

Figure 7.8: Variation of Nusselt number vs. mass flow rate for different aspect ratios (Constants; Pitch = 1mm, Turns = 7, HR = 0.25mm).

At higher mass flow rates, the overall bulk velocity of the fluid is decreased on increasing the hydraulic diameter. Hence, the overall convective heat transfer is reduced with the drop in velocity. It should be noted that the Nusselt number drops on increasing

the flow rate for α = 1 and this implies that local heat transfer conductance vary around the edge of the channel and move towards zero at the square corners (Kays and Crawford, 1993). Svino and Siegel (1964) found that poor convection occurs due to lower velocities at the corners. In addition, the overall effective heat transfer area is also decreased as the aspect ratio is reduced and this leads to lesser heat transfer.

7.2.2 The effects of geometrical parameters on the flow field.

Figure 7.9 through 7.12 shows the pressure drop analysis for all the geometrical parameters considered in this study. It can be inferred that pressure drop increases on increasing the mass flow rate for all cases. The pressure drop for different values of helix radius is portrayed in Figure 7.9. As the helix radius is increased, the magnitude of the main flow is intensified due to ease of flow and this leads to higher velocity and in turn produces larger pressure drop.

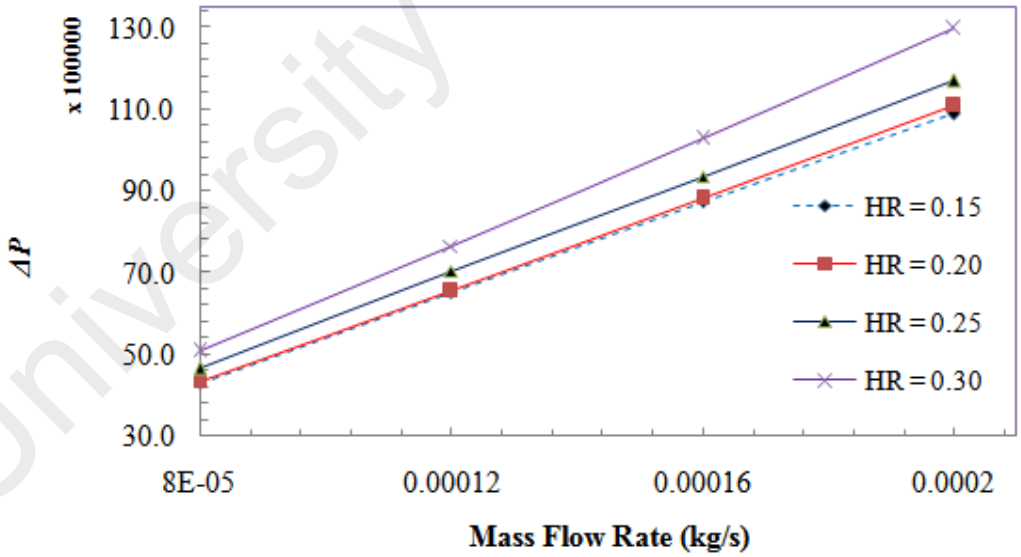

Figure 7.9: Pressure drop vs. mass flow rate for different helix radius (Constants; Pitch = 1mm, Turns = 7, α = 2).

Similar effects on pressure drop are noticed for variation in pitch as shown in Figure 7.10. As the pitch is increased, the torsion effects become more intense which leads to a

higher pressure drop. Increasing the number of turns also lead to additional pressure drop and this is due to the increase in overall length of the HMCHS as shown in Figure 7.11.

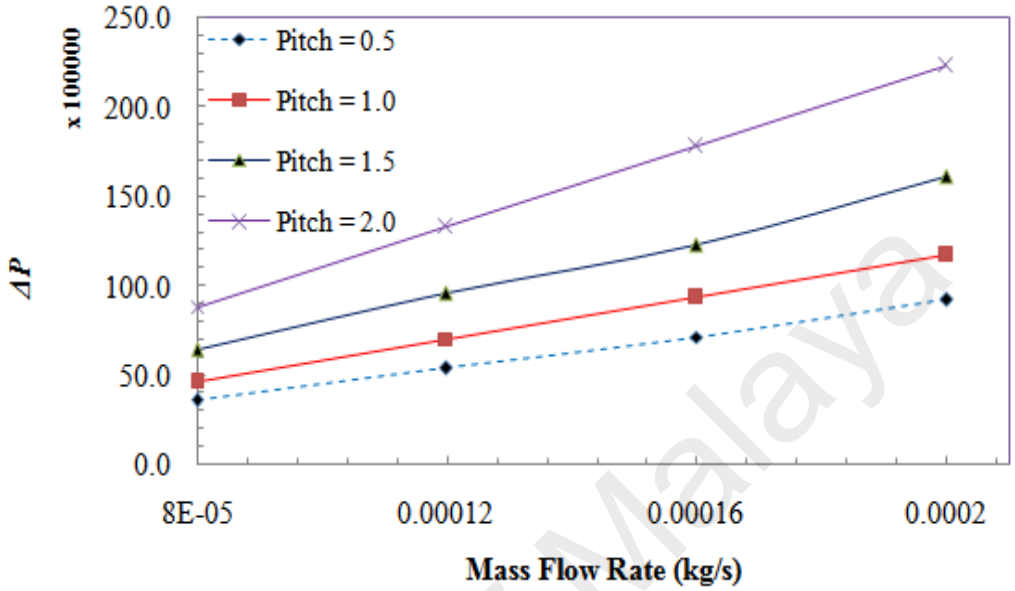

Figure 7.10: Pressure drop vs. mass flow rate for different pitch (Constants; HR = 0.25mm, Turns = 7, α = 2).

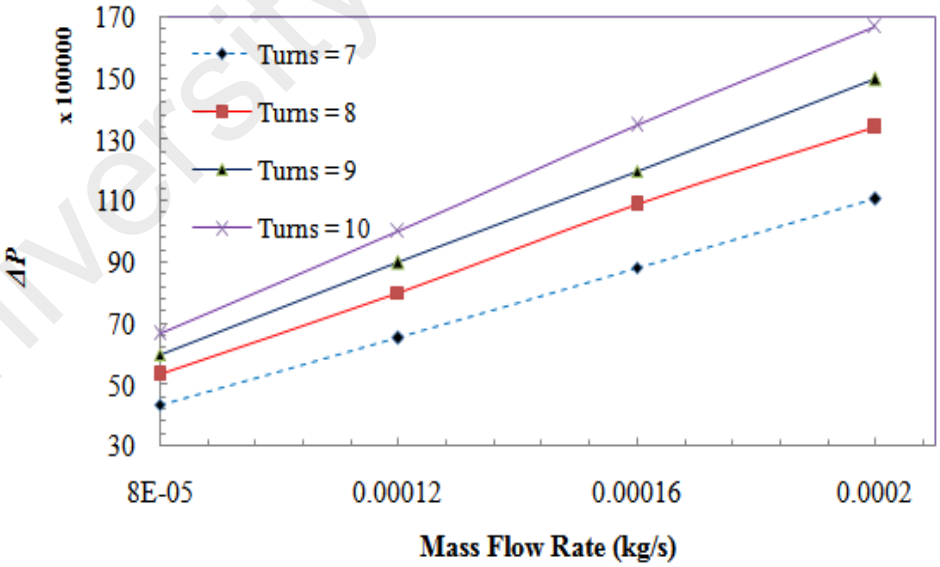

Figure 7.11: Pressure drop vs. mass flow rate for different number of turns (Constants; Pitch = 1mm, HR = 0.25mm, α = 2).

It can also be observed that pressure drop increases on decreasing the aspect ratio as depicted in Figure 7.12. As the aspect ratio becomes smaller, the overall bulk velocity becomes higher which directly results in additional wall shear stress. The pressure drop profile is different for aspect ratio 0.5 and 1.0 because the overall velocity change due change in area and the sides which are made or longer or shorter is different. The presence of porous medium in the HMCHS further adds to the pressure drop which already exists due to the secondary flow.

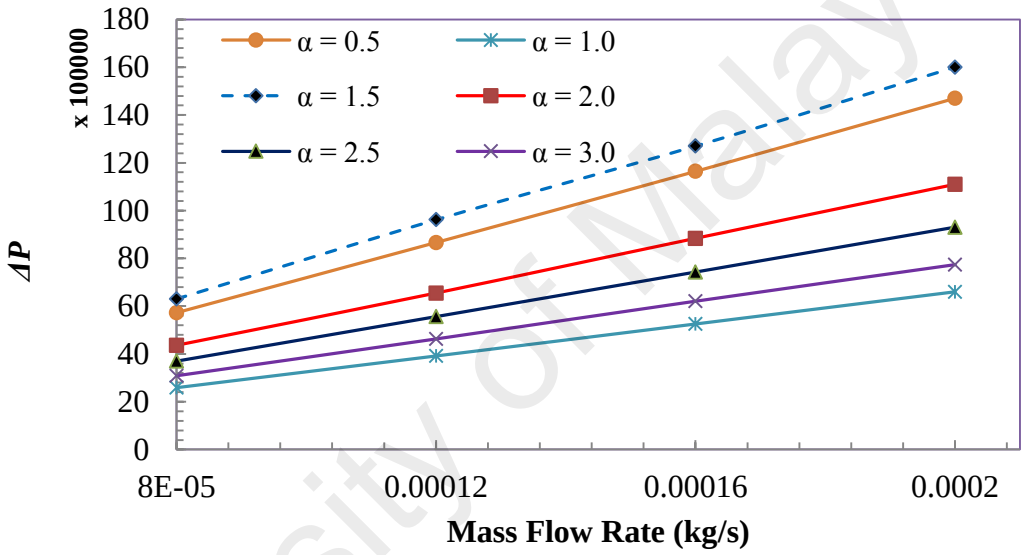

Figure 7.12: Pressure drop vs. mass flow rate for different aspect ratios.

7.2.3 HMCHSC performance

The performance index of the HMCHS is calculated using the following equation (Dang et al., 2011):

$$\eta = \frac{Q}{\Delta P} \tag{7.7}$$

where Q id the heat transfer and ΔP is the pressure drop. It is in an indication of the overall performance of the system based on pressure drop. It can be inferred from Table 7.4 that

the overall performance index is significantly lower for all the HMCHS compared to the straight microchannel except for the channel with the largest aspect ratio. The performance index tends improve as the helix radius is increased. A larger helix radius will encounter a smaller magnitude of secondary flow which leads to smaller pressure drop. Performance index decreases on increasing the pitch. Increasing the number of turns will lead to better overall heat transfer, hence giving a better performance index value. It can be also seen that performance index increases on increasing the aspect ratio. The porous medium lead to good thermal enhancement, however the pressure drop through the channel is very high.

Table 7.4: Performance index based on various geometrical parameters.

Parameters	Effects		Performance Index (W/Pa) x 10^{-5}	
			Non-Porous	Porous
Fixed	Straight		7.52	
Pitch = 1.0,	Helix Radius	0.15	1.38	0.11
Turn = 7,		0.20	2.06	0.13
Aspect Ratio = 2		0.25	2.64	0.15
		0.30	3.10	0.16
HR = 0.2,	Pitch	0.5	3.50	0.19
Turn = 7,		1.0	2.64	0.15
Aspect Ratio = 2		1.5	1.85	0.12
		2.0	1.35	0.09
Pitch = 1.0,	Turns	7	2.64	0.15
HR = 0.2,		8	2.65	0.15
Aspect Ratio = 2		9	2.67	0.15
		10	2.68	0.15
Pitch = 1.0,	Aspect Ratio	0.5	1.48	0.10
Turns = 7,		1.0	7.22	0.31
HR = 0.2		1.5	1.25	0.09
		2.0	2.64	0.15
		2.5	4.74	0.22
		2.0	7.66	0.30

7.3 Conclusions

Numerical study on the performance of HMCHS based on various geometrical parameters are analyzed with the presence of porous medium. The thermal field results show that HMCHS can contribute to better heat transfer enhancement as compared to a straight microchannel of similar length and hydraulic diameter. The results also showed that convective heat transfer tends to improve as the helix radius is reduced and when the pitch is increased. Increasing the overall length of the HMCHS leads to a higher pressure drop and lower convective heat transfer. Reducing the aspect ratio leads to an increase in the overall bulk fluid velocity which results to better convective heat transfer but with a penalty in pressure drop. The channel with the largest aspect ratio has the best performance index as compared to all other cases. The porous medium allows better thermal contact between the outer wall and fluid, hence increasing the heat transfer rate.

CHAPTER 8: INFLUENCE OF TRANSVERSE MAGNETIC FIELD ON MICROCHANNEL HEAT SINK PERFORMANCE

The numerical investigation on heat transfer and fluid flow characteristics in a rectangular microchannel heat sink (MCHS) under the influence of transverse magnetic field is presented in this chapter. The effects of Hartmann number, channel aspect ratio, total channel height and total channel width on heat transfer and fluid flow characteristics are widely investigated.

8.1 Mathematical Modelling

8.1.1 Governing equations

The microchannel heat sink considered in this study is shown schematically in Figure 8.1. Heat is transferred from the bottom wall of the MCHS to the working fluid which is water in this case. Several assumptions are made on the operating conditions of the MCHS: (i) the MCHS operates under steady-state conditions; (ii) the fluid remains single phase along the MCHS; (iii) the properties of the MCHS material are temperature independent; (iv) the external heat transfer effects are ignored; (v) the outer walls of the MCHS are adiabatic. The uniform external magnetic field of constant magnitude B_0 is applied in the negative y-direction. The effect of the electromagnetic field is introduced into the equations of motion through $\boldsymbol{J} \times \boldsymbol{B}$ the term, which is the vector product of the electric current density and magnetic field inductance $\boldsymbol{B}$ and represents the Lorentz force. The electric current density $\boldsymbol{J}$ is calculated from Ohm's law. The electric current $\boldsymbol{J}$ and the electromagnetic force $\boldsymbol{F}$ are defined by $\boldsymbol{J} = \sigma_e(\boldsymbol{V} \times \boldsymbol{B} - \nabla\Phi)$, $\nabla . \boldsymbol{J} = 0$, and $\mathbf{F} = \mathbf{J} \times \mathbf{B}$ (Sivasankaran et al., 2011).

The governing equations for flow and heat transfer in the MCHS are:

Continuity equation:

$$\nabla \circ \vec{v} = 0 \tag{8.1}$$

Momentum equation:

$$(\vec{v} \circ \nabla)\vec{v} = \frac{1}{\rho}\nabla p + \nu \Delta \vec{v} + \frac{1}{\rho}(j \times B) \tag{8.2}$$

Energy equation:

$$(\vec{v} \circ \nabla)T = \alpha \Delta T \tag{8.3}$$

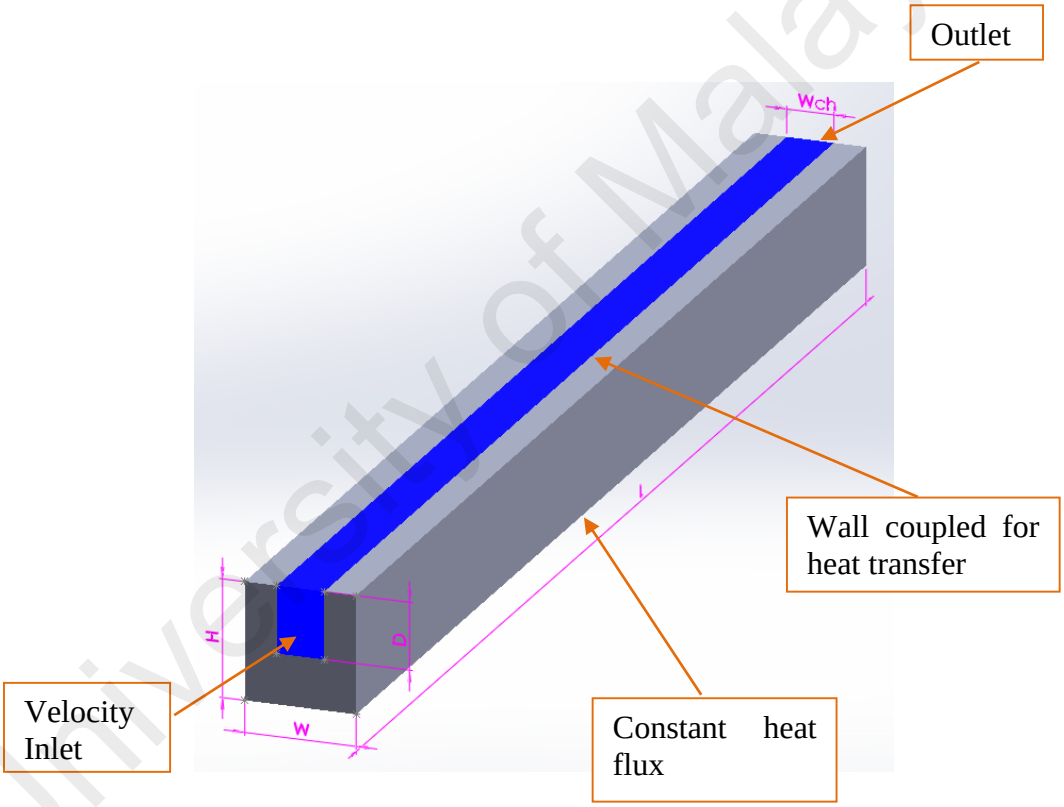

Figure 8.1: Schematic diagram of the computational domain of MCHS.

8.1.2 Boundary conditions

Water is set to flow through the channel and the bottom wall of the MCHS is heated with a constant heat flux of 1×10^6 W/m^2. The inlet velocity is varied to produce Reynolds number in the range of Re = 500-1000. Three-dimensional laminar flow is considered for the entire study. The inlet temperature of the water is set to 300K. The outlet is set to

pressure outlet and the wall between the channel (fluid region) and solid region is set to "coupled for heat transfer". The outer wall of the MCHS is set as adiabatic.

8.1.3 Numerical Method

The numerical computations are carried out by solving the governing equations along with the boundary conditions using the finite volume method. The SIMPLE algorithm is adopted to couple the velocity and pressure field. The second-order upwind differencing scheme is used for the convective terms. The diffusion term in the momentum and energy equations are approximated by the second-order central difference scheme which gives a stable solution. Numerical simulation is carried out for different combinations of pertinent parameters such as (i) Hartmann number, (ii) channel aspect ratio, (iii) total channel height and (iv) total channel width to investigate the effects on MCHS. The convergence criterion is set to be 1×10^{-5}. The convergence criterion required that the maximum relative residual for mass, momentum and energy to be smaller than 1×10^{-6}. Second order discretization scheme is used for pressure, momentum and energy equations. The under-relaxation factor parameters for pressure and momentum is set to 0.3 and 0.7 respectively.

8.1.4 Straight MCHS and Magnetohydrodynamics (MHD) Analysis Model Validation

The model validation is done based on the geometry which was first used by Xia et al. (2011). Water with an inlet velocity of 4 m/s was set to flow through the channel and the bottom wall of the MCHS is heated with a constant heat flux of 1×10^6 W/m^2. The thermal field results are compared with the analytical results suggested by Philips (1990).

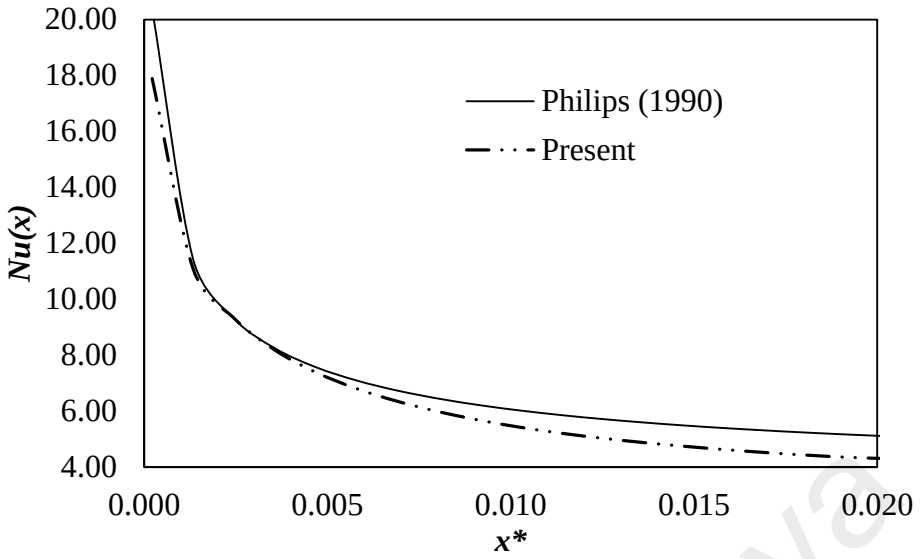

Figure 8.2: Model validation for straight MCHS

The results for transverse magnetic field are validated with the correlation presented by Back (1968). It can be inferred that the thermal field results are in very good agreement with the proposed correlation as seen in Figure 7.2.

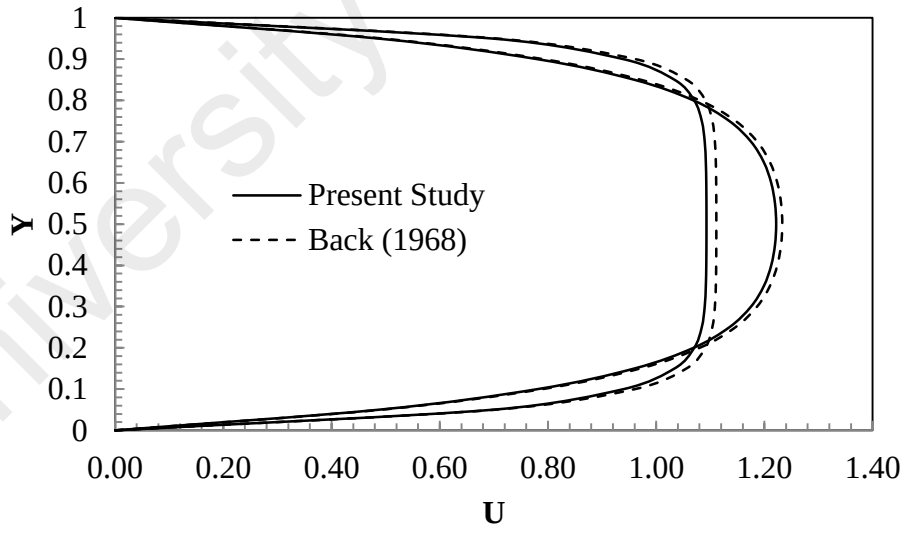

Figure 8.3: Model validation for transverse magnetic field

8.2 Results and Discussion

8.2.1 The effects of transverse magnetic field on the thermal field

The effect of Hartmann number on the thermal field is presented via the Nusselt number in Figure 8.4. The local convective heat transfer coefficient and Nusselt number is calculated using the following equation:

$$h(x) = \frac{q}{(T_{Wall}(x) - T_{Fluid}(x))} \tag{8.4}$$

$$Nu(x) = \frac{h(x)D_h}{\lambda} \tag{8.5}$$

where q represents heat flux, h is the heat transfer coefficient, D_h is the hydraulic diameter and λ is the thermal conductivity of the working fluid. The average Nusselt number can be obtained by:

$$Nu = \frac{1}{L}\int_0^L Nu\,(x).dx \tag{8.6}$$

where L represents the channel length.

It can be seen from the figure that the Nusselt number increases on increasing the Reynolds and Hartmann numbers. In normal cases, the flow becomes fully developed after a certain entry length. However, the magnetic field introduced in this study prevents the fluid from reaching a fully developed state which directly leads to the enhancement in heat transfer. An undeveloped flow will have a higher velocity at the near wall region as compared to a developed region which can be seen from the profile in Figure 8.3. The higher velocity near the wall region leads to better convective heat transfer. As the magnitude of the magnetic field is increased, the effect is further intensified to produce better heat transfer enhancement. This effect can be further presented by comparing the temperature contour at the channel near end region which is illustrated in Figure 8.5.

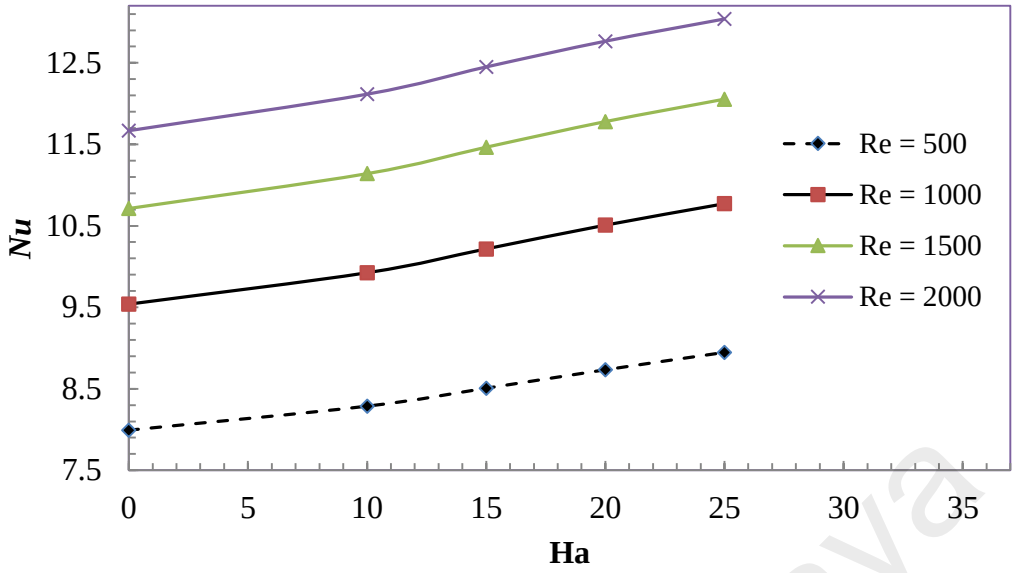

Figure 8.4: Variation of Nusselt number vs. Hartmann number for various Reynolds number

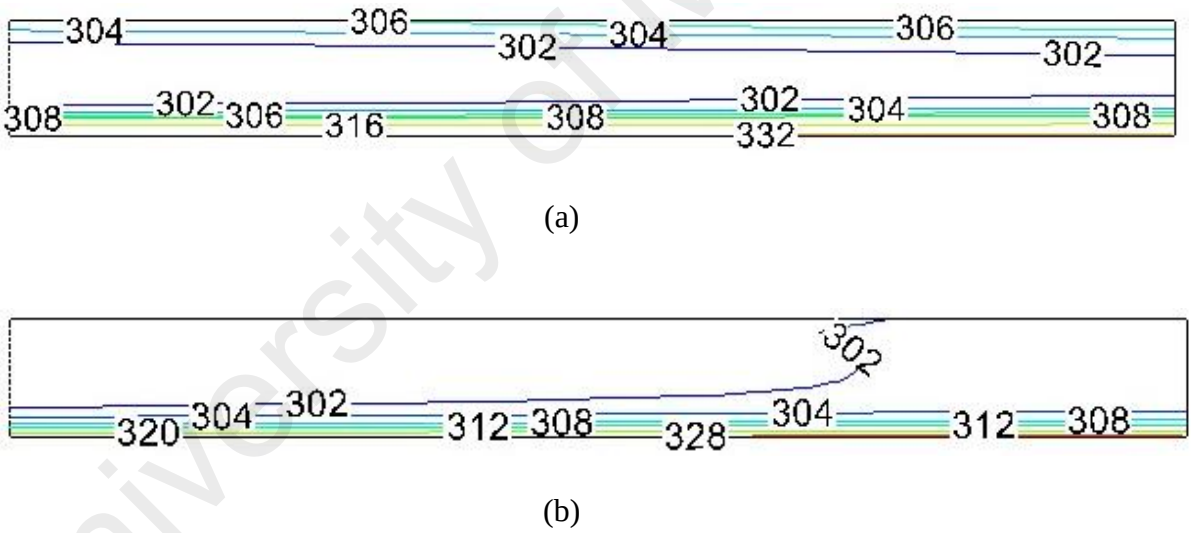

(a)

(b)

Figure 8.5: Isotherms for (a) Ha = 0 and (b) Ha = 25 with Re = 500

The effect of variation of the aspect ratio of MCHS performance is portrayed in Figure 8.6. Increase in the aspect ratio leads to an increase in the Nusselt number and the increment is further enhanced in the presence of the magnetic field for the same reason which is described earlier. The aspect ratio is varied by increasing the channel depth, D (i.e. height) while keeping the constant channel width. Previous literatures suggest that local heat transfer conductance vary around the edge of the channel and move towards

zero at the square corners (Kays and Crawford, 1993). Svino and Siegel (1964) found that poor convection occurs due to lower velocities at the corners. The dominance of these effects on convective heat transfer tends to fade off at higher aspect ratio which is also observed in this study where the Nusselt number increases on increasing the aspect ratio. The surface heat flux contour for this study is shown in Figure 8.7. In addition, as the aspect ratio is increased, the overall wall area increases and this leads to overall increases in heat flux. Though the velocity will decrease as the aspect ratio is increased for a constant Re, the percentage increase in overall heat input into the system is much higher compared to the velocity reduction. Apart from that, the residence time also plays a major role in the overall heat transfer rate. The residence time is basically the amount of time the fluid is at a particular location to absorb the heat from the outer surface. Hence, an optimum balance between residence time and velocity can increase the overall Nusselt number.

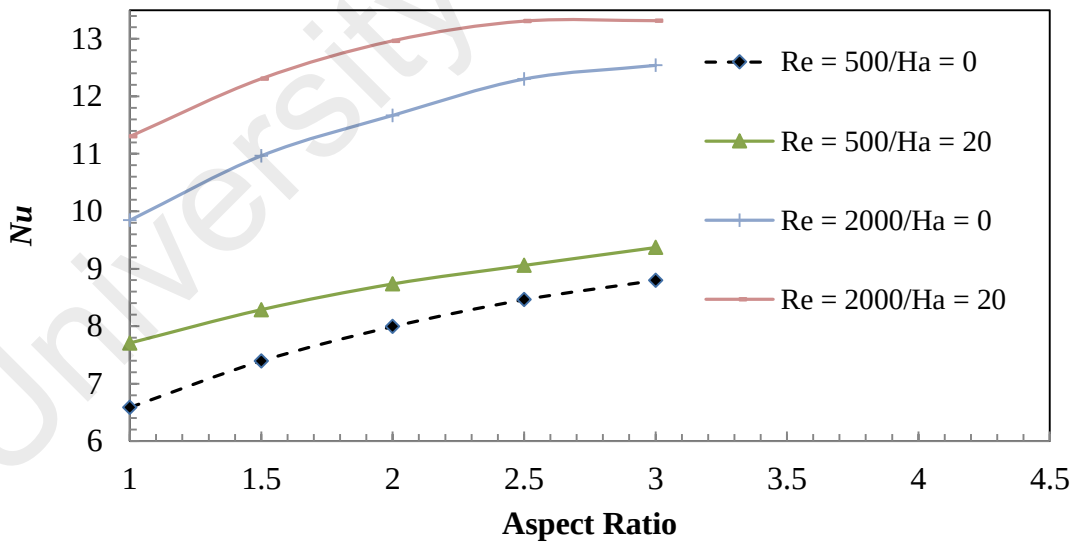

Figure 8.6: Variation of Nusselt number vs. Aspect Ratio for various Reynolds number and Hartmann number

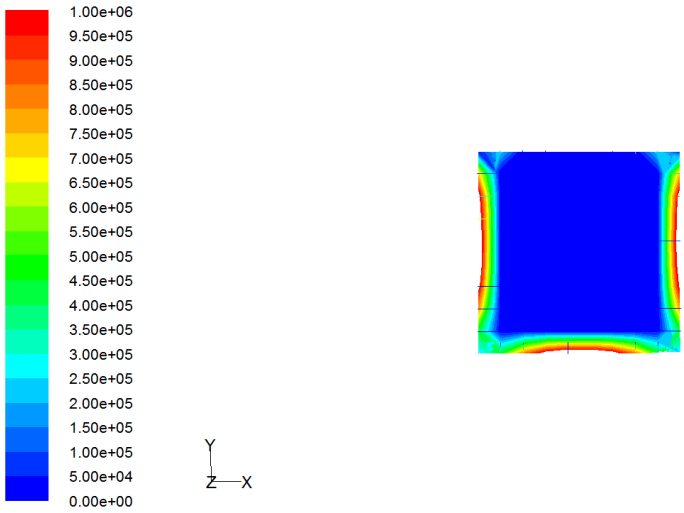

(a)

(b)

Figure 8.7: Surface heat flux contour for channel with (a) 1.0 and (b) 3.0 aspect ratio

Figure 8.8. shows the variation of Nusselt number with total channel height (H). A minor change in Nusselt number is observed when the channel height is increased from 300 to 350 µm. The thickness between the channel and bottom surface plays a vital role in determining the total thermal resistance. An optimum thickness is required for optimum heat transfer which are presented in detail by Biswal et al. (2009).

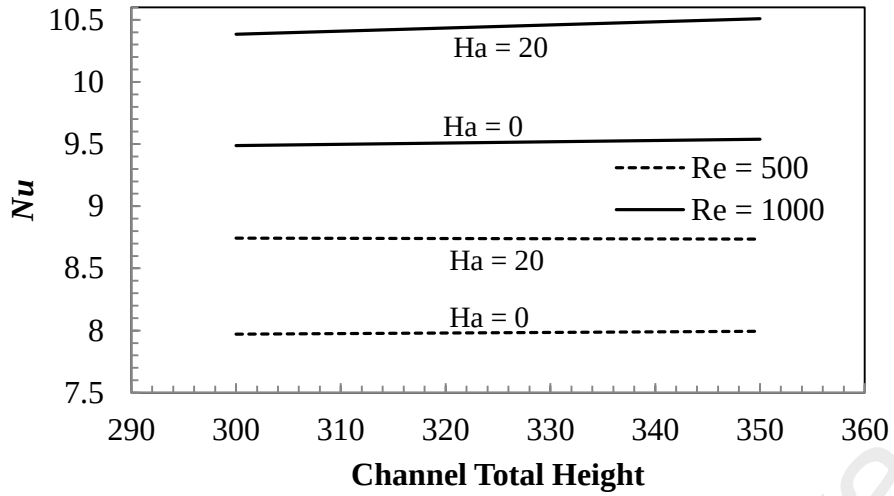

Figure 8.8: Variation of Nusselt number vs. total channel height

The effect of channel total width (W) is presented in Figure 8.8. There is no considerable change in Nusselt number observed when the channel width is varied.

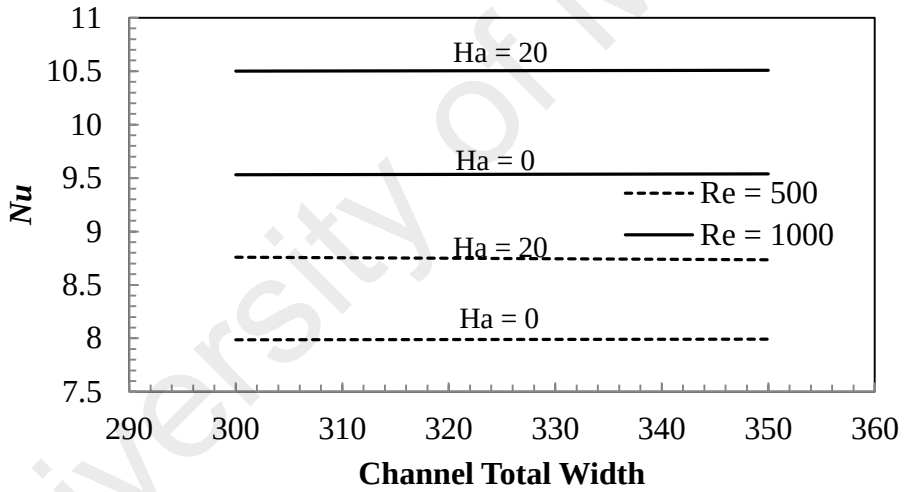

Figure 8.9: Variation of Nusselt number vs. total channel width

8.2.2 The effects of transverse magnetic field on the flow field

Figure 7.10. shows the pressure drop for different values of the Hartmann number. It can be seen that the pressure drop increases on increasing the Hartmann number. The effect of magnetic field prevents the flow from reaching a fully developed state to a certain extent. While this is happening, the velocity at wall tends to be higher than that of a fully developed flow which directly leads to a higher shear stress at this region. A higher wall shear stress would eventually lead to a higher pressure drop.

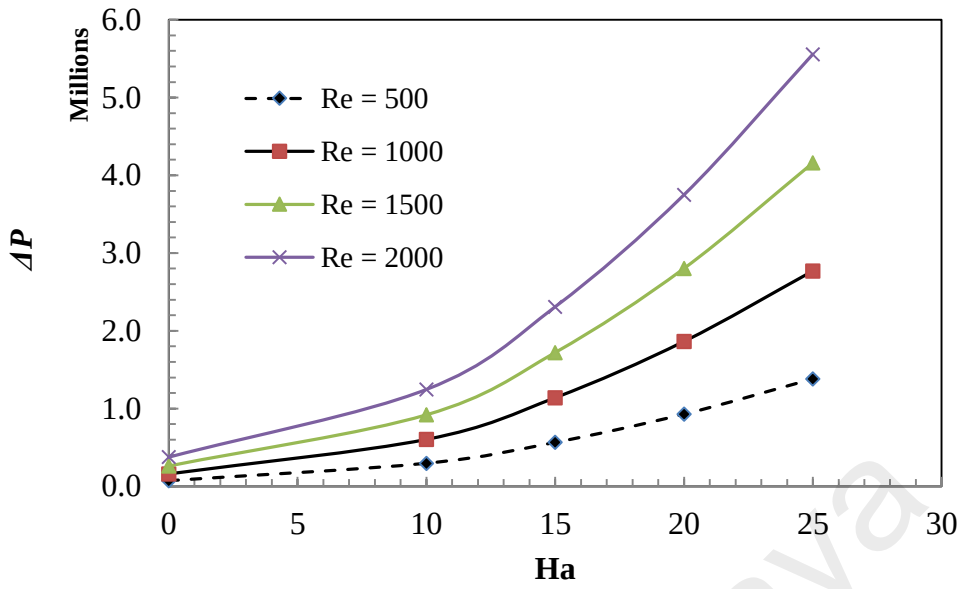

Figure 8.10: Pressure drop vs. Hartmann number for different Reynolds number

In the case of different aspect ratios, it is observed from Figure 7.11 that pressure drop tends to decrease with increasing the aspect ratio. A larger hydraulic diameter allows for a relatively lower velocity which results in a much lower shear stress at the near wall region. This can help to reduce the overall pressure drop through the MCHS.

The effect of total channel height and width on the pressure drop (not illustrated here) showed no significant difference. However, a small variation is present and this can be accounted for the variance in density due to some changes in the overall fluid temperature which can have a direct effect on the velocity.

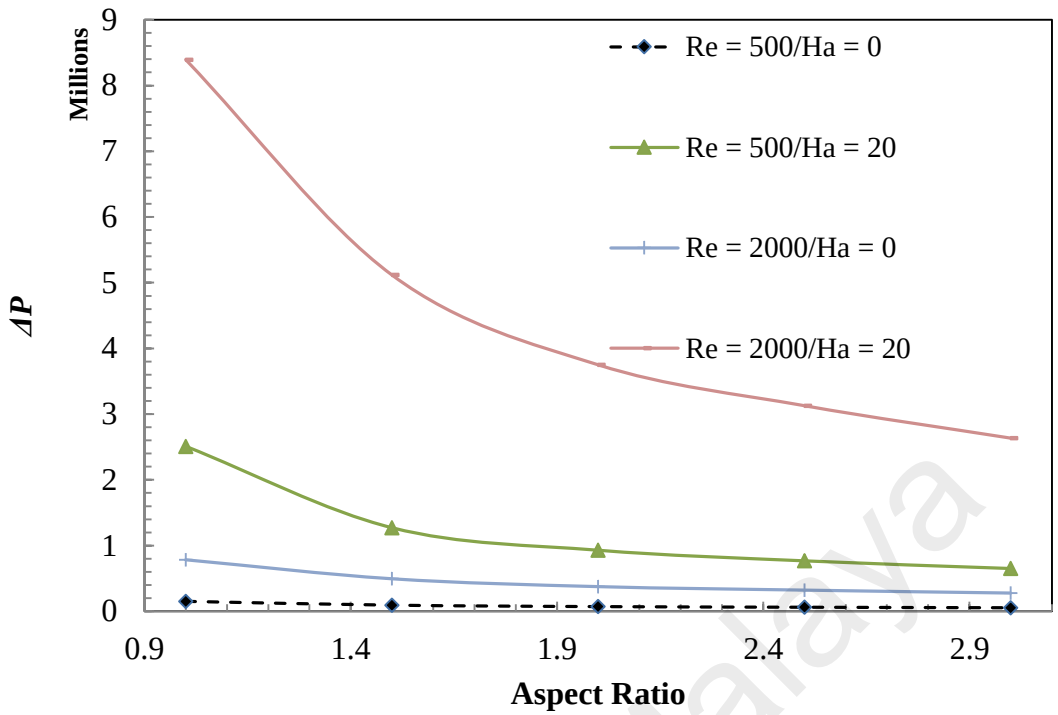

Figure 8.11: Pressure drop vs. aspect ratio for different Reynolds number and Hartmann number

8.3 Conclusions

Thermal and flow field characteristics of a MCHS under the influence of magnetic field are studied numerically. The effects of Hartmann number, aspect ratio, total channel height and total channel width on flow and temperature field are investigated.

- Magnetic field is able to increase the convective heat transfer substantially. It is found that convective heat transfer can be enhanced by increasing the magnitude of the magnetic field, but is accompanied by significant amount of pressure drop.
- Nusselt number seems to also increase on increasing the aspect ratio with a reduction in pressure drop.
- Considerable changes in the thermal and flow fields are also observed on varying total channel height and width.

CHAPTER 9: INFLUENCE OF TRANSVERSE MAGNETIC FIELD ON TRAPEZOIDAL MICROCHANNEL HEAT SINK

This chapter discusses the effects of transverse magnetic field on heat transfer and fluid flow characteristics in a trapezoidal microchannel heat sink (TMCHS). The effects of the Hartmann number, channel bottom width, channel top width and channel height on heat transfer and fluid flow characteristics are widely investigated.

9.1 Mathematical Modelling

9.1.1 Governing equations

The trapezoidal microchannel heat sink considered in this study is shown schematically in Figure 9.1. The heat is transferred from the bottom wall of the TMCHS to the working fluid which is water in this case. Several assumptions are made on the operating conditions of the TMCHS as follows:

(i) The TMCHS operates under steady-state conditions;

(ii) The fluid remains single phase along the TMCHS;

(iii) The properties of the TMCHS material are temperature independent;

(iv) The external heat transfer effects are ignored;

(v) The outer walls of the TMCHS are adiabatic.

The effect of the electromagnetic field is introduced into the equations of motion through $\boldsymbol{J} \times \boldsymbol{B}$ the term, which is the vector product of the electric current density and magnetic field inductance $\boldsymbol{B}$ and represents the Lorentz force. The electric current density $\boldsymbol{J}$ is calculated from Ohm's law. The electric current $\boldsymbol{J}$ and the electromagnetic force $\boldsymbol{F}$ are defined by $\boldsymbol{J} = \sigma_e(\boldsymbol{V} \times \boldsymbol{B} - \nabla \Phi)$, $\nabla . \boldsymbol{J} = 0$, and $\mathbf{F} = \mathbf{J} \times \mathbf{B}$ (Sivasankaran et al., 2011).

The governing equations for fluid flow and heat transfer in the TMCHS are:

Continuity equation:

$$\nabla \circ \vec{v} = 0 \tag{9.1}$$

Momentum equation:

$$(\vec{v} \circ \nabla)\vec{v} = \frac{1}{\rho}\nabla p + \nu \Delta \vec{v} + \frac{1}{\rho}(j \times B) \tag{9.2}$$

Energy equation:

$$(\vec{v} \circ \nabla)T = \alpha \Delta T \tag{9.3}$$

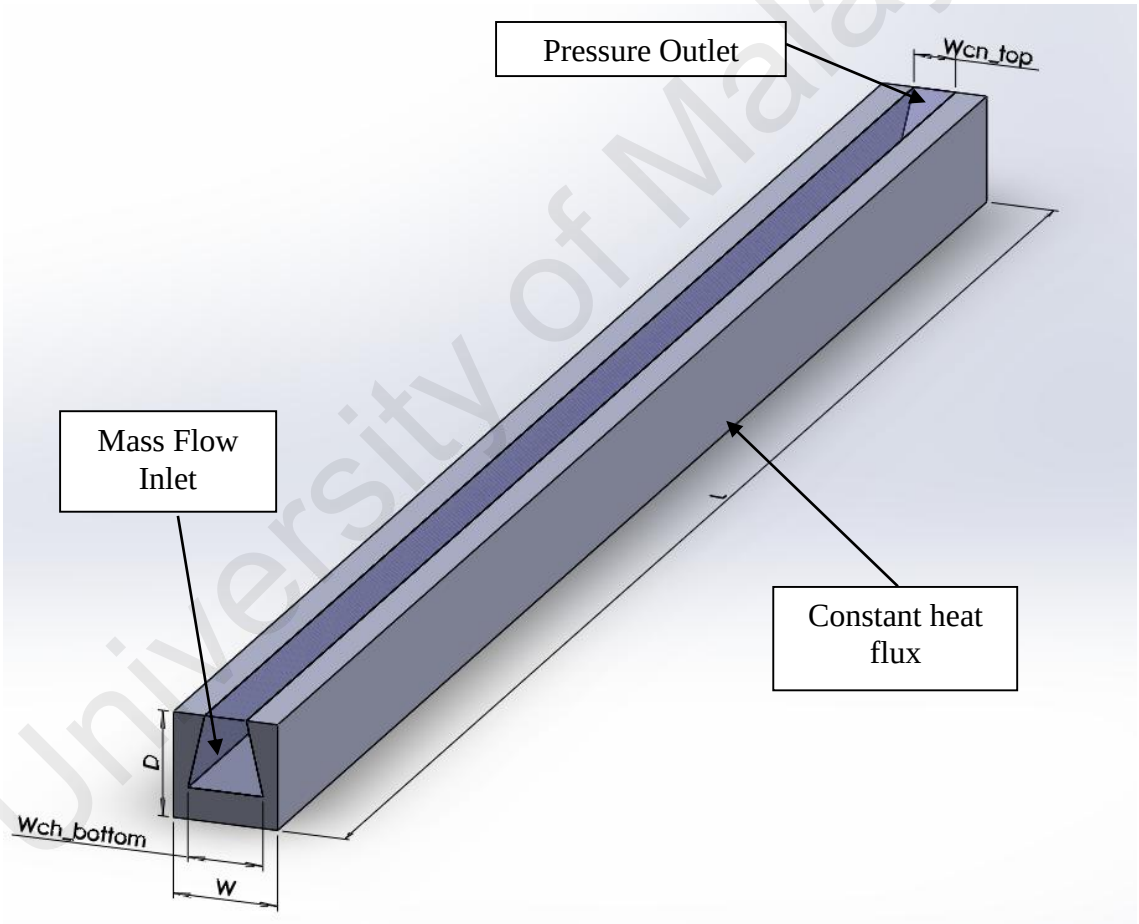

Figure 9.1: Schematic diagram of the computational domain of TMCHS.

9.1.2 Boundary conditions

Water is set to flow through the channel and the bottom wall of the TMCHS is heated with a constant heat flux of 1×10^6 W/m^2. Mass flow rate values in the range of 0.00008 to 0.0002 kg/s are considered. Three-dimensional laminar flow is considered for the entire study. The inlet temperature of the water is set to 300K. The outlet is set to pressure outlet and the wall between the channel (fluid region) and solid region is coupled for heat transfer. The outer wall of the MCHS is set as adiabatic.

9.1.3 Numerical Method

The numerical computations are carried out by solving the governing equations along with boundary conditions using the finite volume method. The SIMPLE algorithm is adopted to coupling the velocity and pressure field. The second-order upwind differencing scheme is used for the convective terms. The diffusion term in the momentum and energy equations are approximated by the second-order central difference scheme which gives a stable solution. Numerical simulation is carried out for different combinations of pertinent parameters such as Hartmann number, channel bottom width, channel depth and channel top width to investigate the effects on TMCHS. The convergence criterion required that the maximum relative residual for mass, momentum and energy to be smaller than 1×10^{-6}. Second order discretization scheme is used for pressure, momentum and energy equations. The under-relaxation factor parameters for pressure and momentum is set to 0.3 and 0.7 respectively.

9.2 Results and Discussion

9.2.1 The effects of transverse magnetic field on the thermal field

The effect of Hartmann number on heat transfer rate is presented the Nusselt number as shown in Figure 9.2. The local convective heat transfer coefficient and Nusselt number is calculated using the following equation:

$$h(x) = \frac{q}{(T_{Wall}(x) - T_{Fluid}(x))} \tag{9.4}$$

$$Nu(x) = \frac{h(x)D_h}{\lambda} \tag{9.5}$$

where q represents heat flux, h is the heat transfer coefficient, D_h is the hydraulic diameter and λ is the thermal conductivity of the working fluid. The average Nusselt number can be obtained by:

$$Nu = \frac{1}{L}\int_0^L Nu\,(x).dx \tag{9.6}$$

where L represents the channel length.

It can be observed from the figure that the Nusselt number increases on increasing the mass flow rate and Hartmann number. The increase in mass flow rate leads to an increase in the overall velocity which directly enhances the convective heat transfer. Nusselt number increases about 16% when *Ha* increases from 0 to 25. The transverse magnetic field tends to create a force in the opposite direction of the flow, thus preventing the flow to reach a fully developed state, hence directly resulting in the enhancement of convective heat transfer. As the magnitude of the magnetic field is increased, the effect is further intensified to produce better heat transfer where similar trends were observed by Aminossadati et al. (2011).

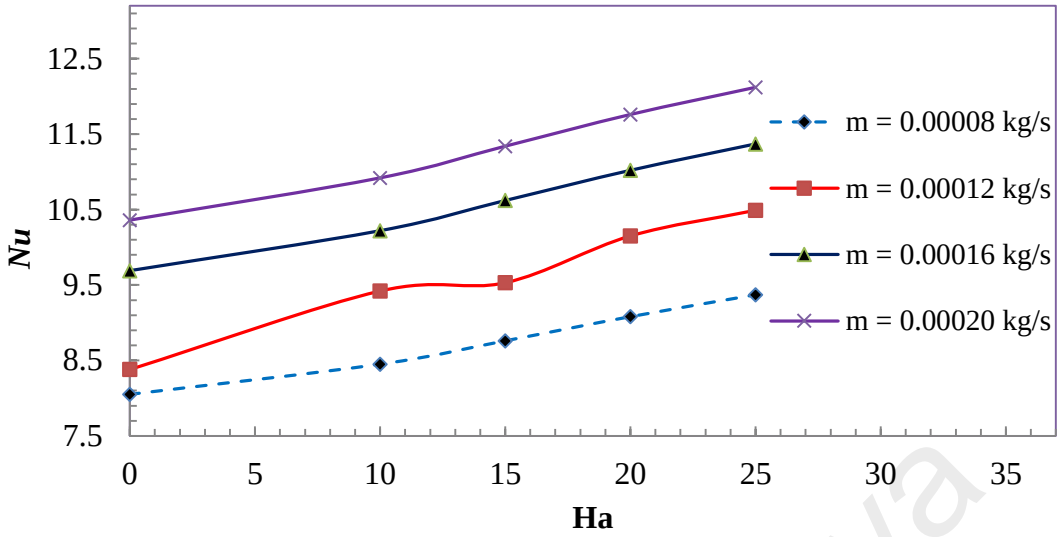

Figure 9.2: Variation of Nusselt number vs. Hartmann number for various mass flow rates.

The effect of channel bottom width on Nusselt number is portrayed in Figure 9.3. For the case of Ha = 0, an increase in channel bottom width results in the decrease of Nusselt number.

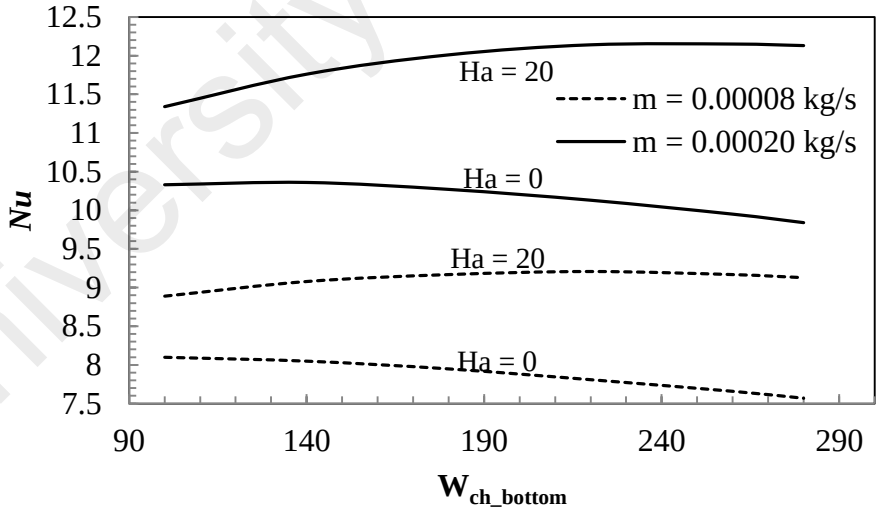

Figure 9.3: Variation of Nusselt number vs. channel bottom width.

It can be seen from Figure 8.4 that heat flux varies around the edge of the channel and move towards zero at the sharp corners. This is due to poor convection which occurs as a result of lower velocities at the corners. The decline is further intensified as the angle of the corner becomes sharper.

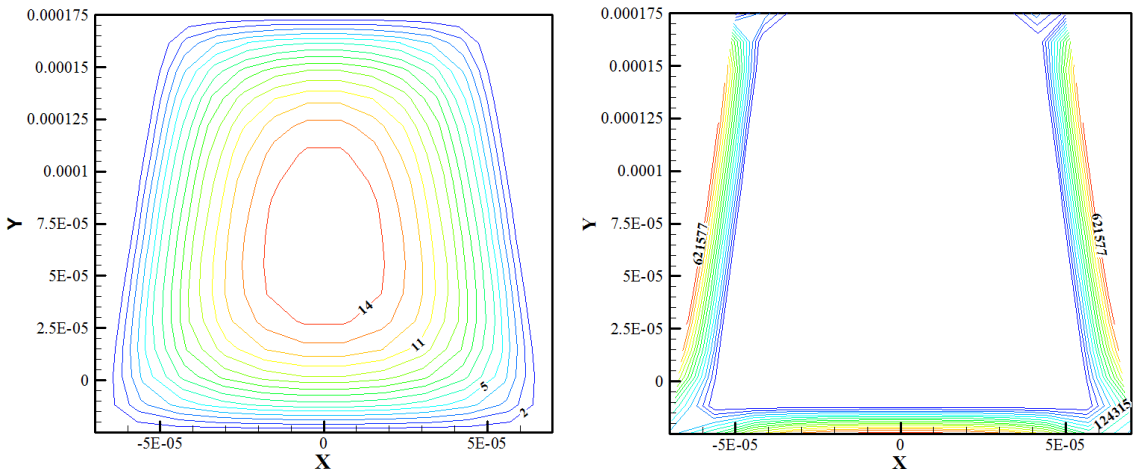

(a)

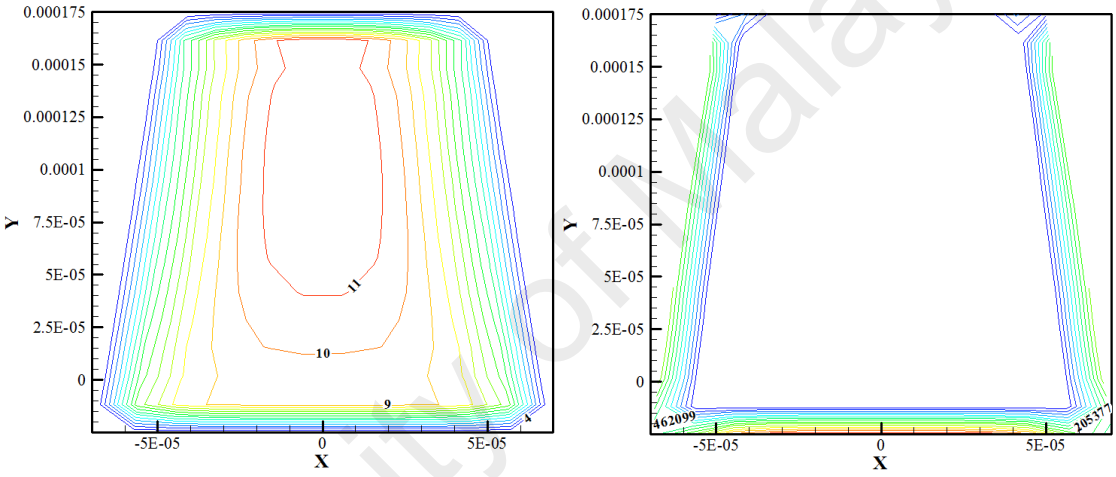

(b)

Figure 9.4: Velocity (left) and surface heat flux (right) contour for (a) Ha = 0 and (b) Ha = 25 at $\dot{m} = 0.0002\ kg/s$

An optimum trend is observed in the presence of the magnetic field whereby an enhancement is first observed on increasing the channel bottom width and later followed by a decrease in Nusselt number. The magnetic field preserves a relatively higher velocity at the corners up to an optimum corner angle, however the effect tends to fade off as the corners become very sharp past the optimum angle.

Figure 9.5 shows the variation of Nusselt number with channel depth. A minor change in Nusselt number is observed when the channel depth is varied. The thickness between the outer wall and channel bottom surface plays a vital role in determining the total thermal resistance. An optimum thickness is required for optimum heat transfer which is studied and in detail by Biswal et al. (2009) for rectangular channels. It can be seen from the study that Nusselt number increases on increasing the channel depth in the absence of magnetic field and the opposite is observed in the presence of magnetic field.

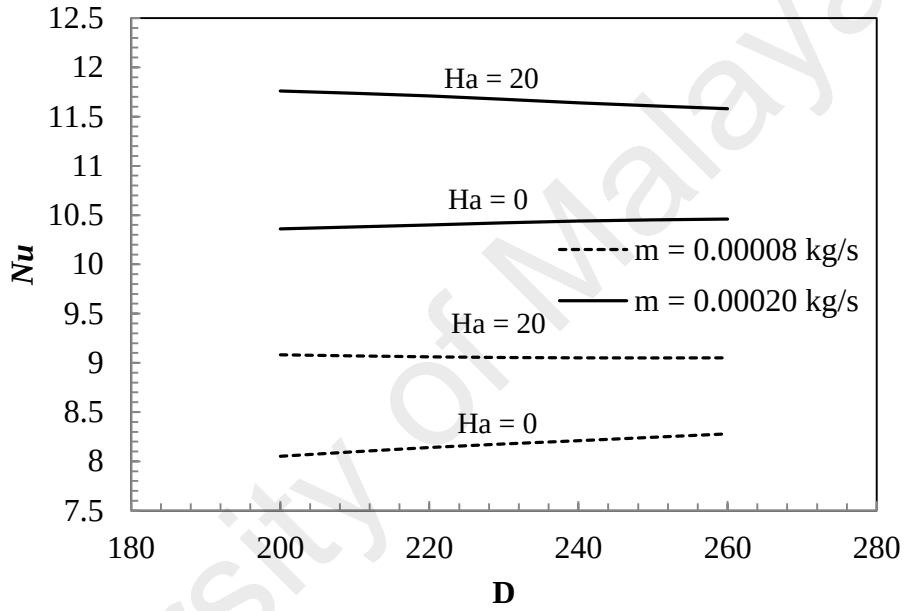

Figure 9.5: Variation of Nusselt number vs. channel depth.

The effect of channel top width is presented in Figure 9.6. The Nusselt number decreased almost linearly on increasing the channel top width. For this case, the effect of velocity plays a more dominant role whereby the overall bulk velocity of the fluid is decreased on increasing the channel top width. Hence, the overall convective heat transfer is reduced with the drop in velocity.

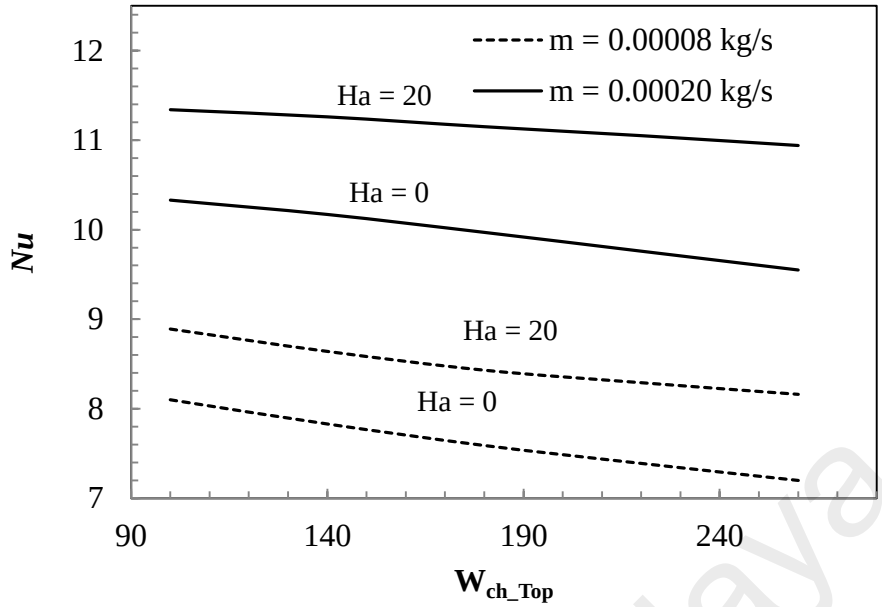

Figure 9.6: Variation of Nusselt number vs. channel top width

9.2.2 The effects of transverse magnetic field on the flow field

The flow field performance of the TMCHS is evaluated in terms of pressure drop. The value is obtained by acquiring the net area-weighted average difference between the inlet and outlet. Figure 9.7 shows the pressure drop for different values of the Hartmann number. It can be seen that the pressure drop increases on increasing the Hartmann number. The effect of magnetic field prevents the flow from reaching a fully developed state to a certain extent. While this is happening, the velocity at wall tends to be higher (non-parabolic velocity profile) than that of a fully developed flow which directly leads to a higher shear stress at this region. A higher wall shear stress would eventually lead to a higher pressure drop. As for the other cases (not illustrated here), the pressure drop decreased on increasing the W_{ch_bottom}, D, and W_{ch_top}. The increase in hydraulic diameter leads to a decrease in the overall bulk velocity, which tends to reduce the magnitude of shear stress at the wall region and directly resulting on a lower pressure drop.

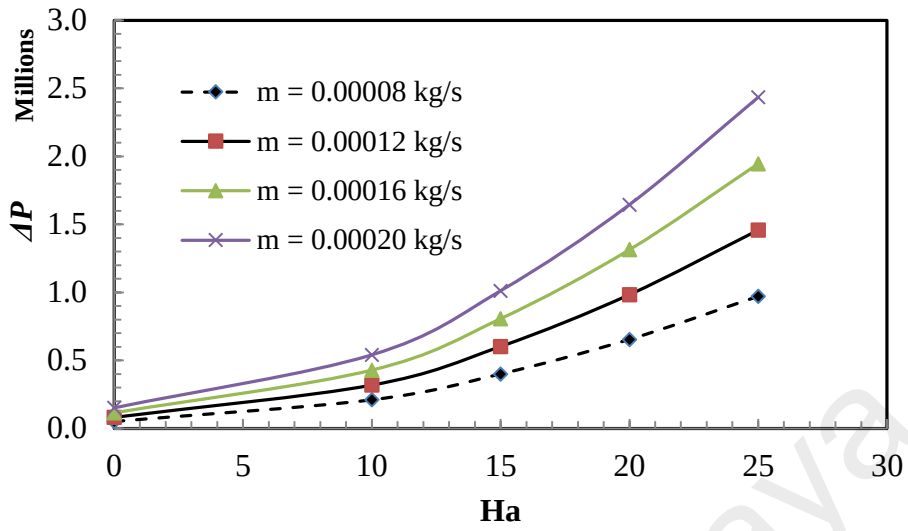

Figure 9.7: Pressure drop for various mass flow rates vs. Hartmann number

9.3 Conclusions

Thermal and flow field characteristics of a TMCHS under the influence of transverse magnetic field is studied numerically. The effects of Hartmann number, channel bottom width, top width and depth on the flow and temperature fields are investigated.

- Magnetic field is able to increase the convective heat transfer substantially in the TMCHS. It is found that convective heat transfer can be enhanced on increasing the magnitude of the magnetic field, but is accompanied by large amount of pressure drop.
- Nusselt number decreases on increasing the channel bottom width in the absence of magnetic field and, an optimum profile is observed in presence of magnetic field.
- Considerable changes in the thermal and flow fields are also observed when the total channel depth is varied due to thermal resistance.
- A decline in Nusselt number is observed when the channel top width is increased.

CHAPTER 10: CONCLUSIONS AND SUMMARY FOR FUTURE WORK

The main objective of this research was to study the various passive and active thermal enhancement techniques which can be applied to MCHS. The effects of helical structure, porous medium, nanofluids, pulsating velocity inlet conditions and transverse magnetic field were considered.

10.1 Conclusions

The numerical results conclude that HMCHS can contribute to better heat transfer enhancement compared to a straight MCHS of similar length and hydraulic diameter. The convective heat transfer also increases on increasing the pitch and decreasing the helix radius due to the effects of secondary flow and torsion.

This study also shows that the mixture model used to predict nanofluid flow is much more accurate compared to the Eulerian-Eulerian and single phase method. The conventional mixture model thermal conductivity equation and viscosity equation are modified to produce more accurate results as the heat transfer enhancement can be over predicted.

Pulsating inlet flow conditions are able to increase convective heat transfer significantly with reduction in pressure drop. The thermal enhancement increase on increasing the amplitude and frequency. The heat transfer coefficient increases on increasing the nanoparticle volume concentration, but the Nusselt number performance decline as a result of increasing thermal conductivity.

Noticeable heat transfer enhancement is observed in the HMCHS filled with porous medium as compared to the non- porous case due to better thermal contact between the heated surface and fluid. However the amount of pressure is significantly higher due to the additional resistance in the channel.

Magnetic field is able to increase the convective heat transfer substantially in the MCHS. It is found that convective heat transfer can be enhanced on increasing the magnitude of the magnetic field, but is accompanied by large amount of pressure drop.

10.2 Recommendations for Future Work

These are some recommendations that could be made in the future of the MCHS research:

The current study conducted is based on numerical solution and the model validation is done based on curved geometries rather than a helical geometry itself. As such experimental work is required to validate the present numerical results.

Apart from that, the two-phase mixture model presented in this study is one of a kind and it is a pioneering effort. Hence the new model proposed in this study should be further continued with other combination of nanoparticles, base fluid and volume concentration.

Furthermore, there are studies in the literature which suggest that turbulent flow conditions are better compared to laminar flow conditions. As such, the comparison study should be carried out to identify the performance of each model.

REFERENCES

Abbasi, Y., Shirani, A. S., & Asgarian, S. (2015). Two-phase mixture simulation of Al_2O_3/water nanofluid heat transfer in a non-uniform heat addition test section. *Progress in Nuclear Energy*, 83, 356-364.

Akdag, U., Ackay, S., & Demiral, D. (2014). Heat transfer enhancement with laminar pulsating nanofluid flow in a wavy channel, *International Communications in Heat and Mass Transfer*, 59, 17-23.

Ali, M. E. (2006). Natural Convection Heat Transfer from Vertical Helical Coils in Oil. *Heat Transfer Engineering.* 27(3), 79-85.

Alam, A., & Kim, K. M (2012). Analysis of Mixing in a Curved Microchannel with Rectangular Grooves. *Chemical Engineering Journal*, 181-182, 708-716.

Alam, A., Arshad, A., & Kwang-Yong K. (2013). Mixing Performance of a Planar Micromixer with Circular Obstructions in a Curved Microchannel. *Chemical Engineering Research and Design*, 92(3), 423-434.

Ambatipudi, K. K., & Rahman, M. M. (2000). Analysis of Conjugate Heat Transfer in Microchannel Heat Sinks. *Numerical Heat Transfer, Part A: Applications, 37*(7), 711-731.

Aminossadati, S. M., Raisi, A., & Ghasemi, B. (2011). Effects of magnetic field on nanofluid forced convection in a partially heated microchannel. *International Journal of Non-Linear Mechanics, 46*(10), 1373-1382.

Arie, M. A., Shooshtari, A. H., Dessiatoun, S. V., Al-Hajri, E., & Ohadi, M. M. (2015). Numerical modelling and thermal optimization of a single-phase flow manifold-microchannel plate heat exchanger, *International Journal of Heat and Mass Transfer*, 81, 478-489.

Azizi, Z., Alamdari, A., & Malayeri M. R. (2015). Convective heat transfer of CU-water nanofluid in a cylindrical microchannel heat sink. *Energy Conversion and Management*, 101, 515-524.

Back, L. H. (1968). Laminar heat transfer in electrically conducting fluids flowing in parallel plate channels. *International Journal of Heat and Mass Transfer*, 11 (11), 1621-1636.

Biswal, L., Chakraborty, S., & Som, S. K. (2009). Design and Optimization of Single-Phase Liquid Cooled Microchannel Heat Sink. *Components and Packaging Technologies, IEEE Transactions on, 32*(4), 876-886.

Berger, M. (2007, April 12). Nanotechnology to the rescue of overheating computer chips. Retrieved from http://www.nanowerk.com/spotlight/spotid=1762.php

Chen, C. H., & Ding, C. Y. (2011). Study on the thermal behavior and cooling performance of a nanofluid-cooled microchannel heat sink, *International Journal of Thermal Sciences*, 50, 378-384.

Chen, C. S., Lee, S. M., & Sheu, J. D. (1998). NUMERICAL ANALYSIS OF GAS FLOW IN MICROCHANNELS. *Numerical Heat Transfer, Part A: Applications, 33*(7), 749-762.

Cho, E. S., Choi, J. W., Yoon, J. S., & Kim, M. S. (2010). Experimental study on microchannel heat sinks considering mass flow distribution with non-uniform heat flux conditions. *International Journal of Heat and Mass Transfer, 53*, 2159-2168.

Cito, S., Pallares, J., Fabregat, A., & Katakis, I. (2012). Numerical simulation of wall mass transfer rates in capillary-driven flow in microchannels. *International Communications in Heat and Mass Transfer, 39*(8), 1066-1072.

Corcione, M., (2010). Heat transfer features of buoyancy-driven nanofluids inside rectangular enclosures differentially heated at the sidewalls, *International Journal of Thermal Sciences*, 49, 1536–1546.

Chu, J. C., Teng, J. T., & Greif R. (2010). Experimental and Numerical Study on the Flow Characteristics in Curved Rectangular Microchannels. *Applied Thermal Engineering*, 30(13), 1558-1556.

Chu, J. C., Teng, J. T., Xu, T. T., Huang, S., Jin, S., Yu, X. F., Dang, T., Zhang, C. P., & Greif, R. (2012). Characterization of Frictional Pressure Drop of Liquid Flow thorugh Curved Rectangular Microchannels. *Experimental Thermal and Fluid Science*, 38, 171-183.

Chu, J. C., Jyh T. T., Ting T. X., Suyi H., Shiping J., Xiang F. Y., Thanhtrung D., Chun P. Z., & Ralph G. (2012). Characterization of frictional pressure drop of liquid flow through curved rectangular microchannels., *Experimental Thermal and Fluid Science*, 38, 171-183.

Chuan, L., Wang, X. D., Wang, T. H., & Yan, W. M. (2015). Fluid flow and heat transfer in microchannel heat sink based on porous fin design concept. *International Communications in Heat and Mass Transfer, 65*, 52-57.

Cuming, H. G., The Secondary Flow in Curved Pipes, *Volume 2880 of Reports and memoranda, Great Britain Aeronautical Research Council*, H. M. Stationery Office 1995.

Emran, M., & Islam, M. A. (2014). Numerical investigation of flow dynamcis and heat transfer characteristics in a microchannel heat sink, *Procedia Engineering*, 90, 563-568.

Dalponte, D., Silin, N., & Clausse, A. (2012). Gas flow in a channel semiobstructed by a porous medium. *Journal of Porous Media*, 15 (10), 927-936.

Dang, T., Teng, J., & Chu, J. (2011). *Influence of Gravity on the Performance Index of Microchannel Heat Exchangers-Experimental Investigations*. In Proceedings of the World Congress on Engineering, 3. London, UK, 1, 1230.

Dunn, P. D., Reay D. A., Heat pipes, *Pergamon Press*, Great Britain, 1994.

Fani, B., Abbassi, A., & Kalteh, M. (2013). Effect of nanoparticles size on thermal performance of nanofluid in a trapezoidal microchannel-heat-sink. *International Communications in Heat and Mass Transfer, 45*(0), 155-161.

Guan X., & Martonen, T. B. (1997). Simulations of Flow in Curved Tubes. *Aerosol Science and Technology, 26*(6), 485-504.

Dehghan, M., Valipour, M. S., & Saedodin, S. (2016). Microchannels enhanced by porous material: Heat transfer enhanceent or pressure drop increment. *Energy Conversion and Manage,emt, 110*, 22-32.

Fedorov, A. G., & Viskanta, R. (2000). Three-dimensional conjugate heat transfer in the microchannel heat sink for electronic packaging. *International Journal of Heat and Mass Transfer, 43*(3), 399-415.

Gamrat, G., Favre-Marinet, M., & Asendrych, D. (2005). Conduction and entrance effects on laminar liquid flow and heat transfer in rectangular microchannels. *International Journal of Heat and Mass Transfer, 48*(14), 2943-2954.

Ganji, D. D., & Malvandi, A. (2014). Natural convection of nanofluids inside a vertical enclosure in the presence of a uniform magnetic field. *Powder Technology*, 263, 50-57.

Garoosi, F., Behzad, R., & Rashidi, M. M. (2015). Two-phase mixture modellig of mixed convection of nanofluids in a square cavity with internal and external heating. *Poweder Technology, 275*, 304-321.

Ghasemi, B., & Aminossadati, A. M. (2010). Brownian motion of nanoparticles in a triangular enclosure with natural convection. *International Journal of Thermal Sciences, 49*, 931-940.

Gui, F., & Scaringe, R. P. (1995). *Enhanced heat transfer in the entrance region of microchannels.* Paper presented at the Proceedings of the 30th Intersociety Energy Conversion Engineering Conference, Orlando, FL, USA, 2, 289-294.

Harms, T. M., Kazmierczak, M. J., & Gerner, F. M. (1999). Developing convective heat transfer in deep rectangular microchannels. *International Journal of Heat and Fluid Flow, 20*(2), 149-157.

Ho, C. J., & Chen, W. C. (2013). An experimental study in thermal performance of Al_2O_3/water nanofluid in a minichannel heat sink. *Applied Thermal Engineering*, 50, 516-522.

Ho, C. J., Chen, Y. Z., Tu F. J., & Lai C. M. (2014a). Thermal performance of water-based suspensions of phase change nanocapsule in a natural circulation loop with a mini-channel heat sink and heat source. *Applied Thermal Engineering*, 64, 376-384.

Ho, C. J., Chen, W. C., & Yan W. M. (2014b). Experiment on thermal performance of water-based suspensions of Al_2O_3 nanoparticles and MEPCM particles in a minichannel heat sink. *International Journal of Heat and Mass Transfer*, 69, 276-284.

Ho, C. J., Chen, W. C., & Yan W. M. (2014c). Correlations of heat transfer effectiveness in a micichannel heat sink with water-based suspensions of Al_2O_3 nanoparticles and/or MEPCM particles. *International Journal of Heat and Mass Transfer*, 69, 293-299.

Ho, C. J., Liu, W. K., Chang. Y. S., & Lin, C. C. (2010). Natural convection heat transfer of alumina-water nanofluid in vertical square enclosure: An experimental study. *International Journal of Thermal Sciences,* 49(8), 1345-1353.

Hong, Z.-C., Zhen, C.-E., & Yang, C.-Y. (2008). Fluid Dynamics and Heat Transfer Analysis of Three Dimensional Microchannel Flows with Microstructures. *Numerical Heat Transfer, Part A: Applications, 54*(3), 293-314.

Hooman, K. (2008). Heat and fluid flow in a rectangular microchannel filled with porous medium, *International Journal of Heat and Mass Transfe*, 51, 5804-5810.

Hung, T. C., & Yan, W.-M. (2012). Effects of tapered-channel design on thermal performance of microchannel heat sink. *International Communications in Heat and Mass Transfer, 39*(9), 1342-1347.

Hung, T. C., Huang, Y. X., & Yan, W. M. (2013). Thermal performance analysis of porous-microchannel heat sinks with different configuration design, *International Journal of Heat and Mass Transfer,* 66, 235-243.

Ingham, D. B., and Pop, I., Transport phenomena in porous medium, *Pergamon*, Oxford, 1998.

Jeseela, S., & Sobhan, C. C. (2015). Numerical modelling of annular flow with phase change in a microchannel, *International Journal of Thermal Sciences*, 89, 87-99.

Jiang, P. X., Li, M., Ma Y. C., and Ze, P. R. (2004). Boundary conditions and wall effect for forced convection heat transfer in sintered porous plate channels, *International Journal of Heat and Mass Transfer*, 47, 2073-2083.

Kalteh, M., Abbassi, A., Saffar-Avval, M., Frijns, A., Darhuber, A., & Harting, J. (2012). Experimental and numerical investigation of nanofluid forced convection inside a wide microchannel heat sink. *Applied Thermal Engineering*, 36 (0), 260-268.

Kays, W. M., & Crawford, M. E., *Convective Heat and Mass Transfer*, 3rd ed., pp. 125, 1993.

Kandlikar, S. G. (2012). History, advances, and challenges in liquid flow boiling heat transfer in microchannels: A crtitical review. *Journal of Heat Transfer,* 134(3), 034001-1-034001-15

Keshavarz Moraveji, M., Mohammadi Ardehali, R., & Ijam, A. (2013). CFD investigation of nanofluid effects (cooling performance and pressure drop) in mini-channel heat sink. *International Communications in Heat and Mass Transfer,* 40(0), 58-66.

Kim, S.-M., & Mudawar, I. (2010). Analytical heat diffusion models for different micro-channel heat sink cross-sectional geometries. *International Journal of Heat and Mass Transfer, 53*(19–20), 4002-4016.

Knight, R. W., Goodling, J. S., & Hall, D. J. (1991). Optimal Thermal Design of Forced Convection Heat Sinks-Analytical. *Journal of Electronic Packaging, 113*(3), 313-321.

Konh, B., & Shams, M. (2014). Numerical simulation of roughness in microchannels by using the second-order slip boundary condition, *Nanoscale and Microscale Thermophysical Engineering*, 18, 97-112.

Kuipers, J. A. M., Prins, W., & Van Swaaij, W. P. M. (1992). Numerical calculation of wall-tobed heat-transfer coefficients in gas-fluidized beds, *AIChE Journal*, 38, 1079-1091.

Lee, P.-S., Garimella, S. V., & Liu, D. (2005). Investigation of heat transfer in rectangular microchannels. *International Journal of Heat and Mass Transfer, 48*(9), 1688-1704.

Liu, K., Qing Y., Shengguan H., Feng C., Yulong Z., Xiaole F., Lei L., Chao S. & Hao B. (2013). A High-Efficiency Three-Dimensional Helical Micromixer in Fused Silica. *Microsystem Technologies*, 19(7), 1033-1040.

Liu, Y., Chen, H. F., Zhang, H. W., & Li, Y. X. (2015). Heat transfer performance of lotus-type porous copper heat sink with liquid GaInSn coolant. *International Journal of Heat and Mass Transfer, 80*, 605-613.

Luciu, R. S, Mateescu, T., Cotorobai, V., & Mare, T. (2009). Nusselt Number and Convection Heat Transfer Coefficient for a Coaxial Heat Exchamger Using Al_2O_3-Water pH=5 Nanofluid. *Buletinul Instititilui Politehnis Din IASI.*

Lotfi, R., Saboohi, Y., & Rashidi, A. M. (2010). Numerical study of forced convective heat transfer of Nanofluids: Comparison of different approaches. *International Communications in Heat and Mass Transfer*, 37, 74-78.

McQuillen, J. B., Chato, D. J., Motil, B. J., Doherty M. P., Chao D. F., & Zhang N. (2012). Porous screen applied in liquid acquisition device channel and CFD simulation of flow in the channel. *Journal of Porous Media*, 15 (5), 429-437.

Malvandi, A., & Ganji, D. D. (2014a). Brownian motion and thermophoresis effects on slip flow of alumina/water nanofluid inside a circular microchannel in the presence of magnetic field. *International Journal of Thermal Sciences*, 84, 196-206.

Malvandi, A., & Ganji, D. D. (2014b). Magnetohydrodynamic mixed convective flow of Al2O3-water nanofluid inside a vertical microtube. *Journal of Magnetism and Magnetic Materials*, 369, 132-141.

Mathew, B. & Hegab, H. (2010).Application of effectiveness-NTU relationship to parallel flow microchannel heat exchangers subjected to external heat transfer. *International Journal of Thermal Sciences*, 31, 76-85.

Mathew, B. & Hegab, H. (2012). Experimental investigation of thermal model of parallel flow microchannel heat exhangers subjected to external heat flux. *International Journal of Heat and Mass Transfer*, 55, 2193-2199.

Mohammed, H. A. & Narrein, K. (2012). Thermal and Hydraulic Characteristics of Nanofluid Flow in a Helically Coiled Tube Heat Exchanger. *International Communications in Heat and Mass Transfer*, 39 (9), 1375-1383.

Nandi, T. K., & Chattopadhyay, H. (2014). Numerical investigations of developing flow and heat transfer in raccoon type microchannels under inlet pulsation, *International Communications in Heat and Mass Transfer*, 56, 37-41, 2014

Narrein, K. & Mohammed, H. A. (2013). Influence of Nanofluids and Rotation on Helically Coiled Tube Heat Exchanger Performance. *Thermochimica Acta.* 564, 13-23.

Nadeem, S., Rehman, A., Lee, C., & Lee, J. (2012). Boundary Layer Flow of Second Grade Fluid in a Cylinder with HEat Transfer. *Mathematical Problems in Engineering*, 13 pages.

Nield, D. A., and Bejan, A., Convection in porous media, 2nd ed., *Springer-Verlag*, New York, 1999.

Niazmand, H., Renksizbulut, M., & Saeedi, E. (2008). Developing slip-flow and heat transfer in trapezoidal microchannels. *International Journal of Heat and Mass Transfer, 51*(25–26), 6126-6135.

Ochende, T. B., Meyer, J. P., & Ighalo, F. U. (2010).Combined Numerical Optimization and Constructral Theory for the Design of Microchannel Heat Sinks , *Numerical Heat Transfer Part A*, 58, 882-899.

Patankar, S. V., & Spalding, D. B. A. (1972). Calculation Procedure for Heat, Mass and Momentum Transfer in Three-dimensional Parabolic Flows, *International Journal of Heat and Mass Transfer,* 15, 1787

Peng, X. F., & Peterson, G. P. (1996). Convective heat transfer and flow friction for water flow in microchannel structures. *International Journal of Heat and Mass Transfer, 39*(12), 2599-2608.

Pfahler, J., Harley, J., Bau, H., & Zemel, J. (1989). Liquid transport in micron and submicron channels. *Sensors and Actuators A: Physical, 22*(1–3), 431-434.

Pfahler, J., Harley, J., Bau, H., & Zemel, J. (1990). *Liquid and gas transport in small channels*. Paper presented at the ASME DSC.

Philips, R. J. Microchannel Heat Sinks, Advances in Thermal Modeling of Electronic Components and Systems, *Hemicphere Publishing Corporation*, New York 1990. (Chapter 3)

Poh, S. T., & Ng, E. Y. K. (1998). *Heat Transfer and Flow Issues in Manifold Microchannel Heat Sinks: A CFD Approach*. Proceedings of the Electronic Packaging Technology Conference, EPTC, Singapore, 246–250.

Pourmehran, O., Gorji, M. R., Hatami, M., Sahebi, S. A. R., & Domairry, G. (2015). Numerical optimization of microchannel heat sink (MCHS) performance cooled by KKL based nanofluids in saturated porous medium. *Journal of the Taiwan Institute of Chemical Engineers, 55*, 49-68.

Qu, W., & Mudawar, I. (2002a). Analysis of three-dimensional heat transfer in micro-channel heat sinks. *International Journal of Heat and Mass Transfer, 45*(19), 3973-3985.

Qu, W., & Mudawar, I. (2002b). Experimental and numerical study of pressure drop and heat transfer in a single-phase micro-channel heat sink. *International Journal of Heat and Mass Transfer, 45*(12), 2549-2565.

Rahman, M. M., & Gui, F. (1993a). Experimental measurements of fluid flow and heat transfer in microchannel cooling passages in a chip substrate *ASME EEP*, *2*(4), 685-692.

Rahman, M. M., & Gui, F. (1993b). *Design, fabrication, and testing of microchannel heat sinks for aircraft avionics cooling.* Paper presented at the Proceedings of the 28th Intersociety Energy Conversion Engineering Conference 1, Atlanta, GA, 1.1-1.6.

Raisi, A., Ghasemi, B., & Aminossadati, S. M. (2011). A numerical study on the forced convection of laminar nanofluid in a microchannel with both slip and no-slip condition, *Numerical Heat Transfer Part A*, 59, 114-129.

Saghit, M. Z., Ahadi, A., Yousefi, T., & Farahbakhsh, B. (2016). Two-phase and single phase models of flow of nanofluid in a square cavity: Comparison witg experimental results. *International Journal of Thermal Sciences,* 100, 372-380.

Shah, R. K. (1975). *Thermal entry length solutions for the circular tube and parallel plates.* Paper presented at the Proceedings of Third National Heat and Mass Transfer Conference, Indian Institute of Tenchnology, Bombay, HMT-11-75.

Sheu, T. S., Chen, S. J., & Chen, J. J. (2012). Mixing Performance of a Planar Micromixer with Circular Obstructions in a Curved Microchannel. *Chemical Engineering Science,* 71, 321-332.

Singh, R., Akbarzadeh, A., & Mochizuki, M. (2009). Sintered porous heat sink for cooling of high-powered microprocessors for server applications, *International Journal of Heat and Mass Transfer.* 52, 2289-2299.

Sivasankaran, S., Bhuvaneswari, M., Kim, Y. J., Ho, C. J., & Pan, K. L. (2011). Numerical study on magneto-convection of cold water in an open cavity with variable fluid properties, *International Journal of Heat and Fluid Flow.* 32, 932-942.

Sivasankaran, S., Malleswaran, A., & Lee, J. (2011). Hydromagnetic combined convection in a lid-driven cavity with sinusoidal boundary conditions in both sidewalls, *International Journal of Heat and Mass Trasnfer.* 54(1), 512-525.

Sun, L., Oosthuizen, P. H., & McAuley, K. B. (2006). A numerical study of channel-to-channel flow cross-over through the gas diffusion layer in a PEM-fuel-cell flow system using a serpentine channel with a trapezoidal cross-sectional shape. *International Journal of Thermal Sciences, 45*(10), 1021-1026.

Svino, J. M., & Siegel, R. (1946). Laminar forced convection in rectangular channels with unequal heat addition on adjacent sides. *International Journal of Heat and Mass Transfer*, 16, 733–741.

Targui, N., & Kahalerras, H. (2013). Analysis of a double pipe heat exchanger performance by use of porous baffles and pulsating flow. *International Communications in Heat and Mass Transfer, 76,* 43-54.

Tsai, T.-H., & Chein, R. (2007). Performance analysis of nanofluid-cooled microchannel heat sinks. *International Journal of Heat and Fluid Flow, 28*(5), 1013-1026.

Tuckerman, D. B., & Pease, R. F. W. (1981). High-performance heat sinking for VLSI. *Electron Device Letters, IEEE, 2*(5), 126-129.

Tuckerman, D. B., & Pease, R. F. W. (1982). *Ultrahigh Thermal Conductance Microstructures for Cooling Integrated Circuits.* Paper presented at the 32nd Electronic Components Conference.

Vafai, K., Handbook of Porous Media, 2nd ed., *Taylor & Francis*, New York, 2005.

Vajjha, R. S. V., Das, D. K., & Kulkarni D. P. (2010). Decelopment of new correlations for convective heat trasnfer and frcition factor in trubulent regime for nanofluids. *International Journal of Heat and Mass Transfer*, 53, 4607-4618.

Versteeg, H. K., & Malalasekara, W. An Introduction to Computational Fluid Dynamics, The Finite Volume Method, *Prentice Hall*, London 1995.

Wang, C. Y. (2013). Unsteady Poiseuille flow in a porous rotation channel *Journal of Porous Media*, 16 (3), 267-275.

Wang, L., & Fang L. (2007). Forced Convection in Slightly Curved Microchannels. *International Journal of Heat and Mass Transfer*, 50 (5-6), 881-896.

Wang, G., Niu, D., Xie, F., Wang, Y., Zhao, X., & Ding, G. (2015). Experimental and numerical investigations of a microchannel heat sink (MCHS) with micro-scale ribs and grooves for chip cooling. *Applied Thermal Engineering*, 85, 61-74.

Wang, Z. H., Wang, X.-D., Yan, W.-M., Duan, Y.-Y., Lee, D.-J., & Xu, J.-L. (2011). Multi-parameters optimization for microchannel heat sink using inverse problem method. *International Journal of Heat and Mass Transfer, 54*(13–14), 2811-2819.

Weng, H. C., & Chen, D. C. (2013). Magnetogasdynamic flow and heat transfer in microchannel with isothermally heated walls. *International Journal of Heat and Mass Transfer*, 57, 16-21.

Wen, D., & Ding, Y. (2004). Experimental investigation into convective heat transfer of nanofluids at the entrance region under laminar flow conditions. *International Journal of Heat and Mass Transfer*, 47, 5181-5188.

Weilin, Q., Mohiuddin Mala, G., & Dongqing, L. (2000). Pressure-driven water flows in trapezoidal silicon microchannels. *International Journal of Heat and Mass Transfer, 43*(3), 353-364.

Wu, P., & Little, W. A. (1983). Measurement of friction factors for the flow of gases in very fine channels used for microminiature Joule-Thomson refrigerators. *Cryogenics, 23*(5), 273-277.

Wu, P., & Little, W. A. (1984). Measurement of the heat transfer characteristics of gas flow in fine channel heat exchangers used for microminiature refrigerators. *Cryogenics, 24*(8), 415-420.

Xi, Y., Yu. J., Xie, Y., & Gao. J., (2010). Single-Phase Flow and Heat Transfer in Swirl Microchannels. Experimental Thermal and Fluid Science, 34(8), 1309-1315.

Xie, G., Li, G., Sunden, B., Zhang W., & Li, H. (2013). A numerical Study of the Thermal Performance of Microchannel Heat Sinks with Multiple Length Bifucation in Laminar Liquid Flow, *Numerical Heat Transfer Part A*, 65, 107-126.

Yang, G. & Ebadian M. A. (1996). Turbulent Forced Convection in a Helicoidal Pipe with Substantial Pitch. *International Journal of Heat and Mass Transfer.* 39 (10), 2015-2022.

Yang, W. H., Zhang, J. Z., & Cheng, H. (2005). The study of flow characteristics of curved Microchannel, *Applied Thermal Engineering*, 25(13), 1894-1907.

Yang, Y. Z., Wang, Y. B., & Huang, B. Y. (2014). Numerical Optimization for Nanofluid Flow in Microcnahnnels Using Entropy Generation Minimization, *Numerical Heat Transfer Part A*, 67, 571-588.

Yu, W., France, D. M., Routbort, J. L., & Choi, S. U. S. (2008). Review and Comparison of Nanofluid Thermal Conductivity and Heat Transfer Enhancements. *Heat transfer Engineering,* 29(5), 432-460.

Zhao, C. Y., & Lu, T. J. (2002). Analysis of microchannel heat sinks for electronics cooling. *International Journal of Heat and Mass Transfer, 45*(24), 4857-4869.

Zhang, C. P., Lian, Y. F., Yu, X. F., Liu, W., Teng, J. T., Xu, T. T., Hsu, C. H., Chang, Y. J., & Greif, R. (2013). Numerical and experimental studies on laminar hydrodynamics and thermal characteristics in fractal-like microchannel networks. Part B: Investigations in the performances of pressure drop and heat transfer. *International Journal of Heat and Mass Transfer.* 66, 939-947.

Zhang, T. T., Jia, L., Zhang, J., & Jaluria, Y. (2014). Numerical simulation of fluid flow and heat transfer in U-shaped microchannes, *Numerical Heat Transfer Part A*, 66, 217-228.

PUBLICATIONS

Narrein, K., Sivasankaran, S., & Ganesan, P. (2015). Two-Phase Analysis of Helical Microchannel Heat Sink using Nanofluids, *Numerical Heat Transfer, Part A: Applications,* 68, 1-14, (ISI, Q1)

Narrein, K., Sivasankaran, S., & Ganesan, P. (2015) Convective Heat Transfer and Fluid Flow Analysis in a Helical Microchannel Filled with Porous Medium, *Journal of Porous Media,* 18(8), 1-10, (ISI, Q3)

Narrein, K., Sivasankaran, S., & Ganesan, P. Numerical Investigation of Two-Phase Laminar Pulsating Nanofluid Flow in Helical Microchannel, *Numerical Heat Transfer, Part A: Applications,* (ISI, Q1) - In Press

Narrein, K., Sivasankaran, S., & Ganesan, P. Influence of Transverse Magnetic Field on Microchannel Heat Sink Performance, *Journal of Applied Fluid Mechanics,* (Accepted)

Narrein, K., Sivasankaran, S., & Ganesan, P. Influence of Transverse Magnetic Field on Trapezoidal Microchannel Heat Sink, *Journal of Magnetism and Magnetic Materials,* (Submitted)

Narrein, K., Sivasankaran, S., & Ganesan, P. Numerical Analysis of Convective Heat Transfer and Fluid Flow in a Helical Microchannel Heat Sink, *Numerical Heat Transfer, Part A: Applications,* (Submitted)